

# Abstract

Advancements in robot-assisted surgery invigorate the application of robotic technologies in dentistry. This thesis aims to develop a robotic system in assisting endodontic treatment procedures. Considering the workspace and the extreme precision in endodontic treatment, a six degrees of freedom robotic manipulator – DentiBot – forms the basis of the developed system. Due to the lack of visual feedback in endodontic treatment, the DentiBot is integrated with a force and torque sensor, whose measurements guide the robot's motion during surgical procedures. Two main iatrogenic errors causing the failures of root canal treatment, namely incomplete root preparation and instrument fracture, are addressed. First, force-guided robot alignment based on admittance control techniques is proposed to adjust the surgical path and compensate for the patient's movement in real-time. Second, file federate control is proposed to protect endodontic files from fracturing, particularly when the file gets stuck in the root canal. These two functions are combined to automate the root preparation procedure. Experimental results have demonstrated the performance of force-guided alignment and file feedrate control. The feasibility of robot-assisted endodontic treatment is verified by the pre-clinical evaluation performed on acrylic root phantoms.

*Keywords:* *Endodontic treatment, Robot-assisted system, Admittance control, Force-guided alignment, File feedrate control, Instrument fracture*

# Contents

<b>Abstract</b>	<b>i</b>
<b>List of Figures</b>	<b>iv</b>
<b>List of Tables</b>	<b>ix</b>
<b>1 Introduction</b>	<b>1</b>
1.1 Motivation . . . . .	1
1.2 Problem Definition and Previous Work . . . . .	2
1.3 Proposed Method . . . . .	6
1.4 Main Contributions . . . . .	8
<b>2 State-of-the-Art</b>	<b>10</b>
2.1 Surgical Robots Applied in Dentistry . . . . .	10
2.2 Robot-Assisted Endodontic Treatment . . . . .	14
<b>3 Design and Analysis of the Dental Surgical Robot – DentiBot</b>	<b>19</b>
3.1 Requirement and Specification . . . . .	19
3.2 Design of DentiBot . . . . .	20
3.3 Kinematics Analysis . . . . .	23
3.4 Tool-tip Coordinate . . . . .	32
<b>4 Force-Guided Robot Alignment</b>	<b>40</b>
4.1 Problem Definition and Proposed Method . . . . .	40

<b>CONTENTS</b>	<b>iii</b>
4.2 Integration of F/T sensor . . . . .	42
4.3 Dragging Mode . . . . .	52
4.4 Self-Alignment Mode . . . . .	58
4.5 Parameter Selection . . . . .	63
<b>5 File Rotation and Feedrate Control</b>	<b>68</b>
5.1 Problem Definition and Proposed Method . . . . .	68
5.2 Inverse Rotation Control . . . . .	73
5.3 File Feedrate Control . . . . .	75
5.4 Automated Endodontic Treatment . . . . .	78
<b>6 Experimental Results</b>	<b>81</b>
6.1 Experimental Setup . . . . .	81
6.2 Force-Guided Alignment . . . . .	89
6.3 Pre-Clinical Evaluation . . . . .	107
<b>7 Conclusions and Future work</b>	<b>111</b>
7.1 Conclusions . . . . .	111
7.2 Discussion and Future Work . . . . .	112
<b>Appendices</b>	<b>114</b>
A Forward Kinematics . . . . .	115
B Jacobian Matrix . . . . .	116
<b>Reference</b>	<b>122</b>

# List of Figures

1.1	Endodontic treatment procedure . . . . .	3
2.1	Dental robot designed by the University of Hong Kong . . . . .	11
2.2	Implant robot designed by Yokohama National University, Japan .	11
2.3	Implant robot designed by Chosun university, Korea . . . . .	12
2.4	Implant robot - YOMI (Neosis, Miami, Florida, USA) . . . . .	13
2.5	Patient tracking system of YOMI . . . . .	14
2.6	Robot-assisted endodontic treatment . . . . .	15
2.7	Pre-clinical test of the endodontic micro robot . . . . .	16
2.8	Design of endodontic robot with mirco actuators . . . . .	17
2.9	Tool change mechanism of the endodontic micro robot . . . . .	17
3.1	DentiBot formed by a 6 DoF robotic manipulator . . . . .	20
3.2	Modified dental handpiece composed of a servo motor, a coupler, and the endodontic file. . . . .	21
3.3	Coordinate definition of DentiBot. {0} to {6} represent frames of robot arm axes. {S} represents the frame of F/T sensor. {H} represents the handpiece tool-tip frame. . . . .	23
3.4	Schematic diagram for tool center point (TCP). The translation vector ${}^6p_H$ denotes the origin position relative to the frame{6}. . .	34
3.5	Four points method. Align a fixed point with four different poses.	36
3.6	Schematic diagram for obtaining the tool vector. . . . .	37

3.7 Illustration of finding the rotation matrix with the tool vector . . . . .	38
4.1 Data analysis of F/T sensor. Initial Value is the initial value of F/T sensor without reset. Gravity Load is the gravity of end effector. External Force is the value of force or torque. . . . .	42
4.2 Control scheme. $f_d$ denotes the desired forces and torques vector. $f_s$ denotes the real value measured by F/T sensor. $\dot{x}, [\dot{x}, \dot{y}, \dot{z}, \dot{\theta}_x, \dot{\theta}_y, \dot{\theta}_z]$ , denotes the velocity of end effector. $J_g$ denotes the geometric Ja- cobian matrix. $\dot{\theta}, [\dot{\theta}_1, \dot{\theta}_2, \dot{\theta}_3, \dot{\theta}_4, \dot{\theta}_5, \dot{\theta}_6]$ , denotes the joints' angular velocities. $\theta, [\theta_1, \theta_2, \theta_3, \theta_4, \theta_5, \theta_6]$ , denotes the joints' angles. $M$ is an inertial diagonal matrix, $\text{diag}(m_1, m_2, \dots, m_6)$ , and $B$ is a damping diagonal matrix, $\text{diag}(b_1, b_2, \dots, b_6)$ . $K$ is a constant gain diagonal matrix, $\text{diag}(k, k, k, k, k, k)$ . . . . .	53
4.3 Illustration of changing reference frame from $\{S\}$ to $\{H\}$ . ${}^S f_p$ and ${}^S \tau_p$ respectively denote a force vector and a torque vector applied at point p and observed from $\{S\}$ . . . . .	59
4.4 Illustration of changing measurement point from point p to point q. $f$ denote a force vector applied at frame $\{H\}$ and observed from point p and q. $r_p, r_q$ are distances between point p, q and their projections on $f$ . . . . .	60
4.5 Implementation of Sensor compensation in the DentiBot. . . . .	62

4.6 Admittance Control. $f_d$ denotes the desired forces and torques vector. $f_s$ denotes the real value measured by F/T sensor. $\dot{x}$ , $[\dot{x}, \dot{y}, \dot{z}, \dot{\theta}_x, \dot{\theta}_y, \dot{\theta}_z]$ , denotes the velocity of end effector. $\mathbf{M}$ is an inertial diagonal matrix, $\text{diag}(m_1, m_2, \dots, m_6)$ , and $\mathbf{B}$ is a damping diagonal matrix, $\text{diag}(b_1, b_2, \dots, b_6)$ . $\mathbf{K}$ is a constant gain diagonal matrix, $\text{diag}(k, k, k, k, k, k)$ .	63
4.7 Reference point A in Dragging Mode. Reference point B and holding points $G_1, G_2$ in Self-Alignment Mode.	65
5.1 The illustration of an endodontic file	69
5.2 Endodontic files with different diameters	70
5.3 The prototype of DentiBot. A single z-axis manipulator with a modified handpiece to verify our proposed method – Inverse Rotation Control	73
5.4 Motion planning of Inverse Rotation Control with the prototype of DentiBot. $I_{\max}$ denotes the maximum bearing current	74
5.5 Control scheme of File Feedrate Control with DentiBot. $\tau_d$ represents the desired torque. $\tau_z$ represents the file torque. $f_z$ is the third element of the input of admittance control.	76
5.6 Flow chart of File Feedrate Control with DentiBot. $\{^H\}f, [f_x, f_y, f_z, \tau_x, \tau_y, \tau_z]$ , is measured by F/T sensor related to frame $\{H\}$ . $f_d$ denotes the desired force.	77
5.7 Methods of autonomous endodontic treatment	78

5.8 Flowchart of the algorithm for autonomous endodontic treatment	79
6.1 Communication protocol – EtherCAT. Master device is RT-target and slave devices are robot arm, F/T sensor and modified handpiece.	82
6.2 Graph user interface with LabVIEW 2018 . . . . .	83
6.3 Experimental setup with DentiBot, a motion-capture system cap- turing LEDs, and a Stewart platform simulating patient moving . .	84
6.4 Flow charts for force-guided alignment experiment. (a) shows Config.A – inserting without file rotation. (b) shows Config.B – inserting with file rotation. (c) shows Config.C – inserting with file rotation and file feedrate control. . . . .	90
6.5 Position command of Stewart platform for force-guided alignment experiment . . . . .	91
6.6 Patient trajectory simulated by Stewart platform . . . . .	94
6.7 Config. A: Handpiece position vs root position root and their relative distance . . . . .	96
6.8 Config. B: Handpiece position vs root position root and their relative distance . . . . .	97
6.9 Config. C: Handpiece position vs root position root and their relative distance . . . . .	98
6.10 Zoom-in plot of Force vs Velocity on Z-axis from 80th to 90th second	99
6.11 Config. A: Force vs Velocity and Velocity command . . . . .	100
6.12 Config. B: Force vs Velocity and Velocity command . . . . .	101

6.13 Config. C: Force vs Velocity and Velocity command . . . . .	102
6.14 Config. A: Force vs Handpiece position . . . . .	104
6.15 Config. B: Force vs Handpiece position . . . . .	105
6.16 Config. C: Force vs Handpiece position . . . . .	106
6.17 Flowchart of the algorithm for autonomous endodontic treatment	107
6.18 Acrylic root phantom used in operative technique practice . . . .	108
6.19 Experiment 2: A comparison of completeness before and after two times drilling. $\tau_d$ were set 40 in A,B,C and 50 in D,E,F . . . . .	109

# List of Tables

3.1	Denavit-Hartenberg parameters of Meca500 . . . . .	24
4.1	Comparison of arc-functions . . . . .	50
4.2	Moving commands of Meca500 . . . . .	56
4.3	Parameters setting of Admittance control. . . . .	66
6.1	Specifications of the hardware and software environments . . . . .	86
6.2	Technical specifications of the robot arm - meca500 . . . . .	87
6.3	Technical specifications of the F/T sensor - mini40 . . . . .	88
6.4	Parameters setting of admittance control in Experiment 1. . . . .	92
6.5	Results of pre-clinical evaluation . . . . .	110



# **Chapter 1**

## **Introduction**

A surgical robot in assisting endodontic treatment – DentiBot – is presented in this thesis. DentiBot is designed to help dentists perform the root preparation procedure autonomously. This chapter will give brief introductions of the endodontic treatment, previous work, problem definition, and proposed method.

### **1.1 Motivation**

Advancements in robot-assisted surgery invigorate the application of robotic technologies in dentistry. However, the majority of dental robot is applied in implantology. Research on robot-assisted Endodontic treatment is seldom explored. The performance of endodontic treatment depends on a dentist's long-term clinician experience and skill. A qualified dentist with a certification can operate an endodontic treatment. With enough clinical experience, the dentist can increase the success rate of surgery and acquire an endodontist license. According to statistics from the Ministry of Health and Welfare, R.O.C. (Taiwan) [1], the number of dentists in Taiwan is 15,178. However, according to The Academy of Endodontology, R.O.C. (Taiwan) [2], only 238 dentists own an endodontist license. It implies that performing an endodontic treatment requires the dentist's expertise of endodontics

and enough clinical experience.

Besides, endodontic treatment is a tedious and time-consuming surgery for dentists due to intricate situations of teeth. A patient who suffered from an infected tooth spends countless hours see a dentist. It might take two to three rounds of treatments, even more than two months in the worst case.

Therefore, our team looks forward to designing a robot-assisted system to accomplish endodontic treatment. The robot-assisted system should have the capability to reduce times for entire treatment, increase the success rate of endodontic treatment for dentists, and provide patients a safer surgery.

## 1.2 Problem Definition and Previous Work

In this section, endodontic treatment is introduced followed by a brief description of related work and problem definition.

### **Endodontic treatment**

Endodontic treatment, also known as root canal treatment and nerve extraction, is performed to cure an infected tooth. The main procedure of endodontic treatment is divided into three parts - Opening, Cleaning, and Filling shown in Figure 1.1.

An infected tooth arises from periodontal disease, attrition, trauma, or decay. Once the dental pulp is infected, it causes an irreversible inflammation and lets patients confront endodontic treatment. Figure 1.1 shows an infected tooth and its dental pulp, which consists of blood vessels, nerves, connective tissues, and

lymphatics. In the "Opening", a dentist drills the crown of the infected tooth to remove dentin and expose infected pulps inside canals to the air [3]. Next, "Cleaning" termed root preparation or debridement is the most essential step in entire endodontic treatment. Dentists uses an endodontic file, a superelastic root reamer, to remove the infected pulp thoroughly. It is necessary to ensure that there are no remained infected pulps [4] after this procedure. Then, in the "Filling", the dentist uses a dental plugger to fill the empty root canal with Gutta-percha, a plastic substance. "Filling" can prevent cross-infection between root canals because the cured tooth remains many invisible and inaccessible pulp tissue [5]. Finally, the dentist seals the root canal with a new crown to protect cured root canal and accomplishes endodontic treatment.

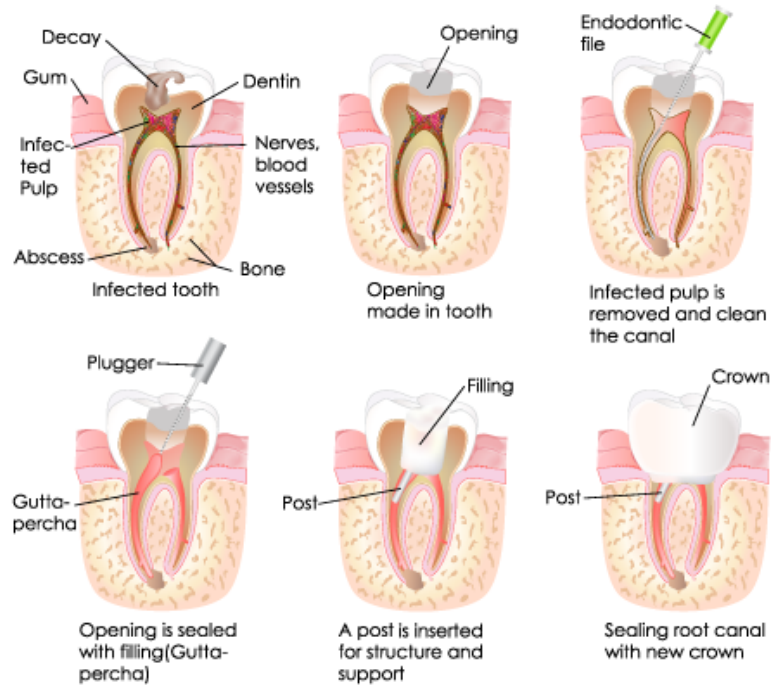


Figure 1.1: Endodontic treatment procedure [6]

As stated above, "Cleaning" is of paramount importance in whole treatment because cleaning improperly will result in pulp necrosis, apical abscess, periodontal ligament inflammation, or even cellulitis [7]. If there are too many untreated contaminated canals, the treatment should be operated on again. Success in endodontic treatment depends on how well the dentist cleans and shapes the root canal. Therefore, it is important to figure out how a robot assists dentists in performing root canal treatment.

## **Previous Work**

There are more and more robots which applied to specific surgery. In the dental field, the majority of robotic applications are in implant surgery. The researchers in Chosun University built a dental implant robot [8], a remote center of motion (RCM) mechanism. Li, J. et al. designed a robotic system using a soft bracing technique to drill teeth [9]. Also, there is a commercial implant robot, YOMI (Neocis ,Miami, FL). However, to the best of our knowledge there was one and only one robot for endodontic treatment. Janet Dong and his team proposed a microrobot performing endodontic treatment with a surgical path planned by 3-D root computer model [10]. However, the study using 3-D model belongs to pre-operation. Any patient moving or image error is a big challenge because it is not easy to reschedule the preoperative path because root canals in a tooth are unseen by a camera from any angle. Besides, once an endodontic file enters into a root canal, it is hard to obtain the tool-tip of file due to its flexibility. The endodontic file will

bend when it bears a force. Iatrogenic errors such as perforation, overpreparation, and underpreparation might happen. Therefore, a problem reveals – how to adjust a surgical path to drill root canals in real-time and without visual feedback?

On the other hand, instrument fracture is the other concern during endodontic treatment [11]. If an endodontic file suffers excessive usage, it would unpredictably break. The leading causes of fractured files are torsional fracture and flexural fatigue, which account for 55.7% and 44.3% separately [12]. Removal of a broken file in a small root is technically tricky, so it is essential to reduce the probability of the instrument fracture. Therefore, our robot should prevent the instrument fracture by some detection. In addition, endodontic treatment also requires repeatedly drilling to clean canals thoroughly. This repetitive action of root canal treatment is tedious and time-consuming. Therefore, It would be an efficient way to automate the root preparation procedure by an endodontic robot.

### **Problem Definition**

To sum up, there are three main problems.

1. How to build an endodontic robot to assist dentists in performing the root preparation?
2. How to adjust the surgical path in real-time and without visual feedback in any intricate root situations?
3. How to protect the endodontic file from fracturing during the surgery?

## 1.3 Proposed Method

In this section, the prospect of DentiBot is presented followed by the proposed methods.

### Prospect

To build a robot system for endodontic treatment, it is necessary to contemplate requirements and specifications comprehensively from technical and clinical perspectives. There are four subjects of the proposed robot-assisted project.

1. Dentist could move DentiBot to an infected tooth.
2. Searches all root canals of the infected tooth.
3. Cleans roots thoroughly in the root preparation.
4. Detects the apex of the root canal and accomplishes entire treatment.

### Design of DentiBot

By comprehensive consideration, a robot-assisted system – DentiBot – is developed to provide a precise and safe endodontic treatment. DentiBot consists of a 6-DoF robot arm, a 1-DoF end effector modified from a dental handpiece, and a 6-DoF force/torque sensor. This 7-DoF robotic manipulator can manifest various motions such as drilling and reciprocation endodontic treatment requires.

Therefor, DentiBot meets requirements of workspace and dimension in endodontic treatment.

### **Force-Guided Robot Alignment**

Due to the lack of visual feedback in endodontic treatment, force-guided robot alignment based on admittance control techniques is proposed to guide the robot's motion. Force-guided alignment enables our system to adjust the surgical path and compensate for the patient's movement in real-time. That means DentiBot could align the root canal path by force feedback without vision feedback. Hence, force-guided alignment could solve the first failure factor – incomplete root preparation.

### **File Rotation and Feedrate Control**

To protect endodontic files from fracturing particularly when the file gets stuck in the root canal, two approaches based on torque control are proposed. The first method, inverse rotation control, could remove debris and prevent files from getting stuck. The second method, file feedrate control, utilizes the measured file torque to regulate the file feedrate. These two proposed approaches are combined to protect endodontic files and achieve high performance in the root preparation procedure.

A new idea that combines all proposed functions – force guided alignment, inverse rotation control, and file feedrate control is presented.

## 1.4 Main Contributions

In this section, main contributions of the thesis are highlighted followed by a brief description of the organization of the thesis.

### Main Contributions of the thesis

The thesis is the beginning of the proposed project and focuses on the first and third subject of the project. In conclusion, there are three main contributions.

1. Integrate a 7-DoF robotic manipulator with 6-DoF F/T sensor for performing endodontic treatment.
2. Real-time Force-guided robot alignment for surgical path without visual feedback.
3. Inverse rotation control and File federate control for protecting the endodontic file from fracturing.

### Organization of the Thesis

In Chapter 2, The state-of-the-art of dental robots for implant placement and endodontic treatment are surveyed and summarized. Implant robots including a commercial robot are reviewed and an endodontic robot is dissected.

The proposed robot – DentiBot – is highlighted in chapter 3. Technical solutions to system integration with a robot arm are presented. The kinematics of the robot arm is derived. Moreover, how to find the tool-tip coordinate is explained.

Chapter 4 demonstrates how to solve the system integration problem when combining a robot arm and an F/T sensor. Gravity compensation and reference frame changing issues are clarified. Moreover, admittance control based on F/T sensor is presented. Subsequently, Force-guided robot alignment is described.

The proposed approach for protecting an endodontic file from fracturing is shown in Chapter 5. File property is discussed and the methods for estimating torque are interpreted. Inverse rotation control and file feedrate control which are used to prevent instrument fracture are defined. Ultimately, the most important thing is that an algorithm for robot-assisted endodontic treatment is proposed.

Experiment results are shown and analyzed in Chapter 6. Technical and pre-clinical experiments are conducted. Force-guided alignment is confirmed by the first experiment and the proposed algorithm including all functions is proven by the second experiment. In the end, Chapter 7 makes a summary and lists future work for this thesis.

# **Chapter 2**

## **State-of-the-Art**

To comprehensively contemplate requirements of an endodontic robot such as workspace, payload, clinical problems, works of literature in the dental field are involved. Recent literatures have revealed that researchers have seen the use of dental robot [13, 14, 15], Most largely, implant surgery is widely discussed [16, 17]. In this chapter, the pieces of literature about dental robots for implant placement and endodontic treatment will be reviewed.

### **2.1 Surgical Robots Applied in Dentistry**

Advancements in robot-assisted surgery invigorates researches on robotics in the dental field. However, the majority of robotic applications are in implant surgery.

The research team in Hong Kong designed a dental manipulator with tendon-sheath mechanism and bracing actuator [9]. The tendon-sheath mechanism drove the whole machine to move and provided flexible manipulations. The soft bracing actuator at the end effector held the handpiece stably due to its stiffness and satisfied the requirement of workspace in a patient mouth. The objective of this robotic system is to perform from operative caries removal, crown preparation, filling, to

Orthodontia. However, pre-clinical tasks had not been proven yet.

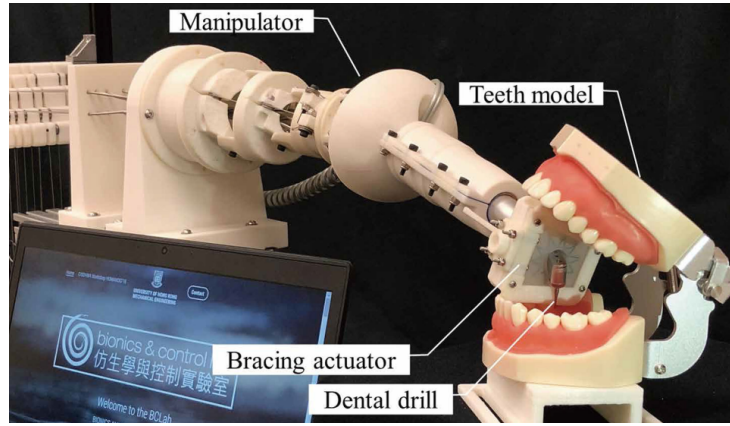


Figure 2.1: Dental robot designed by the University of Hong Kong [9].

T. Iijima *et al.* proposed a master-slave dental system [18]. The serial-parallel hybrid mechanism provided remote center of motion (RCM) as shown in Figure 2.2. A reaction force observer (RFOB) was integrated to obtain force information. Acceleration based bilateral control was implemented to communicate master with slave.

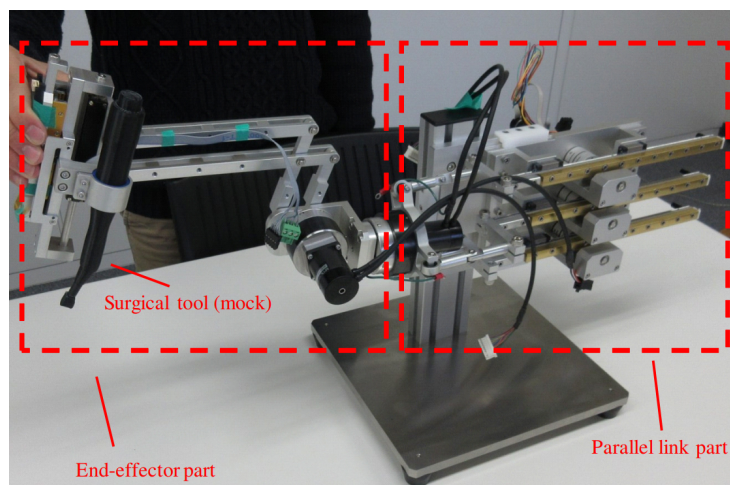


Figure 2.2: Implant robot designed by Yokohama National University, Japan [18].

G. Kim *et al.* proposed an implant robot based on a double parallelogram mechanism [8]. The manipulator is shown in Figure 2.3. With the double parallelogram mechanism, the entry point would be constrained at a fixed point and form a remote center of motion (RCM). Besides, a force and torque sensor was integrated to design an admittance type of cooperative manipulator. The manipulator used torque values in the x and y-axis to calibrate the bias caused by drilling. However, it seemed that the prototype of robot did not meet the requirement of dimension and workspace.

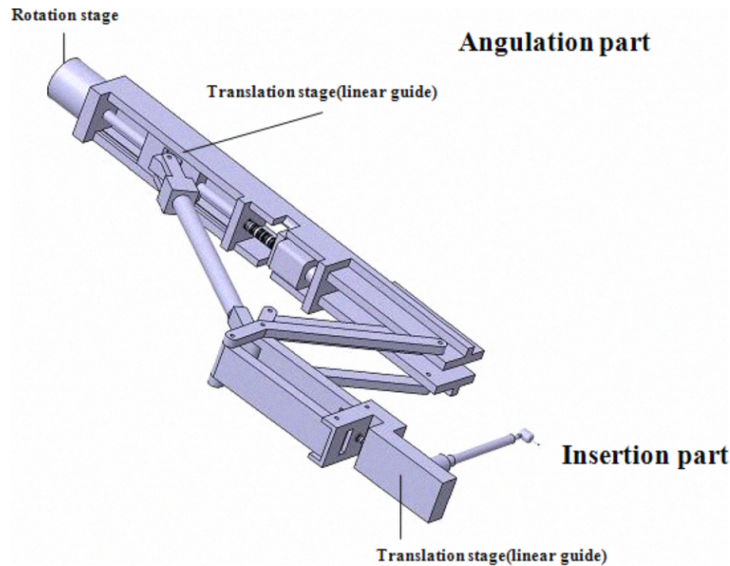


Figure 2.3: Implant robot designed by Chosun university, Korea [8].

There is a commercial robot, YOMI (Neosis, Miami, Florida, USA) [19, 20], which is a robot-assisted system for minimally invasive implant surgery shown in Figure 2.4. YOMI provides precise physical and haptic guidance to perform implant placement because it constrains the drilling position, direction, orientation, and depth. Dentists can design the surgical plan in advance with pre-planning

software and adjust it intraoperatively. Undoubtedly it could increase the accuracy of drilling and decrease the surgery time. Also, once the tool approaches the danger zones such as nerves and sinus cavities, it will alert the dentist to take appropriate measures.



Figure 2.4: Implant robot - YOMI (Neosis, Miami, Florida, USA)

An additional robot arm is connected to the intraoral splint which is mounted on patient mouth shown in Figure 2.5. It enables the robot to keep track of the position information [21] . If the patient moves, YOMI will detect it and alignment immediately to retain the accuracy of the drilling position. Furthermore, it visualizes a 3-D preoperative CT scan and real-time information on the screen to show the updated anatomical features such as drilling entry and bone quantity. YOMI has received the clearance from FDA and has performed more than 2,700 surgeries in the USA. In the pandemic of Covid-19 in 2020, YOMI provided

non-contact surgery between dentists and patients due to its automatic robotic system.

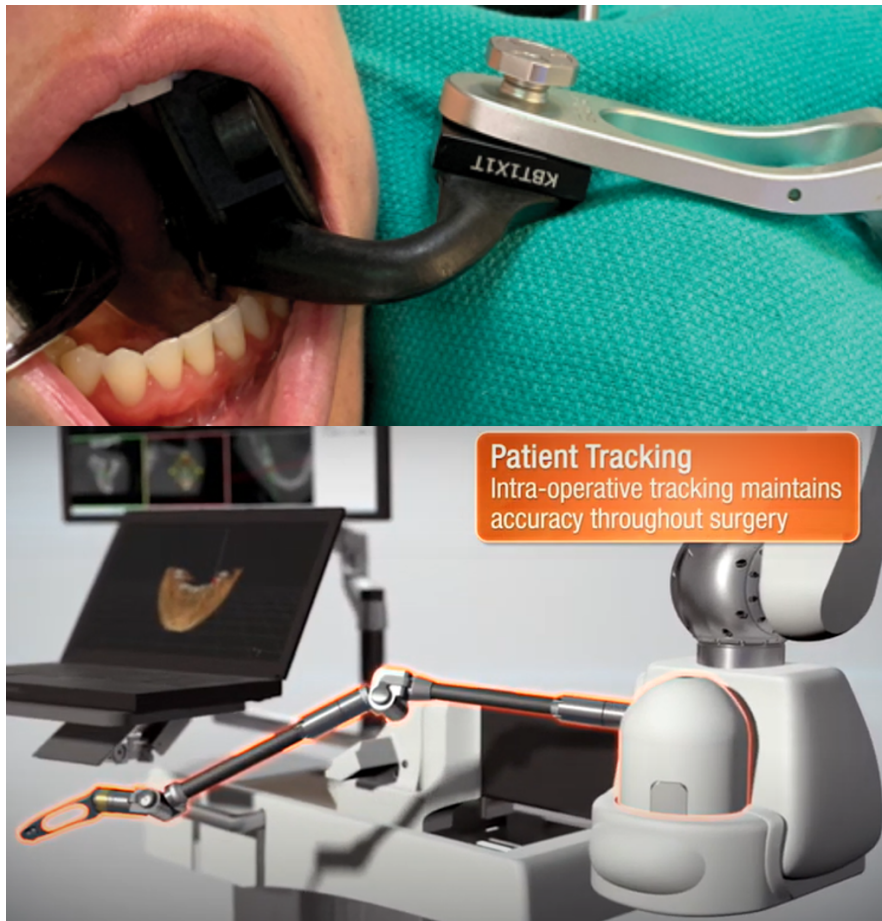


Figure 2.5: Patient tracking system of YOMI [21].

## 2.2 Robot-Assisted Endodontic Treatment

Endodontic treatment requires a higher precision and accuracy than implant placement. There was a domestic team dedicating to develop an endodontic robot. In Intelligent Micro Robot Development for Minimum Invasive Endodontic

Treatment [10, 22, 23, 24], their team proposed a complete project, which involves whole endodontic treatment including "Opening", "Cleaning", and "Filling".

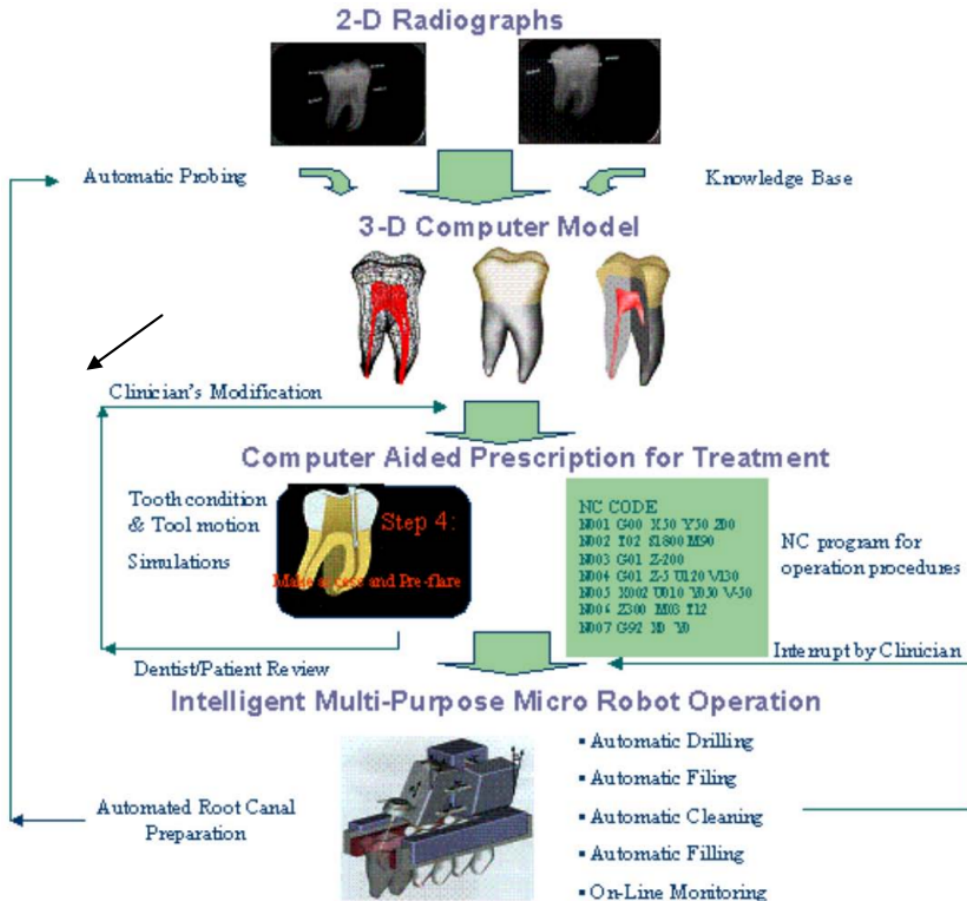


Figure 2.6: Robot-assisted endodontic treatment [22]

The aim of this project was taken apart of several parts as shown in Figure 2.6. Before starting surgery, it utilized a 2-D X-ray image to build a 3-D computational model and designed the corresponding surgical path by computer-aided treatment procedure planning which is widely used in industry. A micro-machine with a tool change mechanism was built to drill and fill. Then, an ultrasonic cleaning tool was interfaced to remove the cutting chips and pulps. However, the study using a 2-D

X-ray image to build a 3-D model belongs to pre-operation. Any accident during surgery would destroy the ideal pre-planned path.

Also, a micro robot was developed to perform root canal treatment. It was small enough to be mounted on several teeth within a mouth as shown in Figure 2.7. Therefore, it reduced the patient's inconvenience because it allowed the patient to close their mouth during the surgery.



Figure 2.7: Pre-clinical test of the endodontic micro robot [10]

A multi-purpose micro-machine was designed for automatic endodontic treatment as shown in Figure 2.8. A parallel bracket was installed on the teeth and the micro-machine was mounted on it. There were three radiopaque reference points inside the bracket. The patient with brackets was taken CT scan, and then three radiopaque points were obtained. With three points, a reference frame was built. Therefore, The machine mounted on bracket would recognize the infected tooth. The micro-machine had 6-DoF including five axes and a drilling tool, they were driven by micro actuators.

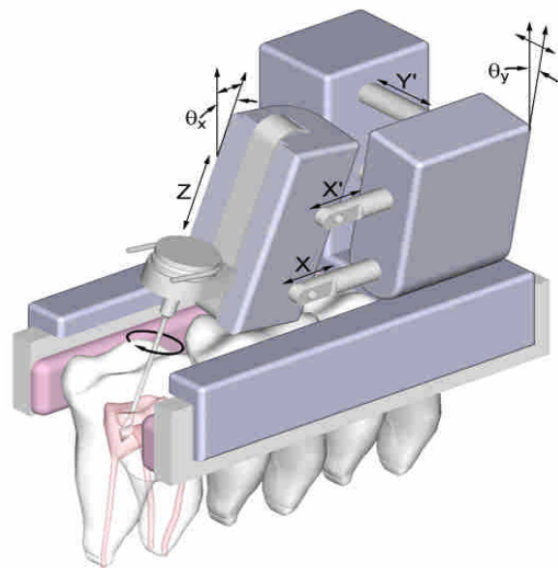


Figure 2.8: Design of endodontic robot with micro actuators [10]

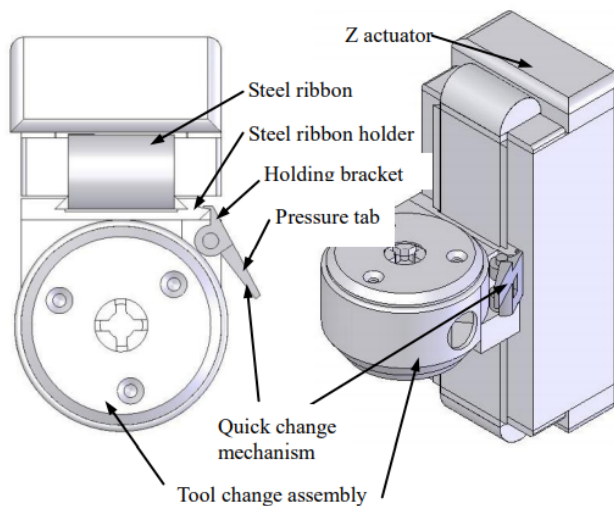


Figure 2.9: Tool change mechanism of the endodontic micro robot [23]

A tool change mechanism was illustrated in Figure 2.9. Because there were several procedures during surgery and different tools were used in different phrase. If the machine can hold all types of tools without calibration, the surgery time would decrease dramatically. Moreover, a hydraulic system was integrated to provide enough drilling force for "Opening" procedure.

However, despite that using 2-D or 3-D image is an appropriate approach to design a surgical path [25, 26], it belongs to pre-operation. There are many factors to disrupt the surgical path such as uncertain tooth condition and image error. It is not easy to reschedule the motion planning because the root canal in a tooth is unseen by a camera from any angle. Besides, once an endodontic file enters into a root canal, it is hard to obtain the tool tip position due to its flexibility.

# **Chapter 3**

## **Design and Analysis of the Dental Surgical Robot – DentiBot**

To design a autonomous endodontic robot, its workspace and dimension are discussed in Section 3.1 followed by detail description of hardware of DentiBot in Section 3.2. Technical solutions to system integration with a robot arm are clarified in this chapter. Section 3.3 and Section 3.4 serve as a robot arm tutorial and provide some imperative approaches when combining a robot arm and an end effector.

### **3.1 Requirement and Specification**

The dental surgical robot should perform delicate and complicated surgery operations because the average diameter of a root canal is 0.28 ( $\pm 0.08$ ) mm [27]. Therefore, our system should have a high resolution of movement. Next, an appropriate workspace is required. In dental anatomy, teeth are located on the maxillary (lower jaw) and the mandibular (upper jaw). To perform surgery with both sides, the end effector should rotate at least 180 degrees. Furthermore, a research indicated that the average range of maximum mouth opening is 50.3 ( $\pm 6.26$ ) mm [28]. Hence, the end effector should be less than this range.

## 3.2 Design of DentiBot

As discussed in the previous section, we decide to build a system composed of a robot arm, an F/T sensor, and a modified handpiece. Why choosing a robot arm and an F/T sensor is because we want to mimic the dentist's clinical behaviour. Due to the 6-DOF robot arm, DentiBot can achieve the action with less hardware restriction. DentiBot can easily move to almost desired positions and rotate more than 180 degrees to drill tooth in both sides of mouth. Also, with the 6-DoF F/T sensor, the real-time force and torque feedbacks are obtained and serve as a haptic feedback. DentiBot can take reaction with the F/T sensor such as a dentist touch and sense something in the surgery and do the corresponding reaction. Besides, by modifying the existing handpiece, which is a handheld dental electric device, there is no doubt that the workspace and dimension in the mouth are satisfied. Also, there are two adapters designed to assemble these devices.

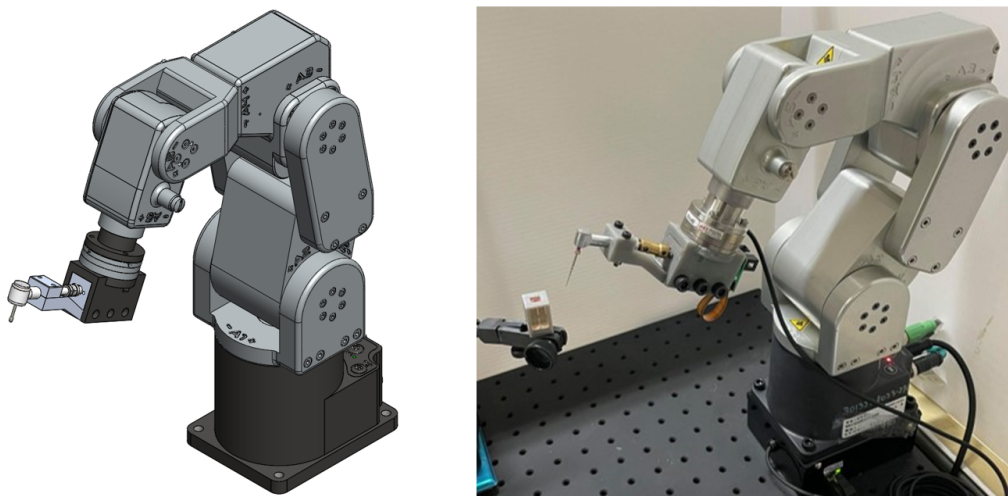


Figure 3.1: DentiBot formed by a 6 DoF robotic manipulator

To meet the requirement of workspace and dimension, we have to select appropriate devices according to those requirements. As shown in Figure 3.1, a 6 DoF robotic manipulator (Meca-500, Mecademic Inc., Montreal, Canada) is used in this work. Its feature is high repeatability (precision: 5  $\mu\text{m}$ ), and it is equipped with zero-backlash speed reducers. In addition, it is compact and portable for laboratory investigation. Second, the corresponding F/T sensor (ATI Industrial Automation, Apex, America) with three force and three torque detections is involved. As for the end effector, we modify an existing dental handpiece that equips a file exchange mechanism shown in Figure 3.2.

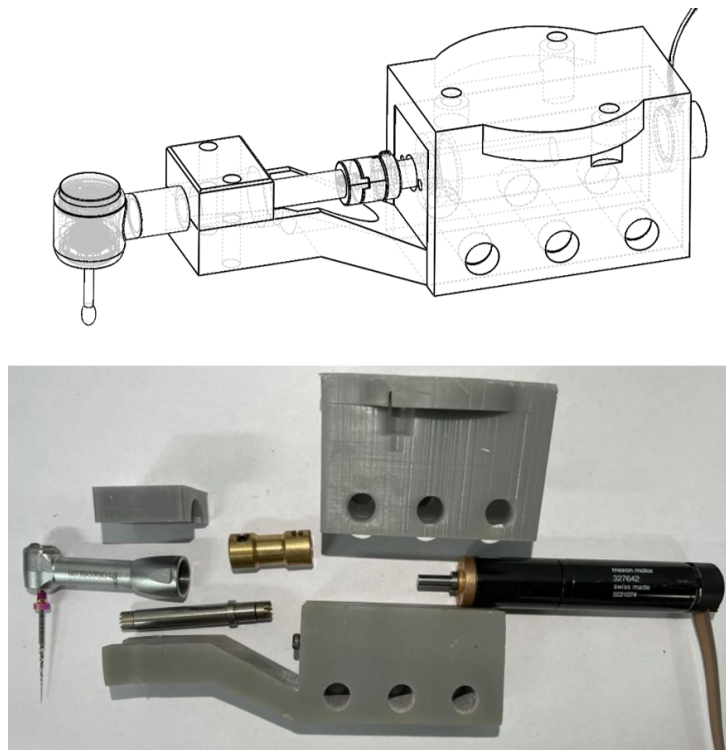


Figure 3.2: Modified dental handpiece composed of a servo motor, a coupler, and the endodontic file.

A coupler connects the existing handpiece and a servo motor so that the rotation of endodontic file is driven by the servo motor. There is a concern about assembly error because the coupler cannot maintain the motor and the existing handpiece in a straight line. The modified handpiece with a motor total weighs around 139 grams including the adapter used to assemble the F/T sensor and the handpiece. The weight of the modified handpiece is acceptable for the overloads of the F/T sensor and the robot arm.

In conclusion, DentiBot totally has seven degrees of freedom. Six degree of freedom come from Meca500, and the other is from the motor inside our modified handpiece. The rotation of the root canal file is driven by a servo motor, whose maximum rotation speed is around 200 rpm. The maximum rotation speed - 200 rpm is lower than the typical standard for endodontic treatment - 300 ~ 600 rpm. However, the clinical outcome of our proposed algorithm with 200 rpm is acceptable. It will be proven in Chapter 6. If needed, the rotation speed can be more faster by changing a higher quality motor.

### 3.3 Kinematics Analysis

In this section, coordinate definition is depicted followed by forward kinematics and Jacobian matrix.

#### Coordinate Definition

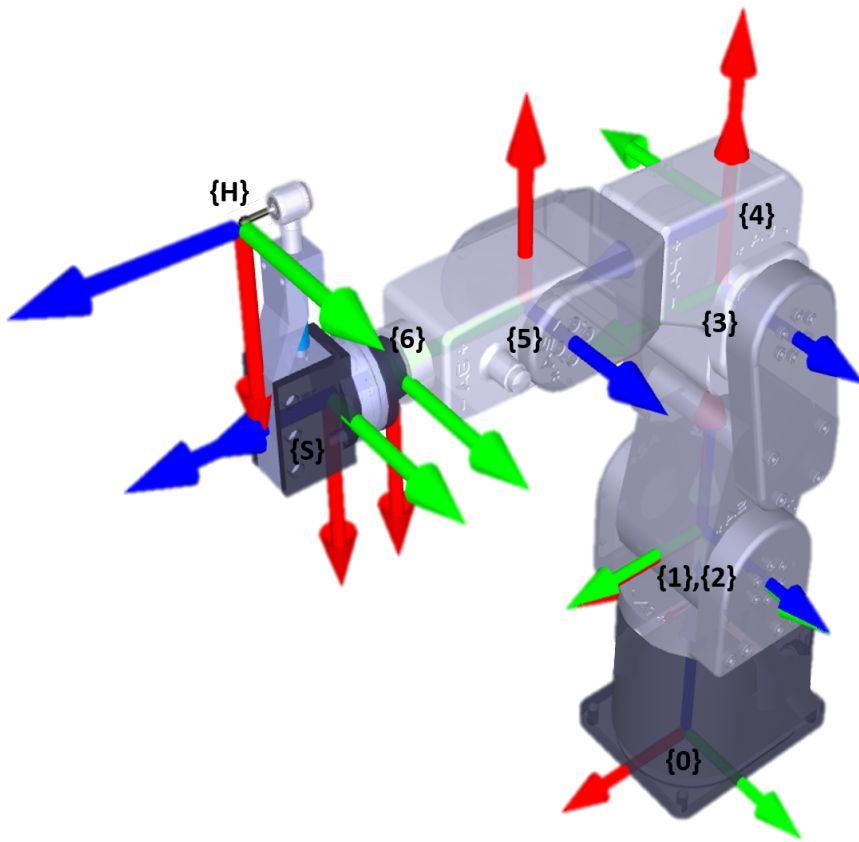


Figure 3.3: Coordinate definition of DentiBot. {0} to {6} represent frames of robot arm axes. {S} represents the frame of F/T sensor. {H} represents the handpiece tool-tip frame.

Table 3.1: Denavit-Hartenberg parameters of Meca500

$i$ (link number)	$\alpha_{i-1}$ (deg)	$a_{i-1}$ (mm)	$\theta_i$ (deg)	$d_i$ (mm)
1	0	0	$\theta_1$	135
2	-90	0	$\theta_2 - 90$	0
3	0	135	$\theta_3$	0
4	-90	38	$\theta_4$	120
5	90	0	$\theta_5$	0
6	-90	0	$\theta_6 + 180$	70

## Forward Kinematics

Denavit-Hartenberg parameters are shown as Table 3.1. Then, the forward kinematics of Meca500 is derived as

$${}^0\mathbf{T} = {}^0\mathbf{T} \cdot {}^1\mathbf{T} \cdot {}^2\mathbf{T} \cdot {}^3\mathbf{T} \cdot {}^4\mathbf{T} \cdot {}^5\mathbf{T} \cdot {}^6\mathbf{T} = \begin{bmatrix} {}^0\mathbf{R} & {}^0\mathbf{p}_6 \\ 0 & 1 \end{bmatrix} \quad (3.1)$$

where  ${}^0\mathbf{R}$  is the rotation matrix from frame{6} to frame{0},  ${}^0\mathbf{p}_6$  is the origin of the frame{6} observed from frame{0}. All detailed indexes of  ${}^0\mathbf{T}$  are shown in Appendix A.

By the way, there is an alternative to calculate the transformation matrix  ${}^0\mathbf{T}$  in real-time. The robot arm command – GetPose – provide position information ( $x$ ,  $y$ ,  $z$ ,  $\alpha$ ,  $\beta$ ,  $\gamma$ ). ( $x$ ,  $y$ ,  $z$ ) is exactly  ${}^0\mathbf{p}_6$ . ( $\alpha$ ,  $\beta$ ,  $\gamma$ ) are Euler angles and denote (raw,

pitch, yaw). Hence, we can use these information to derive the following equation.

$$\begin{aligned}
 {}^0_6\mathbf{T} &= \begin{bmatrix} {}^0_6\mathbf{R} & {}^0\mathbf{p}_6 \\ 0 & 1 \end{bmatrix} \\
 &= \begin{bmatrix} & & & x \\ & & & y \\ & & & z \\ \mathbf{R}_x(\alpha) \cdot \mathbf{R}_y(\beta) \cdot \mathbf{R}_z(\gamma) & & & \\ & & & \\ & & & \\ 0 & & & 1 \end{bmatrix} \\
 &= \begin{bmatrix} C_\beta C_\gamma & -C_\beta S_\gamma & S_\beta & x \\ C_\alpha S_\gamma + S_\alpha S_\beta C_\gamma & C_\alpha C_\gamma - s_\alpha S_\beta S_\gamma & -S_\alpha C_\beta & y \\ S_\alpha S_\gamma - C_\alpha S_\beta C_\gamma & S_\alpha C_\gamma + C_\alpha S_\beta S_\gamma & C_\alpha C_\beta & z \\ 0 & 0 & 0 & 1 \end{bmatrix} \tag{3.2}
 \end{aligned}$$

where  $C_\star, S_\star$  denote  $\cos(\star), \sin(\star)$ ;  $\alpha, \beta, \gamma$  are in representation of Euler angles.

## Jacobian matrix

Jacobian matrix has geometric Jacobian and analytical Jacobian. Therefore, geometric Jacobian based on frame{0}, geometric Jacobian based on frame{H}, and analytical Jacobian are evaluated in this subsection.

### Geometric Jacobian Based on Frame{0}

First, we should clarify the difference between geometric Jacobian and analytical Jacobian. They both use the same linear velocity but different angular velocity. The angular velocity which geometric Jacobian applies is relevant to the angular

velocity  $(\theta_x, \theta_y, \theta_z)$ . In contrast, the angular velocity which analytical Jacobian contemplates is related to the orientation  $(\alpha, \beta, \gamma)$  of the end effector. Therefore, the geometric Jacobian has a clear physical meaning due to the differential  $(\theta_x, \theta_y, \theta_z)$  is the angular velocity . Besides, because the geometric Jacobian can be considered in different frames, it is important to clearly understand and familiar with which frame is our option.

Before examining the geometric Jacobian matrix, it will be necessary to find the relationship between the position and joints' angles and the relationship between the angular velocity and the joints' angles.

Based on the translation matrix in Equation 3.1, we obtain the relationship between the position and joints' angles.

$${}^0\mathbf{p}_6 = \begin{bmatrix} x \\ y \\ z \end{bmatrix} = \begin{bmatrix} x(\theta_1, \theta_2, \dots, \theta_6) \\ y(\theta_1, \theta_2, \dots, \theta_6) \\ z(\theta_1, \theta_2, \dots, \theta_6) \end{bmatrix} \quad (3.3)$$

Moreover, the relationship between the angular velocity and derivative of joints' angles is

$$\begin{bmatrix} \dot{\theta}_x \\ \dot{\theta}_y \\ \dot{\theta}_z \end{bmatrix} = {}^0_1\mathbf{R} \begin{bmatrix} 0 \\ 0 \\ \theta_1 \end{bmatrix} + {}^0_2\mathbf{R} \begin{bmatrix} 0 \\ 0 \\ \theta_2 \end{bmatrix} + {}^0_3\mathbf{R} \begin{bmatrix} 0 \\ 0 \\ \theta_3 \end{bmatrix} + {}^0_4\mathbf{R} \begin{bmatrix} 0 \\ 0 \\ \theta_4 \end{bmatrix} + {}^0_5\mathbf{R} \begin{bmatrix} 0 \\ 0 \\ \theta_5 \end{bmatrix} + {}^0_6\mathbf{R} \begin{bmatrix} 0 \\ 0 \\ \theta_6 \end{bmatrix} \quad (3.4)$$

Therefore, Jacobian matrices can be obtained by differentiating Equation 3.3 and

3.4 as following equation

$$\begin{aligned} \mathbf{v} &= \begin{bmatrix} \dot{x} \\ \dot{y} \\ \dot{z} \end{bmatrix} = \mathbf{J}_{\mathbf{gv}} \cdot \dot{\boldsymbol{\theta}} \\ \mathbf{w} &= \begin{bmatrix} \dot{\theta}_x \\ \dot{\theta}_y \\ \dot{\theta}_z \end{bmatrix} = \mathbf{J}_{\mathbf{gw}} \cdot \dot{\boldsymbol{\theta}} \end{aligned} \quad (3.5)$$

where

$$\mathbf{J}_{\mathbf{gv}} = \begin{bmatrix} \frac{\partial x}{\partial \theta_1} & \frac{\partial x}{\partial \theta_2} & \dots & \frac{\partial x}{\partial \theta_6} \\ \frac{\partial y}{\partial \theta_1} & \frac{\partial y}{\partial \theta_2} & \dots & \frac{\partial y}{\partial \theta_6} \\ \frac{\partial z}{\partial \theta_1} & \frac{\partial z}{\partial \theta_2} & \dots & \frac{\partial z}{\partial \theta_6} \end{bmatrix}, \quad \mathbf{J}_{\mathbf{gw}} = \begin{bmatrix} \frac{\partial \theta_x}{\partial \theta_1} & \frac{\partial \theta_x}{\partial \theta_2} & \dots & \frac{\partial \theta_x}{\partial \theta_6} \\ \frac{\partial \theta_y}{\partial \theta_1} & \frac{\partial \theta_y}{\partial \theta_2} & \dots & \frac{\partial \theta_y}{\partial \theta_6} \\ \frac{\partial \theta_z}{\partial \theta_1} & \frac{\partial \theta_z}{\partial \theta_2} & \dots & \frac{\partial \theta_z}{\partial \theta_6} \end{bmatrix}, \quad \dot{\boldsymbol{\theta}} = \begin{bmatrix} \dot{\theta}_1 \\ \dot{\theta}_2 \\ \dot{\theta}_3 \\ \dot{\theta}_4 \\ \dot{\theta}_5 \\ \dot{\theta}_6 \end{bmatrix}$$

Then, the geometric Jacobian matrix based on frame  $\{0\}$   ${}^0\mathbf{J}_g$  is derived as

$${}^0\mathbf{J}_g = \begin{bmatrix} \mathbf{J}_{\mathbf{gv}} \\ \mathbf{J}_{\mathbf{gw}} \end{bmatrix}_{(6 \times 6)} \quad (3.6)$$

Finally, a relationship between  $\dot{\mathbf{x}}$  and  $\dot{\boldsymbol{\theta}}$  is derived as

$$\begin{aligned} \dot{\mathbf{x}} &= {}^0\mathbf{J}_g \cdot \dot{\boldsymbol{\theta}} \\ \dot{\boldsymbol{\theta}} &= {}^0\mathbf{J}_g^{-1} \cdot \dot{\mathbf{x}} \end{aligned} \quad (3.7)$$

where

$$\dot{\mathbf{x}} = \begin{bmatrix} \dot{x} \\ \dot{y} \\ \dot{z} \\ \dot{\theta}_x \\ \dot{\theta}_y \\ \dot{\theta}_z \end{bmatrix}_{\{0\}}, \quad \dot{\boldsymbol{\theta}} = \begin{bmatrix} \dot{\theta}_1 \\ \dot{\theta}_2 \\ \dot{\theta}_3 \\ \dot{\theta}_4 \\ \dot{\theta}_5 \\ \dot{\theta}_6 \end{bmatrix}$$

By extension, in terms of the Jacobian matrix, the property between joint torque

and force can be derived as

$$\begin{aligned} \boldsymbol{\tau} &= {}^0\mathbf{J}_g^\top \cdot \mathbf{f} \\ \Rightarrow \begin{bmatrix} \tau_{\theta_1} \\ \tau_{\theta_2} \\ \tau_{\theta_3} \\ \tau_{\theta_4} \\ \tau_{\theta_5} \\ \tau_{\theta_6} \end{bmatrix} &= {}^0\mathbf{J}_g^\top \cdot \begin{bmatrix} f_x \\ f_y \\ f_z \\ \tau_x \\ \tau_y \\ \tau_z \end{bmatrix} \end{aligned} \quad (3.8)$$

where  $\boldsymbol{\tau}$  is the vector of joints' torques and  $\mathbf{f}$  is the vector composed of inertial forces and torques of the robot arm.

### Geometric Jacobian Based on Frame{H}

Why the geometric Jacobian based on frame{H}  ${}^H\mathbf{J}_g$  is important is that in section 4.3 admittance control is applied and use F/T sensor detect forces and torques relative to frame{H} instead of frame{0}.

To obtain  ${}^H\mathbf{J}_g$ , we derive it from  ${}^0\mathbf{J}_g$ . Therefore, to start with Equation 3.7.

$$\begin{bmatrix} \dot{x} \\ \dot{y} \\ \dot{z} \\ \dot{\theta}_x \\ \dot{\theta}_y \\ \dot{\theta}_z \end{bmatrix}_{\{0\}} = {}^0\mathbf{J}_g \cdot \begin{bmatrix} \dot{\theta}_1 \\ \dot{\theta}_2 \\ \dot{\theta}_3 \\ \dot{\theta}_4 \\ \dot{\theta}_5 \\ \dot{\theta}_6 \end{bmatrix} \quad (3.9)$$

Then, left-multiply an augmented rotation matrix composed of  ${}^0_R$ .

$$\begin{bmatrix} {}^H_R & 0_{3 \times 3} \\ 0_{3 \times 3} & {}^H_R \end{bmatrix} \cdot \begin{bmatrix} \dot{x} \\ \dot{y} \\ \dot{z} \\ \dot{\theta}_x \\ \dot{\theta}_y \\ \dot{\theta}_z \end{bmatrix}_{\{0\}} = \begin{bmatrix} {}^H_R & 0_{3 \times 3} \\ 0_{3 \times 3} & {}^H_R \end{bmatrix} \cdot {}^0\mathbf{J}_g \cdot \begin{bmatrix} \dot{\theta}_1 \\ \dot{\theta}_2 \\ \dot{\theta}_3 \\ \dot{\theta}_4 \\ \dot{\theta}_5 \\ \dot{\theta}_6 \end{bmatrix} \quad (3.10)$$

Since the transformation coordinate relationship between frame{0} and frame{6}

is

$$\begin{bmatrix} \dot{x} \\ \dot{y} \\ \dot{z} \\ \dot{\theta}_x \\ \dot{\theta}_y \\ \dot{\theta}_z \end{bmatrix}_{\{H\}} = \begin{bmatrix} {}^H_R & 0_{3 \times 3} \\ 0_{3 \times 3} & {}^H_R \end{bmatrix} \begin{bmatrix} \dot{x} \\ \dot{y} \\ \dot{z} \\ \dot{\theta}_x \\ \dot{\theta}_y \\ \dot{\theta}_z \end{bmatrix}_{\{0\}} \quad (3.11)$$

Substitute Equation 3.11 into Equation 3.10.

$$\begin{bmatrix} \dot{x} \\ \dot{y} \\ \dot{z} \\ \dot{\theta}_x \\ \dot{\theta}_y \\ \dot{\theta}_z \end{bmatrix}_{\{H\}} = \begin{bmatrix} {}^H\mathbf{R} & 0_{3 \times 3} \\ 0_{3 \times 3} & {}^H\mathbf{R} \end{bmatrix} \cdot {}^0\mathbf{J}_g \cdot \begin{bmatrix} \dot{\theta}_1 \\ \dot{\theta}_2 \\ \dot{\theta}_3 \\ \dot{\theta}_4 \\ \dot{\theta}_5 \\ \dot{\theta}_6 \end{bmatrix} \quad (3.12)$$

Because

$$\dot{\mathbf{x}} = {}^H\mathbf{J}_g \cdot \dot{\boldsymbol{\theta}} \quad (3.13)$$

where

$$\dot{\mathbf{x}} = \begin{bmatrix} \dot{x} \\ \dot{y} \\ \dot{z} \\ \dot{\theta}_x \\ \dot{\theta}_y \\ \dot{\theta}_z \end{bmatrix}_{\{H\}}, \quad \dot{\boldsymbol{\theta}} = \begin{bmatrix} \dot{\theta}_1 \\ \dot{\theta}_2 \\ \dot{\theta}_3 \\ \dot{\theta}_4 \\ \dot{\theta}_5 \\ \dot{\theta}_6 \end{bmatrix}$$

Therefore the relationship between  ${}^H\mathbf{J}_g$  and  ${}^0\mathbf{J}_g$  is obtained.

$${}^H\mathbf{J}_g = \begin{bmatrix} {}^H\mathbf{R} & 0_{3 \times 3} \\ 0_{3 \times 3} & {}^H\mathbf{R} \end{bmatrix} \cdot {}^0\mathbf{J}_g \quad (3.14)$$

In conclusion,  ${}^H\mathbf{J}_g$  can be derived from  ${}^0\mathbf{J}_g$ , and then we can analyze kinematics on frame  $\{H\}$  with  ${}^H\mathbf{J}_g$ .

### Analytical Jacobian

The linear velocity of analytical Jacobian and geometric Jacobian is the same as shown in Equation 3.3. Nevertheless, as for angular velocity, analytical Jacobian takes the orientation  $(\alpha, \beta, \gamma)$  of the end effector into consideration.

Analytical Jacobian can be derived from geometric Jacobian. First, we investigate the relationship between the angular velocity and derivative of orientation of the end effector as following.

$$\begin{aligned} \begin{bmatrix} \theta_x \\ \theta_y \\ \theta_z \end{bmatrix} &= \begin{bmatrix} \alpha \\ 0 \\ 0 \end{bmatrix} + \mathbf{R}_x(\alpha) \begin{bmatrix} 0 \\ \beta \\ 0 \end{bmatrix} + \mathbf{R}_x(\alpha)\mathbf{R}_y(\beta) \begin{bmatrix} 0 \\ 0 \\ \gamma \end{bmatrix} \\ &= \begin{bmatrix} 1 & 0 & S_\beta \\ 0 & C_\alpha & -S_\alpha C_\beta \\ 0 & S_\alpha & C_\alpha C_\beta \end{bmatrix} \begin{bmatrix} \alpha \\ \beta \\ \gamma \end{bmatrix} \end{aligned} \quad (3.15)$$

Then, utilize this generalized vector to get its Jacobian matrix  $\mathbf{J}_{we}$ .

$$\begin{bmatrix} \dot{\theta}_x \\ \dot{\theta}_y \\ \dot{\theta}_z \end{bmatrix} = \mathbf{J}_{we} \cdot \begin{bmatrix} \dot{\alpha} \\ \dot{\beta} \\ \dot{\gamma} \end{bmatrix} \quad (3.16)$$

where

$$\mathbf{J}_{we} = \begin{bmatrix} 1 & \gamma C_\beta & S_\beta \\ -\beta S_\alpha - \gamma C_\alpha C_\beta & C_\alpha + \gamma S_\alpha S_\beta & -C_\beta S_\alpha \\ \beta C_\alpha - \gamma C_\beta S_\alpha & S_\alpha - \gamma C_\alpha S_\beta & C_\alpha C_\beta \end{bmatrix}$$

Therefore,

$$\begin{bmatrix} \dot{x} \\ \dot{y} \\ \dot{z} \\ \dot{\theta}_x \\ \dot{\theta}_y \\ \dot{\theta}_z \end{bmatrix} = \begin{bmatrix} \mathbf{I}_{3 \times 3} & 0_{3 \times 3} \\ 0_{3 \times 3} & \mathbf{J}_{\text{we}} \end{bmatrix} \begin{bmatrix} \dot{x} \\ \dot{y} \\ \dot{z} \\ \dot{\alpha} \\ \dot{\beta} \\ \dot{\gamma} \end{bmatrix} \quad (3.17)$$

Finally, we obtain the relationship between geometric and analytical Jacobian.

$$\begin{aligned} \mathbf{J}_g &= \begin{bmatrix} \mathbf{I}_{3 \times 3} & 0_{3 \times 3} \\ 0_{3 \times 3} & \mathbf{J}_{\text{we}} \end{bmatrix} \mathbf{J}_a \\ \mathbf{J}_a &= \begin{bmatrix} \mathbf{I}_{3 \times 3} & 0_{3 \times 3} \\ 0_{3 \times 3} & \mathbf{J}_{\text{we}}^{-1} \end{bmatrix} \mathbf{J}_g \end{aligned} \quad (3.18)$$

### 3.4 Tool-tip Coordinate

To obtain translation and rotation vector, we respectively introduce Tool Center Point to find the translation vector and propose an approach to find the rotation vector.

#### Translation Analysis - Tool Center Point

So far, with the forward and inverse kinematics, the robot arm can translate and rotate around frame{6}. However, the origin of the frame{6} is not an operating point. Because the F/T sensor and a detachable end effector will be both mounted

on the wrist, the tool-tip position is what we want. That means we should let the robot arm know how to translate and rotate in frame{H} instead of frame{6}. If we have translation and rotation information of the tool-tip, there is an easy way to directly give the above information to the robot arm. SetTRF ( $x, y, z, \alpha, \beta, \gamma$ ) is the command of the robot arm, whose  $(x, y, z)$  is translation vector and  $(\alpha, \beta, \gamma)$  is rotation vector in representation of Euler angles.

Tool Center Point (TCP) is a critical problem for robot arm control [29]. In the previous section, the forward kinematics of the robot arm have evaluated. By Calculating kinematics, The robot arm can keep track of the origin of the frame{6}, which is observed from the base frame. The robot arm has the capability to translate and rotate with the origin of the frame{6}. The above motions are like a remote center motion (RCM). Nevertheless, it's inefficient to recalculate the transformation matrix via mechanism dimension when changing an end effector or a tool (endodontic file). Besides, using forward kinematics to find the tool-tip frame can not avoid assembly errors.

In order to overcome this problem, the four-points method is interpreted to obtain the tool-tip position information, which is also the translation vector. From Figure 3.3, the transformation matrix between the frame{0} and frame{H} is evaluated as

$${}^0_H T = {}^0_6 T \cdot {}^6_H T \quad (3.19)$$

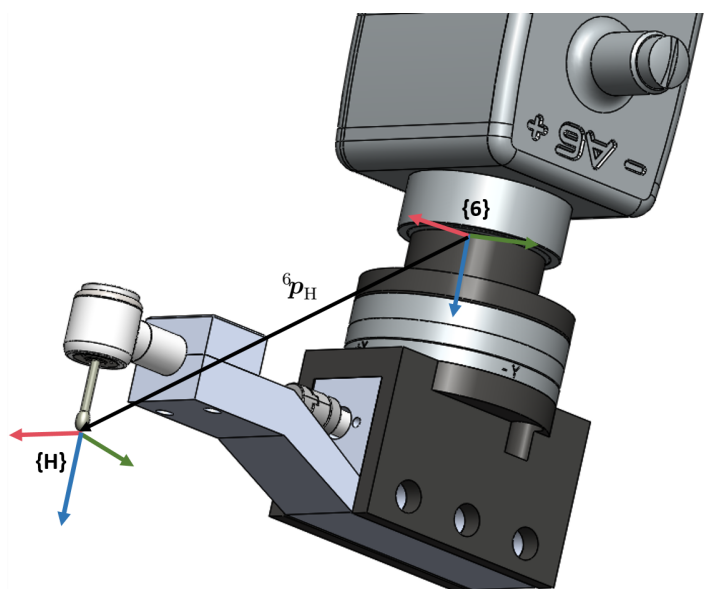


Figure 3.4: Schematic diagram for tool center point (TCP). The translation vector  ${}^6p_H$  denotes the origin position relative to the frame {6}.

and can be rewritten as

$$\begin{aligned} \begin{bmatrix} {}_H^0\mathbf{R} & {}_0\mathbf{p}_H \\ 0 & 1 \end{bmatrix} &= \begin{bmatrix} {}_6^0\mathbf{R} & {}_0\mathbf{p}_6 \\ 0 & 1 \end{bmatrix} \begin{bmatrix} {}_H^6\mathbf{R} & {}_6\mathbf{p}_H \\ 0 & 1 \end{bmatrix} \\ &= \begin{bmatrix} {}_6^0\mathbf{R} \cdot {}_H^6\mathbf{R} & {}_6^0\mathbf{R} \cdot {}_6\mathbf{p}_H + {}_0\mathbf{p}_6 \\ 0 & 1 \end{bmatrix} \end{aligned} \quad (3.20)$$

where  $\mathbf{R}$  is the rotation matrix,  ${}^0\mathbf{p}_6$  is the origin of the frame{6} observed from frame{0}, and  ${}^6\mathbf{p}_H$  is the origin of the frame{H} observed from frame{6}. Consequently, a crucial equation is obtained

$${}^0\mathbf{p}_H = {}_6^0\mathbf{R} \cdot {}^6\mathbf{p}_H + {}^0\mathbf{p}_6 \quad (3.21)$$

Now, we move the tool-tip to a fixed point with four different poses including position and orientation as shown in Figure 3.5. Then, four different rotation matrices and vectors are derived.

$$\begin{aligned} {}^0\mathbf{p}_H &= {}_6^0\mathbf{R}^1 \cdot {}^6\mathbf{p}_H + {}^0\mathbf{p}_6^1 \\ &= {}_6^0\mathbf{R}^2 \cdot {}^6\mathbf{p}_H + {}^0\mathbf{p}_6^2 \\ &= {}_6^0\mathbf{R}^3 \cdot {}^6\mathbf{p}_H + {}^0\mathbf{p}_6^3 \\ &= {}_6^0\mathbf{R}^4 \cdot {}^6\mathbf{p}_H + {}^0\mathbf{p}_6^4 \end{aligned} \quad (3.22)$$

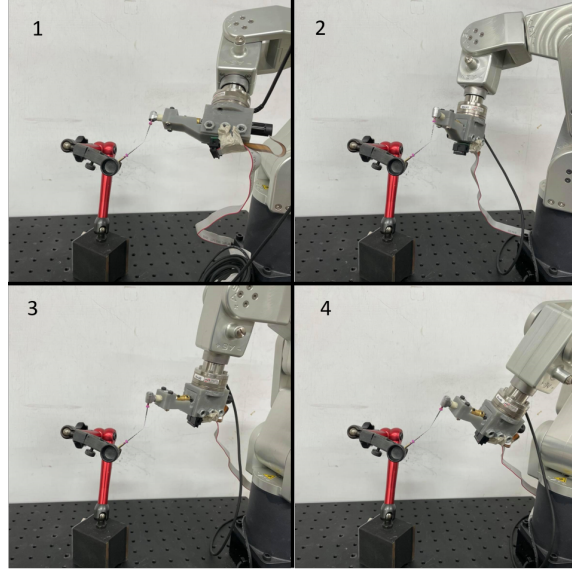


Figure 3.5: Four points method. Align a fixed point with four different poses.

${}^6\mathbf{p}_H$  is unknown. In order to extract  ${}^6\mathbf{p}_H$  from Equation 3.22, we subtract the second to forth equation from the first equation.

$$\begin{bmatrix} {}^0\mathbf{R}^1 - {}^0\mathbf{R}^2 \\ {}^0\mathbf{R}^1 - {}^0\mathbf{R}^3 \\ {}^0\mathbf{R}^1 - {}^0\mathbf{R}^4 \end{bmatrix} \cdot {}^6\mathbf{p}_H = \begin{bmatrix} {}^0\mathbf{p}_6^2 - {}^0\mathbf{p}_6^1 \\ {}^0\mathbf{p}_6^3 - {}^0\mathbf{p}_6^1 \\ {}^0\mathbf{p}_6^4 - {}^0\mathbf{p}_6^1 \end{bmatrix} \quad (3.23)$$

where we define

$$\mathbf{R} = \begin{bmatrix} {}^0\mathbf{R}^1 - {}^0\mathbf{R}^2 \\ {}^0\mathbf{R}^1 - {}^0\mathbf{R}^3 \\ {}^0\mathbf{R}^1 - {}^0\mathbf{R}^4 \end{bmatrix}_{9 \times 3}, \mathbf{p} = \begin{bmatrix} {}^0\mathbf{p}_6^2 - {}^0\mathbf{p}_6^1 \\ {}^0\mathbf{p}_6^3 - {}^0\mathbf{p}_6^1 \\ {}^0\mathbf{p}_6^4 - {}^0\mathbf{p}_6^1 \end{bmatrix}_{9 \times 1}$$

Therefore,

$$\begin{aligned} {}^6\mathbf{p}_H &= \mathbf{R}^\dagger \cdot \mathbf{p} \\ &= (\mathbf{R}^\top \mathbf{R})^{-1} \mathbf{R}^\top \cdot \mathbf{p} \end{aligned}$$

Finally, we can utilize the four-points method to obtain the translation vector  ${}^6\mathbf{p}_H$ .

### Rotation Analysis

Turning now to the discussion about the rotation vector. Above all, the vector of tool insertion direction  $t$  should be obtained. By applying the TCP method with two endodontic files with different lengths, two vectors  ${}^6p_{H_{\text{long}}}$ ,  ${}^6p_{H_{\text{short}}}$  are obtained and illustrated as Figure 3.6. Hence,

$$t = {}^6p_{H_{\text{long}}} - {}^6p_{H_{\text{short}}} \quad (3.24)$$

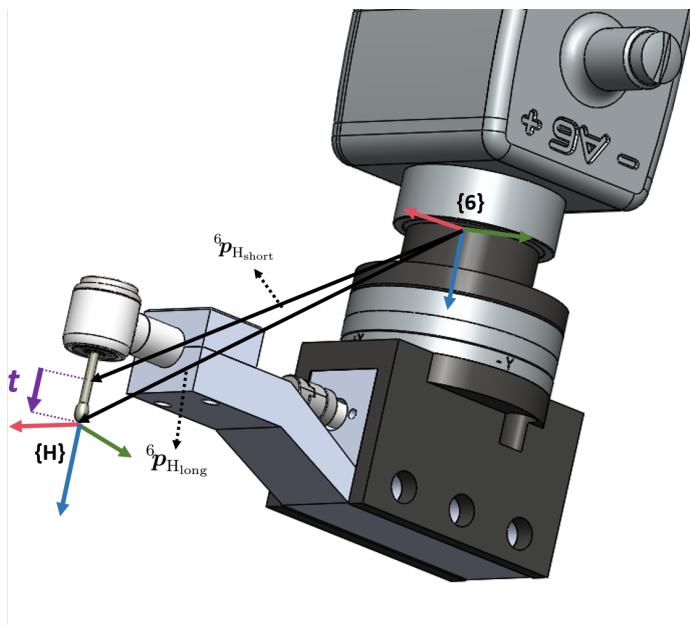


Figure 3.6: Schematic diagram for obtaining the tool vector.

For analyzing it easily, we depict it in Figure 3.7. Note that here we only discuss rotation, so we assume that we have done translation and matched the frame  $\{H\}$  with frame  $\{6\}$ . Because we hope to send a Z-axis command to achieve

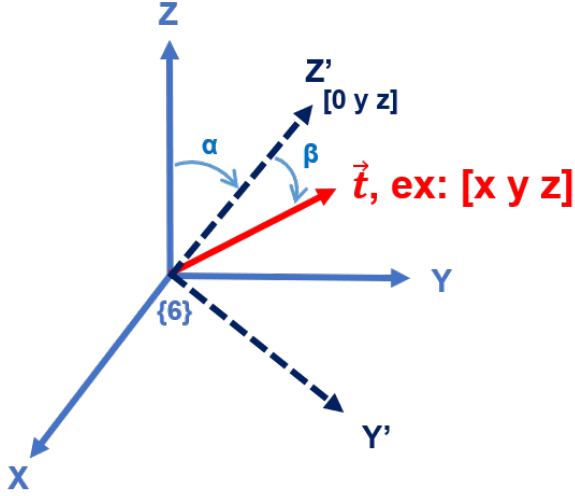


Figure 3.7: Illustration of finding the rotation matrix with the tool vector

tool insertion, we should align the original Z-axis to the tool vector  $\mathbf{t}$ . Nevertheless, Z-axis alignment without other restrictions will produce many solutions. We choose one of the solutions to align Z-axis to the tool vector. According to the figure, we assume the tool vector  $\mathbf{t}$  is  $[t_x \ t_y \ t_z]$ , whose projection to yz-plane  $\text{proj}_{(y-z)}\mathbf{t}$  is  $[0 \ t_y \ t_z]$ . Initially, we rotate  $\alpha$  degree around X-axis to make original Z-axis align the projection  $[0 \ y \ z]$ . Next, we rotate  $\beta$  degree around Y' axis and finally align the original Z-axis to the tool vector  $[t_x \ t_y \ t_z]$ . Therefore,

$${}^H_6\mathbf{R} = \mathbf{R}_x(\alpha)\mathbf{R}_y(\beta) \quad (3.25)$$

, and

$$\begin{aligned} \alpha &= -\text{sign}(t_y) \cdot \cos^{-1} \left( \frac{\hat{k} \cdot \text{proj}_{(y-z)}\mathbf{t}}{\|\hat{k}\| \cdot \|\text{proj}_{(y-z)}\mathbf{t}\|} \right) \\ \beta &= \text{sign}(t_x) \cdot \cos^{-1} \left( \frac{\mathbf{t} \cdot \text{proj}_{(y-z)}\mathbf{t}}{\|\mathbf{t}\| \cdot \|\text{proj}_{(y-z)}\mathbf{t}\|} \right) \end{aligned} \quad (3.26)$$

where  $\alpha, \beta$  are Euler angles which could be applied with the robot command "SetTCP",  $\hat{k}$  is the unit vector of in the direction of the z-axis, and  $t, [t_x \ t_y \ t_z]$ , is the tool vector.

In this section, we have demonstrated two key aspects of reference frame changing of the robot arm. By the translation and rotation information, it's easy to input the results of them via the command setTRF. The robot arm can recognize frame{H}, then translate and orientate along with frame{H}. Having discussed how to combine a robot arm with an end effector, the next section addresses ways of combining an F/T sensor.

# Chapter 4

## Force-Guided Robot Alignment

In this chapter, an Forces and Torques (F/T) sensor is involved and force-guided robot alignment is proposed. Problem definition is addressed in section 4.1 followed by Integration of F/T sensor in section 4.2. Admittance control based on F/T sensor is described in section 4.3. Coordinate transformation of F/T sensor will be interpreted in section 4.4. Parameter selection of admittance control is discussed in section 4.5.

### 4.1 Problem Definition and Proposed Method

In this section, problem definition is addressed followed by a brief introduction of proposed method.

#### Problem Definition

In modern robot-assisted surgery, to simulate the eyes of doctors, image processing is often considered. With the image's information, the surgeon can obtain real-time data that humans can not observe clearly. Surgeons use the image process to do many things, such as tracking whether the patient is moving, positioning an incision point, and navigating an insertion path. As for root canal treatment, the

endodontist checks the number of root canals with computed tomography. Before starting to clean the pulp, the endodontist tries to insert root files into root canals. Then the endodontist takes the patient to have computed tomography(CT). CT scan can clearly show the tooth with the root files. With the preoperative image, the endodontist can check whether all root canals are all found and determine all root canals' lengths. However, the above image application is preoperative. The endodontist can only use the preoperative image to guess the direction of the insertion. The intraoperative image processing is absent due to the dimension restriction of a tooth. It is difficult to get a real-time image when the dentist inserts a root file into the opened tooth because it will obstacle the observation. Besides, the diameter of a root canal is 1 mm and is smaller than a root file. It is impossible to get the image from any shooting angle.

### **Proposed Method**

To solve the first problem – without image processing, admittance control based on F/T sensor is reviewed. The literature on peg-in-hole based on F/T sensor [30, 31, 32, 33] are surveyed because the cleaning procedure is similar to it. To apply in different situation, two operating modes – "Dragging Mode" and "Self-Alignment Mode" are designed. In "Dragging Mode", Dentists can hold the handpiece to the desired position and orientation. In "Self-Alignment Mode", the handpiece can automatically align the root canal direction with any complicated conditions. Two modes are set by change reference frame and parameter setting.

## 4.2 Integration of F/T sensor

In this section, technical solution to system integration with an F/T sensor is discussed. In Figure 4.1 shows that initial value and gravity load both affect the value of F/T sensor. Hence, in this section, initial value are obtained off-line and gravity load is compensated in real-time. Finally, external force evaluation is discussed.

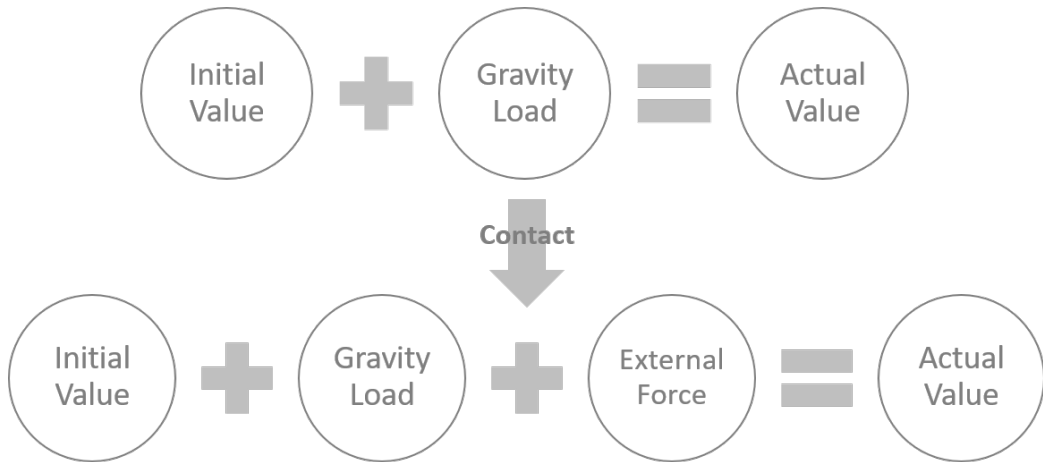


Figure 4.1: Data analysis of F/T sensor. Initial Value is the initial value of F/T sensor without reset. Gravity Load is the gravity of end effector. External Force is the value of force or torque.

### Gravity Compensation and Initial Value Reset

Gravity compensation is a critical technical issue when combining an F/T sensor with a robot arm and an end effector [34]. Fundamentally, stable data is

received when a static F/T sensor bears the same load or force. Nevertheless, our F/T sensor is installed on the robot arm and move with the pose of the robot arm. On account of its mobility, the gravity of the end effector will significantly affect the actual value we received. Moreover, starting without resetting the F/T sensor to zero would lead to an initial value. If we could not analyze the actual value to an initial value and a gravity load, we would obtain an unstable actual value, not to mention the external force caused by contact force. Therefore, we illustrate a method, which is to analyze the actual value of the F/T sensor to an initial value and gravity load in real-time. It's worth noting that with this approach, we can get the installation angle between the F/T sensor and the robot arm, including assembly error, and we no longer need to reset the F/T sensor to zero every time.

The actual value measured by F/T sensor is expressed as  $[f_x \ f_y \ f_z \ \tau_x \ \tau_y \ \tau_z]$ , which is affected by initial value expressed as  $[f_{0x} \ f_{0y} \ f_{0z} \ \tau_{0x} \ \tau_{0y} \ \tau_{0z}]$  and gravity load expressed as  $[f_{gx} \ f_{gy} \ f_{gz} \ \tau_{gx} \ \tau_{gy} \ \tau_{gz}]$ . Initial value is the value without resetting F/T sensor and gravity load is the gravity of the end effector.

$$\text{Actual Value} = \text{Initial value} + \text{Gravity Load}$$

$${}^S\boldsymbol{f} = {}^S\boldsymbol{f}_0 + {}^S\boldsymbol{f}_g \quad (4.1)$$

$${}^S\boldsymbol{\tau} = {}^S\boldsymbol{\tau}_0 + {}^S\boldsymbol{\tau}_g$$

where

$$\begin{aligned} {}^S\mathbf{f} &= \begin{bmatrix} f_x \\ f_y \\ f_z \end{bmatrix}, \quad {}^S\mathbf{f}_0 = \begin{bmatrix} f_{0x} \\ f_{0y} \\ f_{0z} \end{bmatrix}, \quad {}^S\mathbf{f}_g = \begin{bmatrix} f_{gx} \\ f_{gy} \\ f_{gz} \end{bmatrix} \\ {}^S\boldsymbol{\tau} &= \begin{bmatrix} \tau_x \\ \tau_y \\ \tau_z \end{bmatrix}, \quad {}^S\boldsymbol{\tau}_0 = \begin{bmatrix} \tau_{0x} \\ \tau_{0y} \\ \tau_{0z} \end{bmatrix}, \quad {}^S\boldsymbol{\tau}_g = \begin{bmatrix} \tau_{gx} \\ \tau_{gy} \\ \tau_{gz} \end{bmatrix} \end{aligned}$$

And, by terms of moment arm formula,

$${}^S\boldsymbol{\tau}_g = \mathbf{r} \times {}^S\mathbf{f}_g \quad (4.2)$$

where  $\mathbf{r}$  denotes the centroid position of the end effector on frame {S} and

$$\mathbf{r} = \begin{bmatrix} x \\ y \\ z \end{bmatrix}$$

Combines Equation 4.1 and Equation 4.2,

$$\begin{aligned} {}^S\boldsymbol{\tau} &= {}^S\boldsymbol{\tau}_0 + {}^S\boldsymbol{\tau}_g \\ &= {}^S\boldsymbol{\tau}_0 + \mathbf{r} \times {}^S\mathbf{f}_g \\ &= {}^S\boldsymbol{\tau}_0 + \mathbf{r} \times ({}^S\mathbf{f} - {}^S\mathbf{f}_0) \end{aligned} \quad (4.3)$$

Then, Equation 4.3 can be extend as

$$\begin{aligned} \tau_x &= \tau_{0x} + (f_z - f_{0z}) \cdot y - (f_y - f_{0y}) \cdot z \\ \tau_y &= \tau_{0y} + (f_x - f_{0x}) \cdot z - (f_z - f_{0z}) \cdot x \\ \tau_z &= \tau_{0z} + (f_y - f_{0y}) \cdot x - (f_x - f_{0x}) \cdot y \end{aligned} \quad (4.4)$$

and be overwritten as

$$\begin{bmatrix} \tau_x \\ \tau_y \\ \tau_z \end{bmatrix} = \begin{bmatrix} 0 & f_z & -f_y & 1 & 0 & 0 \\ -f_z & 0 & f_x & 0 & 1 & 0 \\ f_y & -f_x & 0 & 0 & 0 & 1 \end{bmatrix} \begin{bmatrix} x \\ y \\ z \\ k_1 \\ k_2 \\ k_3 \end{bmatrix} \quad (4.5)$$

where  $k_1, k_2, k_3$  are all constants and

$$\begin{aligned} k_1 &= \tau_{0x} - (f_{0z} \cdot y + f_{0y} \cdot z) \\ k_2 &= \tau_{0y} - (f_{0x} \cdot z + f_{0z} \cdot x) \\ k_3 &= \tau_{0z} - (f_{0y} \cdot x + f_{0x} \cdot y) \end{aligned} \quad (4.6)$$

$[x, y, z, k_1, k_2, k_3]$  is an unknown vector. To extract it, the robot arm moves to  $n$  ( $n \geq 3$ ) positions with different poses. By recording  $n$  torque vectors and

corresponding  $n$  force vectors from F/T sensor, Equation 4.5 is expanded to

$$\begin{bmatrix} \tau_x^1 \\ \tau_y^1 \\ \tau_z^1 \\ \tau_x^2 \\ \tau_y^2 \\ \tau_z^2 \\ \vdots \\ \tau_x^n \\ \tau_y^n \\ \tau_z^n \end{bmatrix} = \begin{bmatrix} 0 & f_z^1 & -f_y^1 & 1 & 0 & 0 \\ -f_z^1 & 0 & f_x^1 & 0 & 1 & 0 \\ f_y^1 & -f_x^1 & 0 & 0 & 0 & 1 \\ 0 & f_z^2 & -f_y^2 & 1 & 0 & 0 \\ -f_z^2 & 0 & f_x^2 & 0 & 1 & 0 \\ f_y^2 & -f_x^2 & 0 & 0 & 0 & 1 \\ \vdots & & \vdots & & & \\ 0 & f_z^3 & -f_y^3 & 1 & 0 & 0 \\ -f_z^3 & 0 & f_x^3 & 0 & 1 & 0 \\ f_y^3 & -f_x^3 & 0 & 0 & 0 & 1 \end{bmatrix} \begin{bmatrix} x \\ y \\ z \\ k_1 \\ k_2 \\ k_3 \end{bmatrix} \quad (4.7)$$

which is defined as

$$\mathbf{m}_{(3n \times 1)} = \mathbf{F}_{(3n \times 6)} \cdot \mathbf{p}_{(6 \times 1)}$$

Due to the full column rank of  $\mathbf{F}$ , Moore-Penrose pseudoinverse is applied here.

Then,

$$\begin{aligned} \mathbf{p} &= \mathbf{F}^\dagger \cdot \mathbf{m} \\ &= (\mathbf{F}^\top \mathbf{F})^{-1} \mathbf{F}^\top \cdot \mathbf{m} \end{aligned}$$

So far, we have obtained a middle information  $[x \ y \ z \ k_1 \ k_2 \ k_3]$ . Note that  $[x \ y \ z]$  is the centroid position of end effector related to the sensor frame.  $[k_1 \ k_2 \ k_3]$  is still coupled by initial forces  $[f_{0x} \ f_{0y} \ f_{0z}]$  and torque values  $[\tau_{0x} \ \tau_{0y} \ \tau_{0z}]$ .

To decouple  $[k_1 \ k_2 \ k_3]$ , let us return to the first equation in Figure 4.1. We continue to use this formula and contemplate it from the perspective of coordinate

transformation relation. Here we hypothesize that the end effector weighs  $g$  kilograms relative to the frame{0} which is also the world frame. That means the gravity vector of the end effector  ${}^0\mathbf{g}$  is  $[0 \ 0 \ -g]$  related to the frame{0}. Then,

$$\text{Actual Value} = \text{Initial value} + \text{Gravity Load}$$

$$\begin{aligned} \Rightarrow {}^S\mathbf{f} &= {}^S\mathbf{f}_0 + {}^S\mathbf{f}_g \\ &= {}^S\mathbf{f}_0 + {}^S\mathbf{R} \cdot {}_0^6\mathbf{R} \cdot {}^0\mathbf{g} \end{aligned} \quad (4.8)$$

where an installation angle  $\theta$  including assembly error is assumed and

$${}^S\mathbf{R} = \begin{bmatrix} \cos(\theta) & \sin(\theta) & 0 \\ -\sin(\theta) & \cos(\theta) & 0 \\ 0 & 0 & 1 \end{bmatrix} \quad (4.9)$$

Besides, we can easily calculate  ${}^6\mathbf{R}$  from forward kinematics in Equation 3.1.

$$\begin{aligned} {}^6\mathbf{R} &= {}^0\mathbf{R}^\top \\ &:= \begin{bmatrix} r_{11} & r_{12} & r_{13} \\ r_{21} & r_{22} & r_{23} \\ r_{31} & r_{32} & r_{33} \end{bmatrix} \end{aligned} \quad (4.10)$$

Therefore,

$$\begin{bmatrix} f_x \\ f_y \\ f_z \end{bmatrix} = \begin{bmatrix} f_{0x} \\ f_{0y} \\ f_{0z} \end{bmatrix} + \begin{bmatrix} \cos(\theta) & \sin(\theta) & 0 \\ -\sin(\theta) & \cos(\theta) & 0 \\ 0 & 0 & 1 \end{bmatrix} \begin{bmatrix} r_{11} & r_{12} & r_{13} \\ r_{21} & r_{22} & r_{23} \\ r_{31} & r_{32} & r_{33} \end{bmatrix} \begin{bmatrix} 0 \\ 0 \\ -g \end{bmatrix} \quad (4.11)$$

Note that it is discussed on frame{S}.

Equation 4.11 can be rewritten as

$$\begin{bmatrix} -r_{13} & -r_{23} & 0 & 1 & 0 & 0 \\ -r_{23} & r_{13} & 0 & 0 & 1 & 0 \\ 0 & 0 & -r_{33} & 0 & 0 & 1 \end{bmatrix} \begin{bmatrix} g \cos(\theta) \\ g \sin(\theta) \\ g \\ f_{0x} \\ f_{0y} \\ f_{0z} \end{bmatrix} = \begin{bmatrix} f_x \\ f_y \\ f_z \end{bmatrix} \quad (4.12)$$

$[g \cos(\theta), g \sin(\theta), g, f_{0x}, f_{0y}, f_{0z}]$  is an unknown vector and is extracted by the least square solution. First,  $n(n \geq 3)$  third columns of ration matrices and corresponding  $n$  force vectors from F/T sensor are recorded in real-time. Therefore, Equation 4.12 can be expended as

$$\begin{bmatrix} -r_{13}^1 & -r_{23}^1 & 0 & 1 & 0 & 0 \\ -r_{23}^1 & r_{13}^1 & 0 & 0 & 1 & 0 \\ 0 & 0 & -r_{33}^1 & 0 & 0 & 1 \\ -r_{13}^2 & -r_{23}^2 & 0 & 1 & 0 & 0 \\ -r_{23}^2 & r_{13}^2 & 0 & 0 & 1 & 0 \\ 0 & 0 & -r_{33}^2 & 0 & 0 & 1 \\ \vdots & & & & & \\ -r_{13}^n & -r_{23}^n & 0 & 1 & 0 & 0 \\ -r_{23}^n & r_{13}^n & 0 & 0 & 1 & 0 \\ 0 & 0 & -r_{33}^n & 0 & 0 & 1 \end{bmatrix} \begin{bmatrix} f_{0x}^1 \\ f_{0y}^1 \\ f_{0z}^1 \\ g \cos(\theta) \\ g \sin(\theta) \\ g \\ f_{0x}^2 \\ f_{0y}^2 \\ f_{0z}^2 \\ \vdots \\ f_{0x}^n \\ f_{0y}^n \\ f_{0z}^n \end{bmatrix} = \begin{bmatrix} f_x \\ f_y \\ f_z \end{bmatrix} \quad (4.13)$$

which is defined as

$$\mathbf{M}_{(3n \times 6)} \cdot \mathbf{p}_{(6 \times 1)} = \mathbf{f}_{(3n \times 1)}$$

Due to the full column rank of  $\mathbf{M}$ , we can apply Moore-Penrose pseudoinverse.

Then,

$$\begin{aligned} \mathbf{p} &= \mathbf{M}^\dagger \cdot \mathbf{f} \\ &= (\mathbf{M}^\top \mathbf{M})^{-1} \mathbf{M}^\top \cdot \mathbf{f} \end{aligned}$$

So far, the load gravity  ${}^0\mathbf{g}$  and the initial forces  $[f_{0x} \ f_{0y} \ f_{0z}]$  are obtained. Then,

Substitute the initial forces  $[f_{0x} \ f_{0y} \ f_{0z}]$  into Equation 4.6, then

$$\begin{aligned} \tau_{0x} &= k_1 + (f_{0z} \cdot y + f_{0y} \cdot z) \\ \tau_{0y} &= k_2 + (f_{0x} \cdot z + f_{0z} \cdot x) \\ \tau_{0z} &= k_3 + (f_{0y} \cdot x + f_{0x} \cdot y) \end{aligned} \tag{4.14}$$

Therefore,  $[k_1 \ k_2 \ k_3]$  are decoupled and the initial torque values  $[\tau_{0x} \ \tau_{0y} \ \tau_{0z}]$  are obtained. Last, Substitute the load gravity  ${}^0\mathbf{g}$  into Equation 4.2 and Equation 4.8, then

$$\begin{aligned} {}^S\mathbf{f}_g &= {}^S\mathbf{R} \cdot {}^6\mathbf{R} \cdot {}^0\mathbf{g} \\ {}^S\boldsymbol{\tau}_g &= \mathbf{r} \times {}^S\mathbf{f}_g \end{aligned} \tag{4.15}$$

Finally, by gravity compensation method, the initial value  $[f_{0x} \ f_{0y} \ f_{0z} \ \tau_{0x} \ \tau_{0y} \ \tau_{0z}]$  and the load gravity  $[f_{gx} \ f_{gy} \ f_{gz} \ \tau_{gx} \ \tau_{gy} \ \tau_{gz}]$  are all evaluated. Besides, the weight of the end effector  $g$  and the installation angle  $\theta$  including assembly error are also obtained.

In conclusion, with the force vector  ${}^S\mathbf{f}$  and the torque vector  ${}^S\boldsymbol{\tau}$  received from F/T sensor, the centroid position of the end effector  $\mathbf{r}$  and the coupled vector  $\mathbf{k}$  are obtained first. Then the initial values  ${}^S\mathbf{f}_0$ ,  ${}^S\boldsymbol{\tau}_0$  are calculated off-line, and subsequently the gravity load  ${}^S\mathbf{f}_0$ ,  ${}^S\boldsymbol{\tau}_0$  are evaluated on-line.

There is an further discussion about the installation angle  $\theta$  including assembly error. Undoubtedly, we can derive it from Equation 4.13as

$$\theta = \cos^{-1} \left( \frac{g \cos(\theta)}{g} \right) \text{ or } \sin^{-1} \left( \frac{g \sin(\theta)}{g} \right) \quad (4.16)$$

In theory, by either the arccos function or arcsin function, we can derive the same value. However, we estimate  $[g \cos(\theta), g \sin(\theta), g, f_{0x}, f_{0y}, f_{0z}]$  by using the least square solution which produce a approximated answer rather than the correct answer. A subtle bias caused by the least square solution will be enlarged through the arc function. Thankfully, we originally designed an adapter to connect the robot arm and F/T sensor, and the installation angle is exactly zero degrees. Therefore, here we only need to concern about the subtle bias result from assembly errors.

Here we take the same bias and compare arccos to arcsin. Obviously, if we

Table 4.1: Comparison of arc-functions

bias $n$ (rad)	$\sin^{-1}(n)$ (degree)	$\cos^{-1}(1 - n)$ (degree)
0	0	0
0.001	0.057	2.56
0.01	0.57	8.11
0.1	5.7	25.84

separately give the same bias ( 0.1 rad) into the arccos and arcsin function, the arccos function will enlarge the bias significantly larger than the arcsin function. Hence we should use

$$\theta = \sin^{-1} \left( \frac{g \sin(\theta)}{g} \right) \quad (4.17)$$

Notably, as a result of the zero installation angle we initially designed from Table 4.1, we could infer using the arcsin function. In contrast, if the installation angle is not zero, the above assumption will be invalid.

Ultimately, we have successfully dissected the actual value of the F/T sensor into the initial value of the F/T sensor and the gravity of the end effector.

### External Force Evaluation

After obtaining the initial value  $[f_{0x} \ f_{0y} \ f_{0z} \ \tau_{0x} \ \tau_{0y} \ \tau_{0z}]$  and the load gravity  $[f_{gx} \ f_{gy} \ f_{gz} \ \tau_{gx} \ \tau_{gy} \ \tau_{gz}]$ , the external force can be evaluated.

External Force = Actual Value – Initial value – Gravity Load

$${}^S\mathbf{f}_e = {}^S\mathbf{f} - {}^S\mathbf{f}_0 - {}^S\mathbf{f}_g \quad (4.18)$$

$${}^S\boldsymbol{\tau}_e = {}^S\boldsymbol{\tau} - {}^S\boldsymbol{\tau}_0 - {}^S\boldsymbol{\tau}_g$$

where  ${}^S\mathbf{f}_e$  is  $[f_{ex} f_{ey} f_{ez}]$ ,  ${}^S\boldsymbol{\tau}_e$  is  $[\tau_{ex} \tau_{ey} \tau_{ez}]$ , and

$$\begin{aligned}
 f_{ex} &= f_x - f_{0x} + g \cos(\theta)r_{13} + g \sin(\theta)r_{23} \\
 f_{ey} &= f_y - f_{0y} - g \sin(\theta)r_{13} + g \cos(\theta)r_{23} \\
 f_{ez} &= f_z - f_{0z} + gr_{33} \\
 \tau_{ex} &= f_x - \tau_{0x} - (g_z \cdot y - g_y \cdot z) \\
 \tau_{ey} &= f_y - \tau_{0y} - (g_x \cdot z - g_z \cdot x) \\
 \tau_{ez} &= f_z - \tau_{0z} - (g_y \cdot x - g_x \cdot y)
 \end{aligned} \tag{4.19}$$

### 4.3 Dragging Mode

In the hope that dentist could drag our system to an infected tooth by holding the end effector, in this section admittance control based on F/T sensor is presented followed by selection of admittance control model, robot command decision, and implementation in discrete time.

#### Admittance Control based on F/T sensor

Admittance control makes the robot move like a spring-mass-damper system. Forces and torques can be mapped into the movements such as position or velocity. Most importantly, admittance control enables a robot arm to cooperate with humans in a safe work environment [35]. Since Meca500 is an industrial robot arm without admittance control, we subsequently combine the robot arm with the F/T sensor to adopt admittance control. With force and torque feedback, the F/T sensor makes

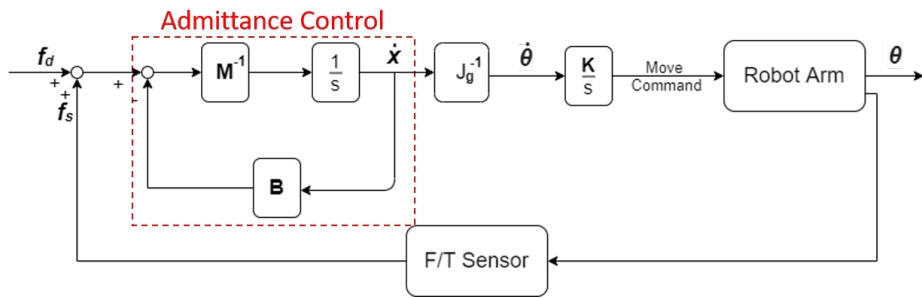


Figure 4.2: Control scheme.  $f_d$  denotes the desired forces and torques vector.  $f_s$  denotes the real value measured by F/T sensor.  $\dot{x}$ ,  $[\dot{x}, \dot{y}, \dot{z}, \dot{\theta}_x, \dot{\theta}_y, \dot{\theta}_z]$ , denotes the velocity of end effector.  $J_g$  denotes the geometric Jacobian matrix.  $\dot{\theta}$ ,  $[\dot{\theta}_1, \dot{\theta}_2, \dot{\theta}_3, \dot{\theta}_4, \dot{\theta}_5, \dot{\theta}_6]$ , denotes the joints' angular velocities.  $\theta$ ,  $[\theta_1, \theta_2, \theta_3, \theta_4, \theta_5, \theta_6]$ , denotes the joints' angles.  $M$  is an inertial diagonal matrix,  $\text{diag}(m_1, m_2, \dots, m_6)$ , and  $B$  is a damping diagonal matrix,  $\text{diag}(b_1, b_2, \dots, b_6)$ .  $K$  is a constant gain diagonal matrix,  $\text{diag}(k, k, k, k, k, k)$ .

Meca500 be like a collaborative robot arm. a control scheme is proposed and depicted in Figure 4.2. It's worth noting that in this approach, the admittance control function is triggered by the end effector mounted on the F/T sensor instead of detecting each wrist torque of the robot arm.

A standard equation of admittance control is represented as Equation 4.20.

The values we obtain from the F/T sensor are  $[f_x, f_y, f_z, \tau_x, \tau_y, \tau_z]$ , whose forces  $[f_x, f_y, f_z]$  are related to the translations  $[x, y, z]$  and torques  $[\tau_x, \tau_y, \tau_z]$  are related to the axis angle  $[\theta_x, \theta_y, \theta_z]$ . Take the first element for example,

$$\begin{aligned} x(s) &= \frac{1}{m_1 s^2 + b_1 s + k_1} \cdot f_x(s) \\ &:= A(s) \cdot f_x(s) = a(t) \otimes f_x(t) \end{aligned} \quad (4.20)$$

Therefore,

$$\begin{bmatrix} x(s) \\ y(s) \\ z(s) \\ \theta_x(s) \\ \theta_y(s) \\ \theta_z(s) \end{bmatrix} = \begin{bmatrix} \frac{1}{m_1 s^2 + b_1 s + k_1} & 0 & \dots & 0 \\ 0 & \frac{1}{m_2 s^2 + b_2 s + k_2} & & \vdots \\ \vdots & & \ddots & 0 \\ 0 & \dots & 0 & \frac{1}{m_6 s^2 + b_6 s + k_6} \end{bmatrix} \begin{bmatrix} f_x(s) \\ f_y(s) \\ f_z(s) \\ \tau_x(s) \\ \tau_y(s) \\ \tau_z(s) \end{bmatrix} \quad (4.21)$$

where  $[m_1, m_2, \dots, m_6], [b_1, b_2, \dots, b_6], [k_1, k_2, \dots, k_6]$  are inertial, damping and spring parameters of admittance control,

### Selection of Admittance Control Model

In our proposed approach,  $\mathbf{K}$  related to spring stiffness is omitted, considering that it's not necessary to bounce such as a spring. Therefore, our system should behave like a mass-damper system. The input is the value measured by F/T sensor and the output is the velocity of end effector shown as

$$\begin{bmatrix} \dot{x}(s) \\ \dot{y}(s) \\ \dot{z}(s) \\ \dot{\theta}_x(s) \\ \dot{\theta}_y(s) \\ \dot{\theta}_z(s) \end{bmatrix} = \begin{bmatrix} 0 & 0 & \dots & 0 \\ \frac{1}{m_1 s + b_1} & 0 & \dots & 0 \\ 0 & \frac{1}{m_2 s + b_2} & \ddots & \vdots \\ \vdots & \ddots & \ddots & 0 \\ 0 & \dots & 0 & \frac{1}{m_6 s + b_6} \end{bmatrix} \begin{bmatrix} f_x(s) \\ f_y(s) \\ f_z(s) \\ \tau_x(s) \\ \tau_y(s) \\ \tau_z(s) \end{bmatrix} \quad (4.22)$$

### Robot Command Decision

After determining our admittance control model, we should select a corresponding command to move the robot. However, there are many commands of moving the robot arm, as shown in Table 4.2.

Position commands is better than velocity commands because Meca500 has a default time-out value to ensure its safety. Even though we could set this value from 0.001 to 1 seconds via the command "SetVelTimeout", Meca500 is still restricted to move with this value. For instance, the value of time-out is set 0.1 sec. While the robot receives a command, the robot move for 0.1 sec then immediately stops. Therefore, it's not easy to control via velocity command due to this default

Table 4.2: Moving commands of Meca500

Types	Commands	Input parameters
Position	MoveJoints	$\theta_1, \theta_2, \theta_3, \theta_4, \theta_5, \theta_6$
	MovePose	$x, y, z, \alpha, \beta, \gamma$
Velocity	MoveJointsVel	$\dot{\theta}_1, \dot{\theta}_2, \dot{\theta}_3, \dot{\theta}_4, \dot{\theta}_5, \dot{\theta}_6$
	MoveLinVelTRF	$\dot{x}, \dot{y}, \dot{z}, \dot{\theta}_x, \dot{\theta}_y, \dot{\theta}_z$

property.

There are two suitable ways to command robot - MovePose and MoveJoints. Implementation of MovePose  $(x, y, z, \alpha, \beta, \gamma)$  is easier than MoveJoints because MovePose is considered in tool-tip frame. That means the robot arm will move  $(x, y, z, \alpha, \beta, \gamma)$  based on the current tool-tip frame.  $(x, y, z)$  can be obtained by multiplying an integrator with  $(\dot{x}, \dot{y}, \dot{z})$ . As for  $(\alpha, \beta, \gamma)$ ,  $(\dot{\alpha}, \dot{\beta}, \dot{\gamma})$  can be obtained by multiplying the inverse matrix of analytical Jacobian which was mentioned in Equation 3.15 with  $\dot{\theta}_x, \dot{\theta}_y, \dot{\theta}_z$ , and then  $(\alpha, \beta, \gamma)$  can be obtained by multiplying an integrator with  $(\dot{\alpha}, \dot{\beta}, \dot{\gamma})$ .

However, considering that the singularity problem is an imperative subject in robotics, we intend to use MoveJoints to set the axes' angles directly. Despite that it's easier to implement admittance control via other commands, the system would touch the singularity point at any time. It undoubtedly exposes patients to danger because of the uncertainty of the system. In our case, we could detect whether it is a singularity or not before commanding the robot. Therefore, position command - MoveJoints and velocity command - MoveJointsVel is our option.

Finally, we designate MoveJoints  $\theta_1, \theta_2, \theta_3, \theta_4, \theta_5, \theta_6$  as our main command. Thanks to the property of Jacobian matrix shown in Equation 3.13, we can transform  $\dot{x}$  into  $\dot{\theta}$ . Then we multiply it an integrator  $\frac{1}{s}$  to obtain  $\theta$ . Note that, because admittance control is based on frame  $\{H\}$ , we should use  ${}^H J_g$  in Equation 3.13 rather than  ${}^0 J_g$  in Equation 3.7.

### Implementation in Discrete Time

To implement it in digital control, the bilinear transformation, also known as Tustin method, is used to control it in discrete time.

$$\begin{aligned} \mathcal{L} \left\{ \frac{v_i(t)}{f_i(t)} \right\} &= \frac{V_i(s)}{F_i(s)} = \frac{1}{m_i s + b_i} \\ \Rightarrow \mathcal{Z} \left\{ \frac{v_i(k)}{f_i(k)} \right\} &= \frac{V_i(z)}{F_i(z)} = \frac{t_s \cdot (1 + z^{-1})}{(t_s \cdot b_i + 2m_i) + (t_s \cdot b_i - 2m_i) \cdot z^{-1}} \end{aligned} \quad (4.23)$$

and

$$\begin{aligned} \mathcal{L} \left\{ \frac{\theta_i(t)}{w_i(t)} \right\} &= \frac{\theta_i(s)}{W_i(s)} = \frac{k}{s} \\ \Rightarrow \mathcal{Z} \left\{ \frac{\theta_i(k)}{w_i(k)} \right\} &= \frac{\theta_i(z)}{W_i(z)} = \frac{t_s \cdot k}{2} \frac{1 + z^{-1}}{1 - z^{-1}} \end{aligned} \quad (4.24)$$

where  $i = 1, 2, \dots, n$ .  $(v_1, v_2, \dots, v_6)$  denotes  $(\dot{x}, \dot{y}, \dot{z}, \dot{\theta}_x, \dot{\theta}_y, \dot{\theta}_z)$ .  $(f_1, f_2, \dots, f_6)$  denotes  $(f_x, f_y, f_z, \tau_x, \tau_y, \tau_z)$ .  $(w_1, w_2, \dots, w_6)$  denotes  $(\dot{\theta}_1, \dot{\theta}_2, \dots, \dot{\theta}_6)$ .  $k$  represents the constant gain.  $t_s = 0.002$  represents the sampling time.  $(m_1, m_2, \dots, m_6)$  and  $(b_1, b_2, \dots, b_6)$  represent inertial and damping parameters of admittance control.

Therefore, the crucial equations are derived as

$$\begin{aligned} v_i[k+1] &= \frac{t_s}{t_s \cdot b_i + 2m_i} \cdot (f_i[k+1] + f_i[k]) - \frac{t_s \cdot b_i - 2m_i}{t_s \cdot b_i + 2m_i} \cdot v_i[k] \\ \theta_i[k+1] &= \theta_i[k] + \frac{t_s \cdot k}{2} (w_i[k+1] + w_i[k]) \end{aligned} \quad (4.25)$$

## 4.4 Self-Alignment Mode

This section aims to adjust the surgical path in real-time. This approach is one of the main contributions in this thesis. A critical technical solution to coordinate transformation of F/T sensor is presented followed by motion planning based on admittance control.

### Coordinate Transformation of F/T sensor

In "Self-Alignment Mode," DentiBot amends the inserting direction by itself to lower the contact resistance. DentiBot should rotate and move the endodontic file related to the tool-tip frame. Nevertheless, the F/T sensor has its own reference coordinates initially. The F/T sensor originally recognizes its coordinate rather than the tool-tip frame. Namely, the F/T sensor receives unmatched data when the tool contacts an obstacle due to the wrong reference frame [36]. Therefore, it is essential to change the reference coordinate of F/T sensor from its original coordinate, frame{S}, to tool-tip coordinate, frame{H}. We analyze it from two perspectives - reference frame changing and measurement point changing.

#### Reference Frame Changing

Figure 4.3 illustrates a force and a torque applied at point p. The force and torque related to {S} and {H} are compared and described as

$$\begin{bmatrix} {}^H \boldsymbol{f}_p \\ {}^H \boldsymbol{\tau}_p \end{bmatrix} = \begin{bmatrix} {}^H \mathbf{R} & \mathbf{0} \\ \mathbf{0} & {}^H \mathbf{R} \end{bmatrix} \begin{bmatrix} {}^S \boldsymbol{f}_p \\ {}^S \boldsymbol{\tau}_p \end{bmatrix} \quad (4.26)$$

where  $\mathbf{f}_p$  and  $\boldsymbol{\tau}_p$  denote the force and the torque applied at point p respectively.

${}^S_R$  is the rotation matrix from frame  $\{S\}$  to  $\{H\}$ .

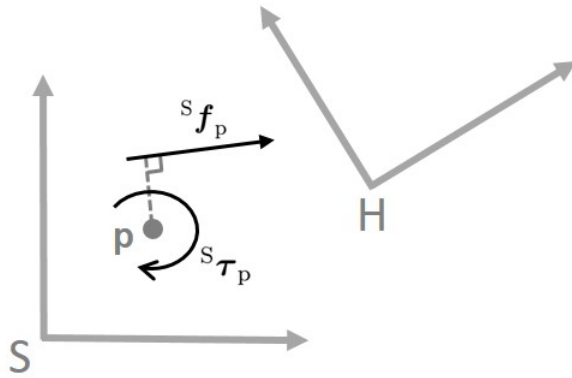


Figure 4.3: Illustration of changing reference frame from  $\{S\}$  to  $\{H\}$ .  ${}^S \mathbf{f}_p$  and  ${}^S \boldsymbol{\tau}_p$  respectively denote a force vector and a torque vector applied at point p and observed from  $\{S\}$ .

### Measurement Point Changing

On the other hand, in Figure 4.4 the relationship of a force and a torque observed at the same frame but at different points is derived as

$$\begin{aligned} {}^H \mathbf{f}_q &= {}^H \mathbf{f}_p \\ {}^H \boldsymbol{\tau}_q &= r_q \cdot {}^H \mathbf{f}_q \\ &= r_p \cdot {}^H \mathbf{f}_p + \mathbf{u} \times {}^H \mathbf{f}_p \\ &= \boldsymbol{\tau}_p + \mathbf{u} \times \mathbf{f}_p \end{aligned} \tag{4.27}$$

where  $\mathbf{f}_p$  and  $\mathbf{f}_q$  are respectively represent the same force measured at point p and q.  $\boldsymbol{\tau}_p$  and  $\boldsymbol{\tau}_q$  are respectively represent the same torque measured at point p and q.

$\mathbf{u}$  denotes the vector from q to p.

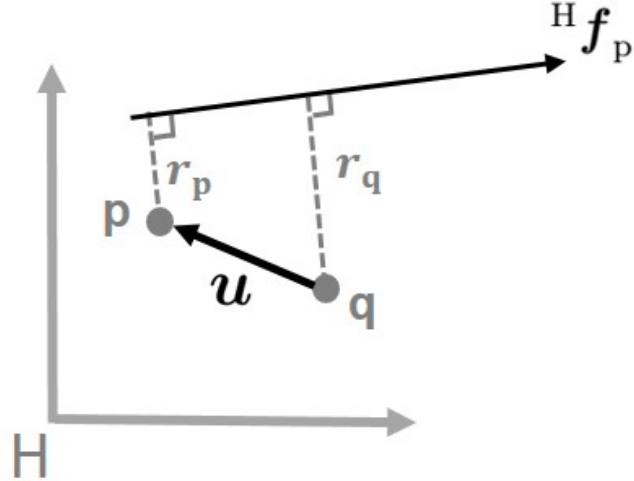


Figure 4.4: Illustration of changing measurement point from point p to point q.  $\mathbf{f}$  denote a force vector applied at frame  $\{\mathbf{H}\}$  and observed from point p and q.  $r_p, r_q$  are distances between point p, q and their projections on  $\mathbf{f}$ .

Assume

$$\mathbf{u} = \begin{bmatrix} u_1 \\ u_2 \\ u_3 \end{bmatrix}$$

Then

$$\mathbf{u} \times \mathbf{f}_p = \begin{bmatrix} 0 & -u_3 & u_2 \\ u_3 & 0 & -u_1 \\ -u_2 & u_1 & 0 \end{bmatrix} \begin{bmatrix} f_1 \\ f_2 \\ f_3 \end{bmatrix} \quad (4.28)$$

Therefore,

$$\begin{bmatrix} \mathbf{f}_q \\ \boldsymbol{\tau}_q \end{bmatrix}_{\{H\}} = \begin{bmatrix} \mathbf{I}_{3 \times 3} & \mathbf{0}_{3 \times 3} \\ 0 & -u_3 & u_2 \\ u_3 & 0 & -u_1 & \mathbf{I}_{3 \times 3} \\ -u_2 & u_1 & 0 \end{bmatrix} \begin{bmatrix} \mathbf{f}_p \\ \boldsymbol{\tau}_p \end{bmatrix}_{\{H\}} \quad (4.29)$$

Finally, reference frame changing and measurement point changing are combined and shown in Equation 4.30. F/T sensor now can change the reference frame from its original frame  $\{S\}$  to the tool-tip frame  $\{H\}$ .

$$\begin{bmatrix} \mathbf{f}_q \\ \boldsymbol{\tau}_q \end{bmatrix}_{\{H\}} = \begin{bmatrix} \mathbf{I}_{3 \times 3} & \mathbf{0}_{3 \times 3} \\ 0 & -u_3 & u_2 \\ u_3 & 0 & -u_1 & \mathbf{I}_{3 \times 3} \\ -u_2 & u_1 & 0 \end{bmatrix} \begin{bmatrix} {}^H_S \mathbf{R} & \mathbf{0} \\ \mathbf{0} & {}^H_S \mathbf{R} \end{bmatrix} \begin{bmatrix} \mathbf{f}_p \\ \boldsymbol{\tau}_p \end{bmatrix}_{\{S\}} \quad (4.30)$$

To implement it in the DentiBot, the corresponding points and vecotors are illustrated in Figure 4.5. It is worth noting that the point p is the origin on the frame  $\{S\}$ , the point q is the origin on the frame  $\{H\}$ , and  $\mathbf{u}$  is the vector which is the origin of frame  $\{H\}$  observed from the frame  $\{S\}$ . Therefore,

$$\mathbf{u} = {}^S \mathbf{p}_H = {}^S \mathbf{p}_6 + {}^6 \mathbf{p}_H \quad (4.31)$$

where  ${}^i \mathbf{p}_j$  ( $i = 6, S$  and  $j = 6, H$ ) denotes the origin of frame  $\{j\}$  observed from frame  $\{i\}$ .  ${}^6 \mathbf{p}_H$  is obtained by the TCP method mentioned in Section 3.4.  ${}^S \mathbf{p}_6$  is a known variable obtained by the mechanism design.

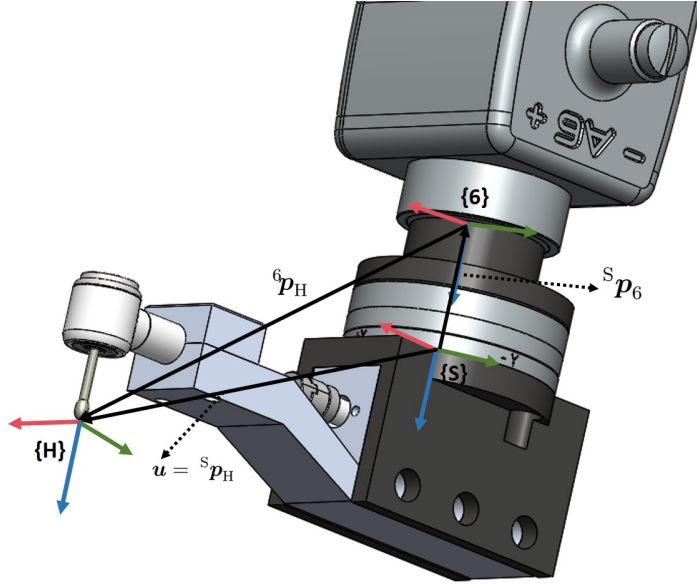


Figure 4.5: Implementation of Sensor compensation in the DentiBot.

## Motion Planning Based on Admittance Control

Here we plan a series of motions to simulate the cleaning procedure of the root canal treatment. Endodontist uses their professional experience to determine how many force to apply and when to reverse the file to release the torque caused by the contact force. Because the root canal resembles a cone. The profundity of the file is larger, then the resultant force composed of contact forces is more significant. Namely, the endodontist will apply more and more pressure in the insertion direction during the surgery. To simulate this series of motions, we could directly command the robot arm to move with the series of actions. However, commanding the robot arm is a dilemma because we have already use admittance control which also commands the robot arm to move. Therefore, to solve the

conflict, we continue to utilize admittance control and propose a method based on admittance control to simulate the series of motions. Because we know the tool-tip frame from section 3.4, we can regulate  $f_d$  to make the robot move. That means if we want to insert along with the tool direction, we could set  $[0 \ 0 \ f_z \ 0 \ 0 \ 0]$ . While  $f_z$  is larger, the robot moves faster.

## 4.5 Parameter Selection

Because our system is similar to a mass-damper system, we focus on the performance of the velocity  $\dot{x}$ . The input is the sum of the desired force and sensor values. Therefore, the system could be considered as

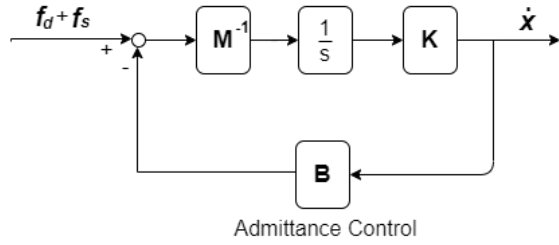


Figure 4.6: Admittance Control.  $f_d$  denotes the desired forces and torques vector.  $f_s$  denotes the real value measured by F/T sensor.  $\dot{x}, [\dot{x}, \dot{y}, \dot{z}, \dot{\theta}_x, \dot{\theta}_y, \dot{\theta}_z]$ , denotes the velocity of end effector.  $M$  is an inertial diagonal matrix,  $\text{diag}(m_1, m_2, \dots, m_6)$ , and  $B$  is a damping diagonal matrix,  $\text{diag}(b_1, b_2, \dots, b_6)$ .  $K$  is a constant gain diagonal matrix,  $\text{diag}(k, k, k, k, k, k)$ .

It is a first-order control system and its step response is

$$\begin{aligned}\mathcal{L}^{-1} \left[ \frac{1}{s} \cdot \frac{k}{m_i s + b_i} \right] &= \mathcal{L}^{-1} \left[ \frac{k}{b_i} \left( \frac{1}{s} - \frac{1}{s + \frac{b_i}{m_i}} \right) \right] \\ &= \frac{k}{b_i} \left( 1 - e^{-\frac{b_i}{m_i} t} \right)\end{aligned}\quad (4.32)$$

where  $i = 1$  to  $n$ .

From the above derivation, we can know

$$\begin{aligned}\text{time constant } \tau_i &= \frac{m_i}{b_i} \\ \text{gain} &= \frac{k}{b_i}\end{aligned}\quad (4.33)$$

Hence, the transient response can be derived as

$$\begin{aligned}\text{Rise time} &= 2.3\tau_i = \frac{2.3m_i}{b_i} \\ \text{Settling time} &= 4\tau_i = \frac{4m_i}{b_i}\end{aligned}\quad (4.34)$$

In theory, when  $\tau_i$  is larger, the pole is farther from the origin in s domain, the system is more stable. Besides, when  $\tau_i$  is larger, the response speed is faster. Furthermore, when the gain  $\frac{k}{b_i}$  is larger, the robot arm moves more. Therefore, we coarse-tune parameter  $k$  to adjust the whole gain of the system and determine the mode of the system is "Dragging Mode" or "Self-Alignment Mode". Last but not least, we fine-tune diagonal parameters of  $b_i$  separately because the inertial and spring properties of each axis are discrepant.

In practice, we implement it in discrete time. From Equation 4.23, we can further derive the final value in discrete time shown as

$$\text{gain} = \lim_{z \rightarrow 1} (z - 1) \cdot \frac{t_s \cdot k(z + 1)}{(t_s \cdot b_i + 2m_i)z + t_s \cdot b_i - 2m_i} \cdot \frac{1}{\frac{2}{t_s} \frac{z-1}{z+1}} = \frac{k \cdot t_s}{b_i} \quad (4.35)$$

Compared to the gain in continuous time, the sampling time in discrete time also affect the gain. Because the sampling time we set is 0.002s, we set ( $m_i : b_i = 1 : 500$ ) to make ( $\tau_i = \frac{m_i}{b_i} = 0.002$ ), then the system will rise up to 98% after 0.004 second. Further, we can alter  $k$  to easily regulate the gain. It is worth noting that the rotation along with Z-axis driven by the robot arm should be deactivated in "Self-Alignment Mode" because the file rotation is driven by the motor. If the rotation along with z-axis is on duty and the file is drilling, the robot arm would rotate along with Z-axis in opposite direction. Hence,  $b_6$  is set a infinite value to deactivate the rotation along with Z-axis. Detailed parameters setting of admittance control with "Dragging Mode" and "Self-Alignment Mode" are shown in Table 4.3.

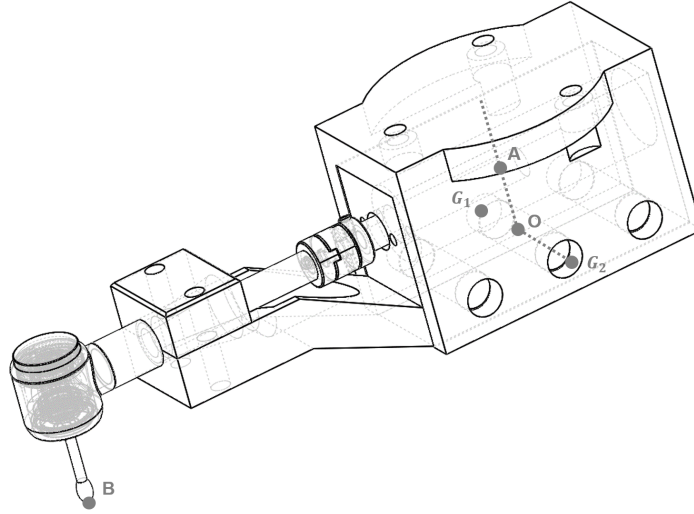


Figure 4.7: Reference point A in Dragging Mode. Reference point B and holding points  $G_1, G_2$  in Self-Alignment Mode.

Table 4.3: Parameters setting of Admittance control.

Parameter	Dragging Mode	Self-Alignment Mode
k	1500	500
$b_1$	80	80
$b_2$	80	80
$b_3$	80	80
$b_4$	160	80
$b_5$	160	80
$b_6$	160	$\infty$
$m_1$	0.08	0.08
$m_2$	0.08	0.08
$m_3$	0.08	0.08
$m_4$	0.16	0.08
$m_5$	0.16	0.08
$m_6$	0.16	$\infty$

---


$$\mathbf{K} = \text{diag}(k, k, k, k, k, k), \quad \mathbf{B} = \text{diag}(b_1, b_2, b_3, b_4, b_5, b_6)$$


---


$$\mathbf{M} = \text{diag}(m_1, m_2, m_3, m_4, m_5, m_6)$$


---

Note that we change the different sensor frames in "Dragging Mode" and "Self-Alignment Mode". As shown in Figure 4.7, Point A and B are two origins of the sensor frame. In "Dragging Mode", we transform the sensor frame to the point A, and the operator can hold the point  $G_1$  and  $G_2$  to move the entire handpiece. On the other hand, in "Self-Alignment Mode" we set the point B as the new sensor frame because we focus on forces and torques the file bears. Due to different level arms, the forces we apply in each axis will be different. There are same level arms ( $\overline{AO}$  and  $\overline{OG}_2$  both are 13.2 mm) if we set the point A as the sensor frame and grasp  $G_1$  and  $G_2$  to move the entire handpiec. Therefore, to provide users a good experience, we should regulate parameters of B in "Dragging mode" with suitable values. With these values, the users can smoothly move the robot arm to the desired position and orientation. We set the first three variables relative to the linear velocity as the same values. Besides, We set the last three variables relative to the angular velocity as the other same values.

# **Chapter 5**

## **File Rotation and Feedrate Control**

The proposed approaches for protecting an endodontic file from fracturing is proposed in this chapter. A brief problem definition is addressed followed by two proposed method – Inverse rotation control and file feedrate control. Finally, the flowchart of the algorithm for autonomous endodontic treatment is proposed.

### **5.1 Problem Definition and Proposed Method**

In this section, problem definition – Instrument fracture is discussed followed by a brief description of proposed methods. Furthermore, file property is assessed and the methods for estimating torque are interpreted.

#### **Problem Definition**

Instrument fracture is a potential crisis for endodontic treatment. If a dentist improperly operates an endodontic file, it will increase the possibility of instrument fracture. Most largely, the instrument fracture will happen while a file is inserted into the one-third place far from the root apex. It is barely possible to take out in a small root canal. Removal of broken files is technically tricky, so it is critical to reducing the probability of the instrument fracture.

There is a technical solution to detect a status of a file. When a file suffers a force, it will lead to the crystalline phase transformation. However, it can only be observed from a microscope. It is impracticable to usually monitor it during the surgery. Previous literature shows there are two main causes of fractured files are torsional fracture and flexural fatigue, which account for 55.7% and 44.3% separately[12]. Therefore, we can reduce the torque a file bears to prevent the instrument fracture.

### File Property

To protect the endodontic file from fracturing, it is imperative to be familiar with its physical property and its correct operations. the physical properties of an endodontic file are assessed. A file is made of alloys of Nickel and Titanium, which is a superelastic material. The Ni-Ti file has significantly more elastic and incorruptible properties. This feature allows it to bend when inserted into a curve root canal and thereby reduces the possibility of stuck.

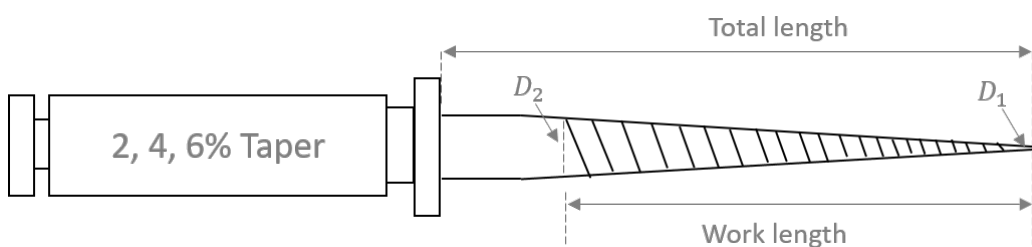


Figure 5.1: The illustration of an endodontic file

In Figure 5.1, an endodontic file is illustrated. There are four types of total

length - 21, 25, 28, and 31 mm. They all have the same work length - 16 mm. Each file has their own number such as #15, #20, #25, … , #40 shown as Figure 5.2, which represent the diameter of files. Take a #15 file with 2% taper for example, the diameter of the tool-tip  $D_1$  is

$$15/100 = 0.15 \text{ (mm)}$$

and the diameter at the end of the work length  $D_2$  is

$$0.15 + 16 \cdot 6\% = 1.11 \text{ (mm)}$$



Figure 5.2: Endodontic files with different diameters

### Proposed Method

In order to protect an endodontic file from fracturing, we need to reduce the file torque. The easiest and most effective way to solve this issue would be monitoring

the torque which the file is enduring. Therefore, a torque monitoring system is implemented on DentiBot. An increase in the file torque is indicative of the contact resistance of the file. Two approaches based on torque monitoring are proposed to protect endodontic files. One is inverse rotation control discussed in section 5.2 and the other is file feedrate control discussed in section 5.3, they are both efficient ways to release the file torque. Once the torque of the file is in excess of a threshold, the file will inversely rotate or decline the feedrate to release torque.

### **How to measure the file torque**

There are two approaches to measure the file torque. One is detecting the current of motor which drives the file rotation to estimate the file torque. The other is directly obtained from the F/T sensor after changing the reference frame to the tool-tip frame.

Here we delves into the first method - detecting the current of motor to estimate the file torque. A motor can be modelled as an RL circuit. In this way, we can get the following formula

$$V = R \cdot I + L \cdot \frac{dI}{dt} + \varepsilon \quad (5.1)$$

where  $V$  represents the input voltage,  $I$  represents the input current, and  $\varepsilon$  represents the back EMF produced by the motor motion.

Since the value of the inductance of DC motor is small, we ignore the inductance term  $L$ . After transposition, we can get the following relation between the

current and the back EMF.

$$I = \frac{I - \varepsilon}{R} \quad (5.2)$$

The back EMF produced by the motor is dependent upon the motor constant  $K$ , shown as the following equation.

$$\varepsilon = K \cdot \frac{d\theta(t)}{dt} = K \cdot \omega(t) \quad (5.3)$$

When the file encounters resistance during the drilling procedure, the rotating speed of the motor would slow down. With the Equation 5.2 and 5.3 we can infer that the back EMF would decrease, and the current would increase. Also, we have the relation between the current and torque

$$T_m = k_m \cdot I \quad (5.4)$$

where  $k_m$  represent the torque constant of a motor.

The maximum torque a root canal file can bear is 6.20 Ncm (62.0 mNm) [37]. Therefore, we can derive the following inequality.

$$T_m \cdot GR < 62 \text{ (mNm)} \quad (5.5)$$

where GR is gear ratio of gearbox mounted on a motor.

Hence, we can set a current threshold based on the following condition.

$$I_{max} < \frac{62}{GR \cdot K_m} \quad (5.6)$$

In realistic implementation, GR is 67 and  $K_m$  is 16 mNm/A

## 5.2 Inverse Rotation Control

This proposed approach is an effective way to protect endodontic file from fracturing. Also, it can remove root debris cut by file and prevent file from getting stuck in root. Once the current of the file exceeds the specific threshold, it will inversely rotate for 90 degrees to release torque and then continue drilling in the original direction. Before designing DentiBot, we have validated this function with the prototype of DentiBot shown as Figure 5.3. This prototype is a drilling system mounted on a magnetic stand. The modified handpiece, a hand-held dental electric device, with a single axis mechanism can validate the inverse rotation control.

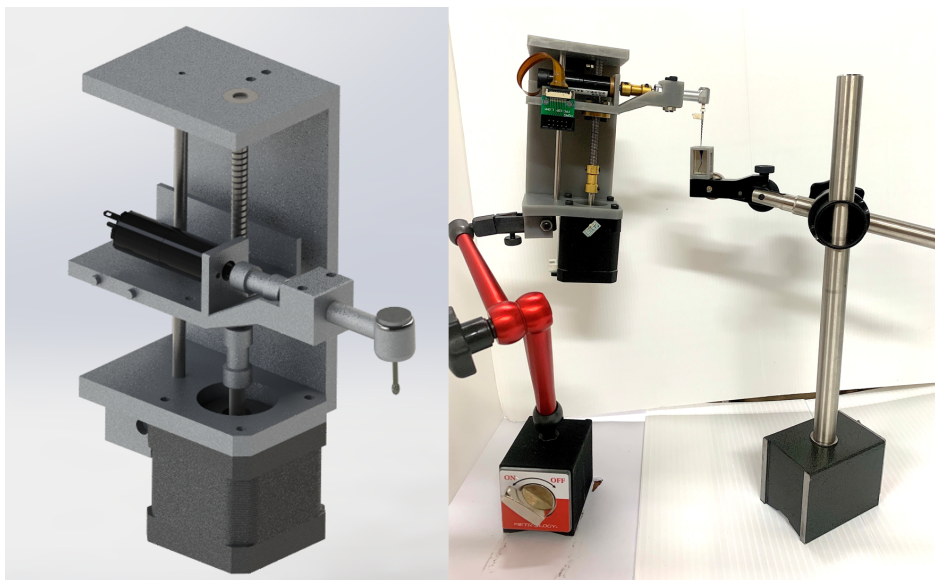


Figure 5.3: The prototype of DentiBot. A single z-axis manipulator with a modified handpiece to verify our proposed method – Inverse Rotation Control

In Figure 5.4, a motion planning is designed to perform the drilling procedure.

The root canal is divided into several sections to be cleaned. In the beginning, the robot moves to the start point and then repetitively drills one section back and forth at least ten times until the current feedback decrease under the specific threshold. If the torque exceeds the threshold, the endodontic file will inversely rotate for 90 degrees to release the torque and then drill the same section again. After one section is cleaned thoroughly, the drilling file will move to the next section. Every section will be cleaned for at least 10 rounds. If there is reverse rotation, it will be more than 10 rounds. When to finish is contingent on whether the endodontic file reaches the final section.

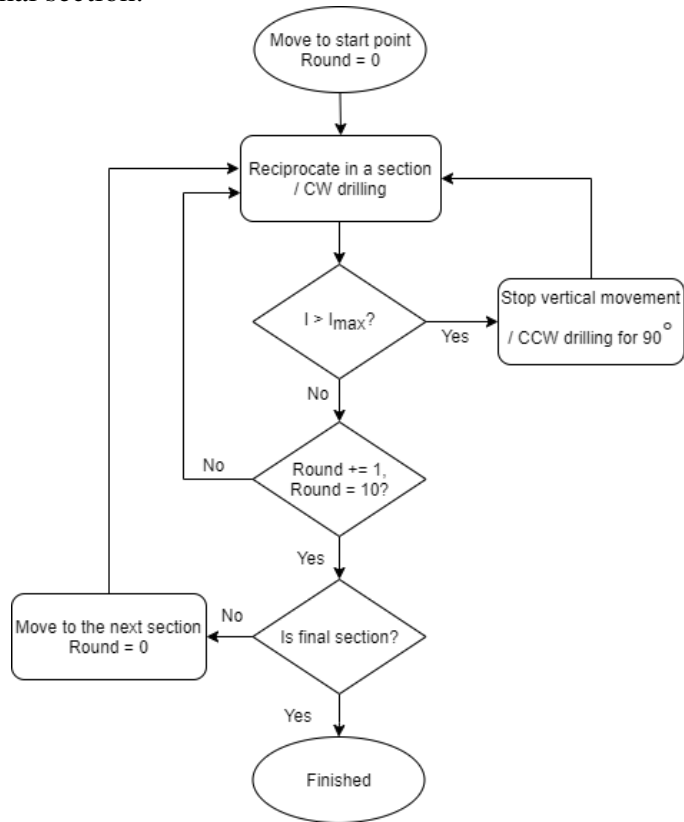


Figure 5.4: Motion planning of Inverse Rotation Control with the prototype of DentiBot.  $I_{max}$  denotes the maximum bearing current

In conclusion, by the preliminary experiment with the prototype of DentiBot, it has been proved that the inverse control rotation is an effective approach to reduce the torque. Therefore, we can detect the current to estimate the torque and inversely rotate the motor if the current exceeds the threshold current.

### 5.3 File Feedrate Control

As mentioned above, we have validated the inverse rotation control with the prototype. However, inverse rotation control is just mimicking a dentist to perform endodontic treatment. It is still time-consuming. Hence, the other method - feed control is proposed to improve this problem. Note that this method can only be valid with DentiBot instead of its prototype because admittance control will be involved. Previous literature which dedicate to a form drilling with torque control is similar to our root drilling [37]. Regulating the feedrate to control the torque is an effective way to reduce time.

$$Vf = f \cdot N$$

where  $Vf$  denotes feedrate.  $f$  denotes feed per revolution.  $N$  denotes spindle speed (rpm).

As the above equation, regulating the feed and spindle can both affect feedrate. Refer to the previous literature, we set the spindle speed a constant (60 rpm) and the feed a variable. Therefore, we regulate the feed instead of the spindle speed to determine the feedrate. A similar control scheme for our root drilling is proposed

and shown as Figure 5.3.

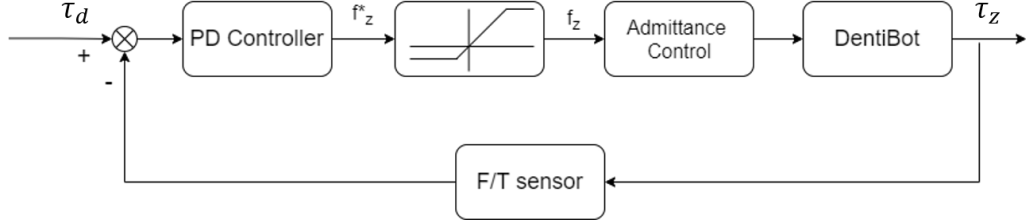


Figure 5.5: Control scheme of File Feedrate Control with DentiBot.  $\tau_d$  represents the desired torque.  $\tau_z$  represents the file torque.  $f_z$  is the third element of the input of admittance control.

The input is the desired torque  $\tau_d$  and the feedback is the file torque  $\tau_z$ .  $f_z^*$  will be determined by the difference of  $\tau_d$  and  $\tau_z$  via a PD controller. A saturation function is involved to constraint  $f_z^*$  and output  $f_z$ .

$$f_z = \text{sat}(f_z^*) = \begin{cases} -0.2 & , \text{if } f_z^* < -0.2 \\ f_z^* & , \text{if } -0.2 \leq f_z^* \leq 0.2 \\ 0.5 & , \text{if } f_z^* > 0.5 \end{cases} \quad (5.7)$$

$f_z$  is the input of admittance control and is relevant to the feed of z-axis. With the admittance control, DentiBot can move along with the tool because  $f_z$  is related to the inserting direction. In conclusion, the feedrate can be regulated by the torque. When the file torque increases, DentiBot will decrease its moving velocity to control the increase rate of file torque. It is worth noting that we combine admittance control into this approach. This feature not only provides the moving direction, but also tracks the root path and patient moving. Once the F/T sensor detects the extra value different from  $[0 \ 0 \ f_z \ 0 \ 0 \ 0]$ , DentiBot will move to the

correspond position and orientation. Moreover, because the z-orientation should be only acted by the file rotation driven by the motor, it is important to turn off z-orientation of admittance control by setting the parameter  $b_6$  of admittance control as a large value.

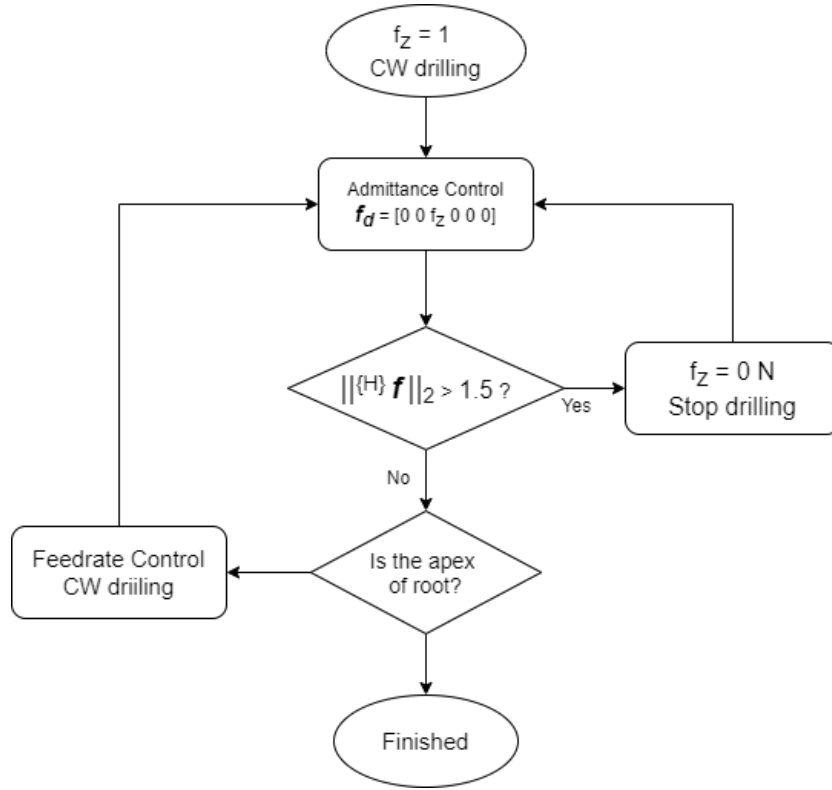


Figure 5.6: Flow chart of File Feedrate Control with DentiBot.  $\{H\} f$ ,  $[f_x, f_y, f_z, \tau_x, \tau_y, \tau_z]$ , is measured by F/T sensor related to frame  $\{H\}$ .  $f_d$  denotes the desired force.

Entire flow chart is shown in Figure 5.6. Considering the realistic condition, DentiBot judges whether patient moving happens by checking whether  $||\{H\} f||_2$  is larger than 1.5 N. File rotation will stop and  $f_z$  will be zero to stop moving when the value is more than 1.5 N, then DentiBot can keep track of the patient moving.

If not, DentiBot will continue drilling with file feedrate control until the tool-tip reaches the apex of root.

## 5.4 Automated Endodontic Treatment

After pre-clinical evaluation, we found that cleaning root only with force-guided alignment and file feedrate control is impracticable. The endodontic file is easy to get stuck in the root due to root debris. The stuck precipitates a dramatic increase of the file torque and file feedrate control can not handle the dramatic increase. The effective way to solve this problem is to rotate inverse the file. Because it is essential to withdraw to get rid of root debris cut by file. The new idea that combines for-guided alignment, inverse rotation control, and file feedrate control is proposed.

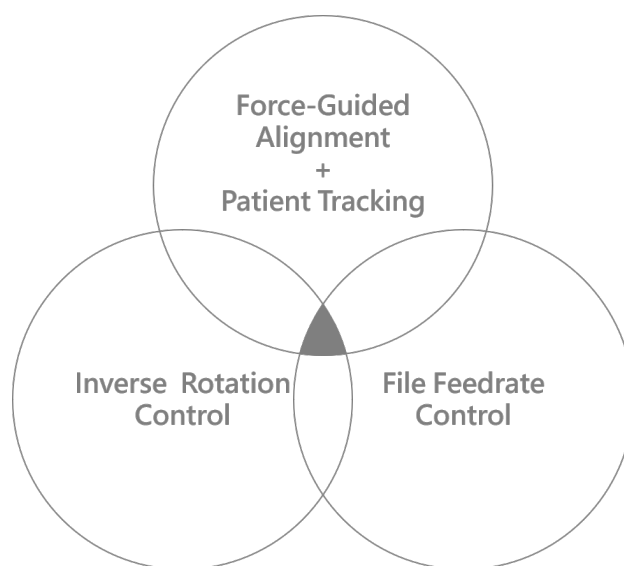


Figure 5.7: Methods of autonomous endodontic treatment

In view of this, a new algorithm for automated endodontic treatment that combines force-guided alignment, inverse rotation control, and file feedrate control is proposed as shown in Figure 5.8. Based on the flow chart of file feedrate control

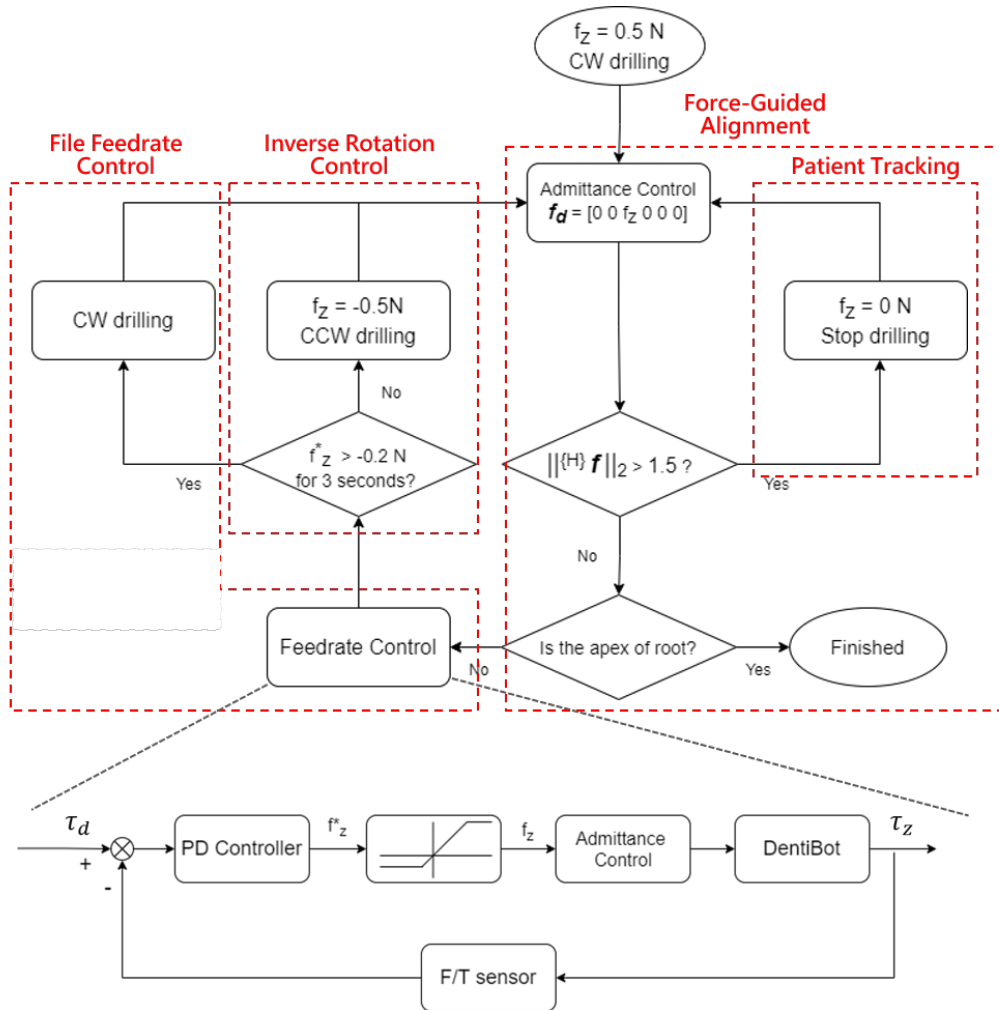


Figure 5.8: Flowchart of the algorithm for autonomous endodontic treatment

in Figure 5.6, inverse rotation control is involved as shown in the left part. The minimum and maximum saturation is from  $-0.5$  to  $0.5$ . When the file torque exceeds the desired torque, Feedrate control will slow down the feed by output

$f_z^*$  with a negative value. If the file torque exceeds a little and  $f_z^*$  does not reach  $-0.2$ , the file will keep clockwise drilling. The above function is essential because it provides file feedrate control a feasibility to regulate the torque. On the contrary, once the file torque exceeds much and  $f_z^*$  is smaller than  $-0.2$ , it will trigger the inverse rotation control. That means the file torque increases dramatically so that file feedrate control can not handle with.

# Chapter 6

## Experimental Results

For checking and validating the proposed method, we set up experiments from technical and pre-clinical perspectives. In the first experiment with a technical perspective, admittance control, force-guided alignment, and file feedrate control were conducted and verified. On the other hand, in pre-clinical evaluation, acrylic root models before and after performing endodontic treatment with DentiBot were also compared in this chapter.

### 6.1 Experimental Setup

#### Software and Firmware Setup

To control and communicate with all devices in low latency and high speed, a communication protocol - Ethernet for Control Automation Technology (EtherCAT) and a real-time operating system (RTOS) are interfaced. EtherCAT (Beckhoff Automation, Verl, Germany) is constructed on EtherNET and utilizes "processing on the fly" technology. Therefore, it provides a short cycle time (less than 100  $\mu$ s) and low jitter. Besides, EtherCAT supports every type of network topologies such as daisy chain, star, and ring. All devices are connected in Daisy-chain with EtherCAT as shown in Figure 6.1. Graph user interface (GUI) and fundamental framework are constructed to reduce and eliminate future developing problems as

shown in Figure 6.2.

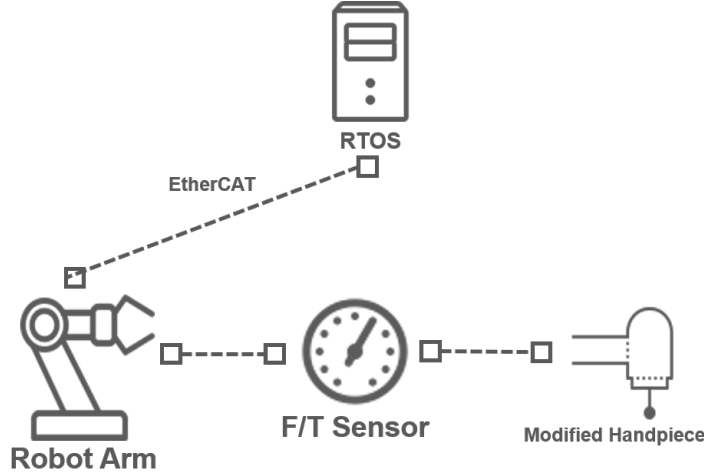


Figure 6.1: Communication protocol – EtherCAT. Master device is RT-target and

slave devices are robot arm, F/T sensor and modified handpiece.

### Hardware Setup

In Figure 6.3, a motion capture system – Impulse X2E (PhaseSpace, San Leandro, CA) is incorporated to obtain the handpiece and root positions . There were four cameras with high resolution sensor around the robot and their resolutions are around 1 mm. The motion capture system can capture LEDs and calculate their Cartesian position for 960 frames per second. Moreover, a Stewart platform on which a root acrylic model is mounted is set up to simulate a small patient moving.

To record the handpiece and root positions, a LED marker is located on the driller and the other three LED markers forming a equilateral triangle are seated on the Stewart platform. Therefore, the handpiece position is directly obtained and

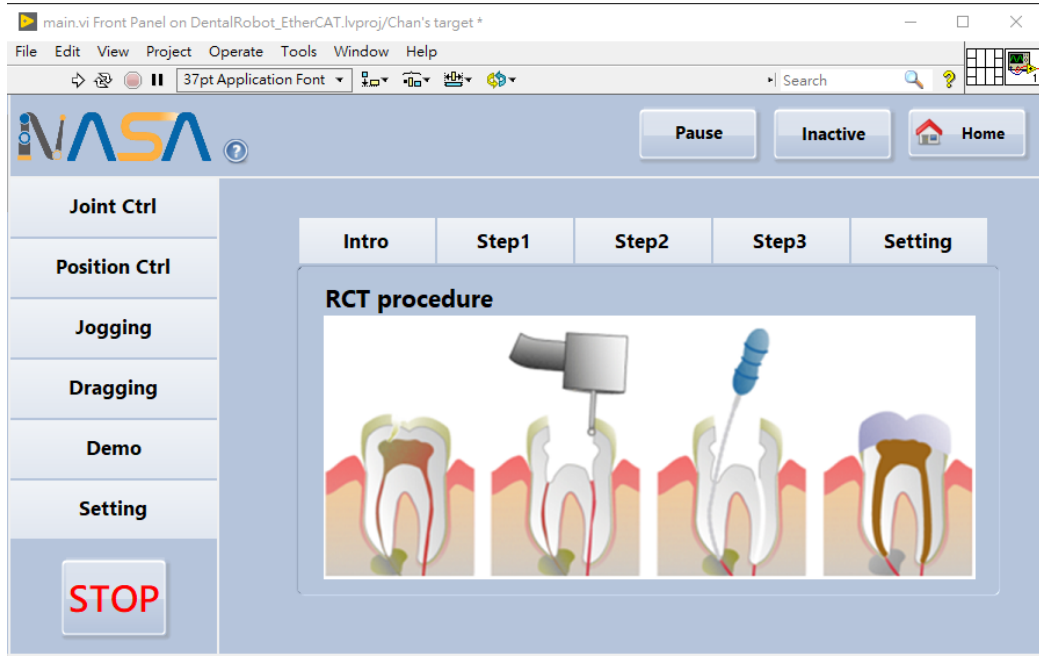


Figure 6.2: Graph user interface with LabVIEW 2018

the root position is calculated as following equation

$$p_{root} = \frac{p_1 + p_2 + p_3}{3}$$

where  $p_{root}$  denotes the root position and  $p_i$  denote the positions of LEDs obtained from the motion capture system.

Also, the positions related to the motion capture system frame are transformed to the Stewart platform frame. Note that there is an original offset in the vertical direction between the root and handpiece in this setup. This original offset is around 55 mm. This original offset will magnify the relative distance on the X-axis and Y-axis. Also, An inaccurate 3-D print supports used to stick three LEDs and acrylic roots lead to wrong centroid point and position biases. The flexible property of endodontic files absorbs contact forces and delays response time. The root



Figure 6.3: Experimental setup with DentiBot, a motion-capture system capturing LEDs, and a Stewart platform simulating patient moving

acrylic model has drilled thoroughly by a file and forms a cone shape in advance. Therefore, there is another bias between the root and the endodontic file. Besides, if the motion capture system captures a LED with less than three cameras, the position information will be incorrect. To obtain stable data, four cameras are set up around DentiBot and the Stewart platform. Therefore, there are many factors to affect the position result and should be in afterward discussion.

The specifications of the hardware and software environment set in the experiments are listed in Table 6.1. The detail specifications of the robot arm and F/T sensor are shown in Table 6.2 and Table 6.3.

Table 6.1: Specifications of the hardware and software environments

Item	Specification
Development Environment	LabVIEW 2018
Real-Time Operating System	National Instrument-RT target CPU: Intel Core 8
Communication Protocol	EtherCAT
Robot Arm	Mecademic-Meca500
F/T Sensor	ATI-Mini40
Handpiece Motor	Maxon - servo motor Gear ratio: 67
Motion Capture System	PhaseSpace-Impulse X2E Resolution: 1mm
Stewart Platform	Actuoanix - Linear Actuator

Table 6.2: Technical specifications of the robot arm - meca500

Payload	0.5 kg
Repeatability	0.005 mm
Reach (at wrist center)	260 mm
Total weight	4.5 kg
Joint range	joint 1: $-175^\circ$ to $+175^\circ$ joint 2: $-70^\circ$ to $+90^\circ$ joint 3: $-135^\circ$ to $+70^\circ$ joint 4: $-170^\circ$ to $+170^\circ$ joint 5: $-115^\circ$ to $+115^\circ$ joint 6: $\pm 100$ revolutions
Speed of joints 1–6	150, 150, 180, 300, 300, 500 °/s
Brakes	On joints 1, 2 and 3
Robot mounting	Any orientation
Safety module	Category 3, PL d
Power supply	90-264 VAC, 50-60 Hz (in) / 24 VDC (out)
Communication	TCP/IP, EtherCAT, Ethernet/IP
Controller	Embedded in robot base
Protection rating	IP 40

Table 6.3: Technical specifications of the F/T sensor - mini40

Weight	0.0499 kg
Diameter	40 mm
Height	12.2 mm
Sensing range	Fx,Fy: 20 N  Fz: 60 N  Tx,Ty: 1 Nm  Tz: 1 Nm
Resolution	Fx,Fy: 1/100 N  Fz: 1/50 N  Tx,Ty: 1/4000 Nm  Tz: 1/4000 Nm
Single-axis overload	Fxy: $\pm 810$ N  Fz $\pm 2400$ N  Txy $\pm 19$ Nm  Tz $\pm 20$ Nm
Stiffness (calculated)	X-axis & Y-axis forces (Kx, Ky): $1.1 \times 10^7$ N/m  Z-axis force (Kz): $2.0 \times 10^7$ N/m  X-axis & Y-axis torque (Ktx, Kty): $2.8 \times 10^3$ Nm/rad  Z-axis torque (Ktz): $4.0 \times 10^3$ Nm/rad
Resonant Frequency	Fx, Fy, Tz: 3200 Hz  Fz, Tx, Ty: 4900 Hz

## 6.2 Force-Guided Alignment

The aim of this experiment was to validate the feasibility of force-guided alignment and patient tracking while the handpiece was drilling the root. We set up three experiments with different scenarios. The metric was to check whether it was possible that DentiBot inserted an endodontic file into a small root and confronted a patient moving at the same time.

Three experiments were designed with three configurations listed below and shown in Figure 6.4.

Config. A – Inserting without file rotation

Config. B – Inserting with file rotation

Config. C – Inserting with file rotation and file feedrate control

To simulate a patient moving, a Stewart platform with six degrees of freedom was incorporated. When the patient moved to a point, our system should move to the same place. Therefore, the target and handpiece positions would be compared to check if our system tracked the patient or not. PhaseSpace - Impulse X2E, a motion capture system, was involved in obtaining the above positions in real-time.

The Stewart platform was scheduled for motion planning. It would move to (0, 0, 0), (15, 0, 0), (15, 0, 15), (0, 0, 15) related to Stewart frame. These points formed a 15 \* 15 mm square composed of two horizontal and two vertical lines. The command position trajectory is illustrated in Figure 6.5. The Stewart platform

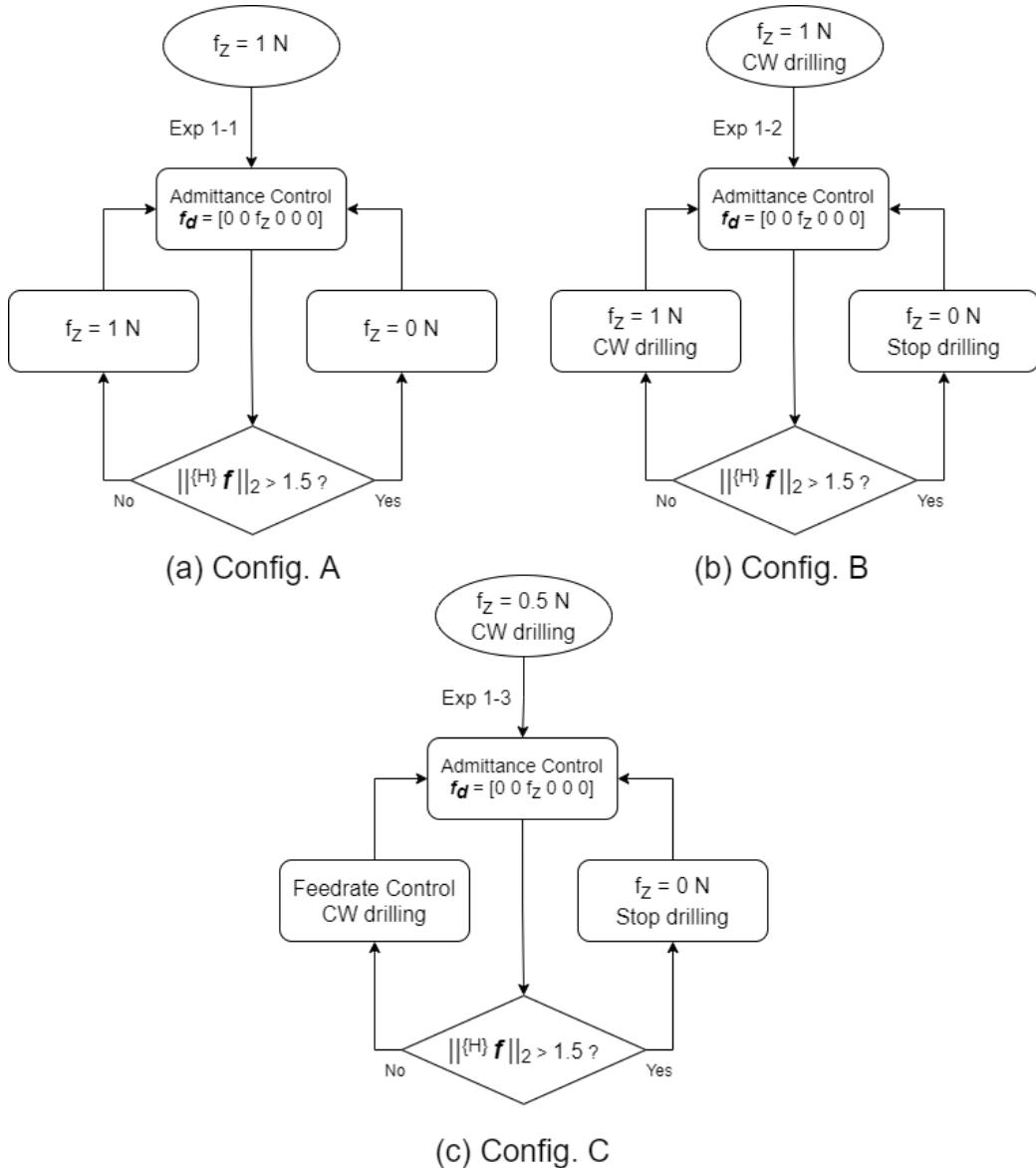


Figure 6.4: Flow charts for force-guided alignment experiment. (a) shows Config.A – inserting without file rotation. (b) shows Config.B – inserting with file rotation. (c) shows Config.C – inserting with file rotation and file feedrate control.

is planned to go along with a square at 3 mm/s first, then stop for 10 seconds, then go along with a square at a faster velocity, and so on. The velocities of four rounds are 3 mm/s, 4 mm/s, 5 mm/s, and 6 mm/s. Each cycle took 20, 15, 12, 10 seconds separately and total experiment time was 87 seconds. Note that, in reality, linear interpolation was implemented to command the Stewart platform. The motion of the Stewart platform was received  $4 \times 100$  steps and executed at an equally distributed time. Even though these 4 points were cut to 400 points and then calculated by inverse kinematics, the X-axis motion still had an apparent distortion due to the hardware assembly error.

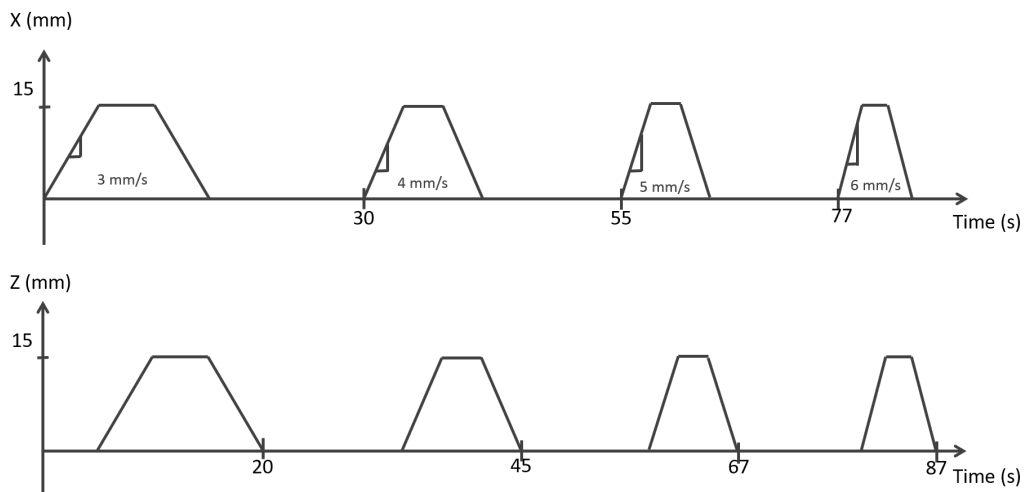


Figure 6.5: Position command of Stewart platform for force-guided alignment experiment

Parameters setting of admittance control in Experiment 1 is shown in Table 6.4. The parameter diagonal matrix  $\mathbf{K}$  is proportional to the gain, and  $\mathbf{B}$  is inversely proportional to the gain. Therefore, the same values are set in all experiments

except  $b_6$ .  $b_6$  is relevant to the rotation along with Z-axis. The rotation along with Z-axis driven by the robot arm should be deactivated in Config. A and B because the file rotation is driven by the motor. If the rotation along with Z-axis is on duty and the file is drilling, the robot arm would rotate along with Z-axis in the opposite direction. Hence,  $b_6$  is set an infinite value to deactivate the rotation along with Z-axis. Config. C is the last technical experiment and is designed as a pre-clinical task, but the metrics are still the same as the previous experiment. Because a slow inserting is required when performing the endodontic treatment. Therefore, the maximum value of  $f_z$  was set 0.5 in Config. C to limit the highest velocity.

Table 6.4: Parameters setting of admittance control in Experiment 1.

Parameter	Config. A	Config. B	Config. C
$k$	500	500	500
$f_z$	1	1	$-0.2 \sim 0.5$
$b_1$	80	80	80
$b_2$	80	80	80
$b_3$	80	80	80
$b_4$	80	80	80
$b_5$	80	80	80
$b_6$	80	$\infty$	$\infty$

$$\mathbf{K} = \text{diag}(k, k, k, k, k, k), \mathbf{B} = \text{diag}(b_1, b_2, b_3, b_4, b_5, b_6)$$

## Results

There were three metric types of figures to show the results of Config. A, B, and C listed as following.

1. The position of handpiece and root and their relative distance
2. The force vs the velocity
3. The force vs the handpiece position

Note that the real position and velocity data were transformed from the Phas-eSpace frame to the Stewart platform frame. The force information were also transformed to the Stewart platform frame from the handpiece frame. Therefore, all data were all considered in the Stewart frame.

The first metric type of figure is comparing the handpiece position with the root position and their relative distance. Config A, B, and C were separately plotted in Figure 6.7, 6.8, and 6.9 and were discussed together here.

First, the trajectory of the Stewart platform was analyzed as shown in Figure 6.6. Distortion of platform moving occurred and led to be different from the position command of Stewart platform. There was a apparent distortion around 3 mm on X-axis when the platform was moving along with Z-axis. This distortion led to the fact that each cycle in the position plot on X-axis is not a trapezoid. The Stewart platform moving along with X-axis was smooth, so the position plot on Z-axis is a typical trapezoid. Therefore, the relative distance between the handpiece and the root became the most essential metric.

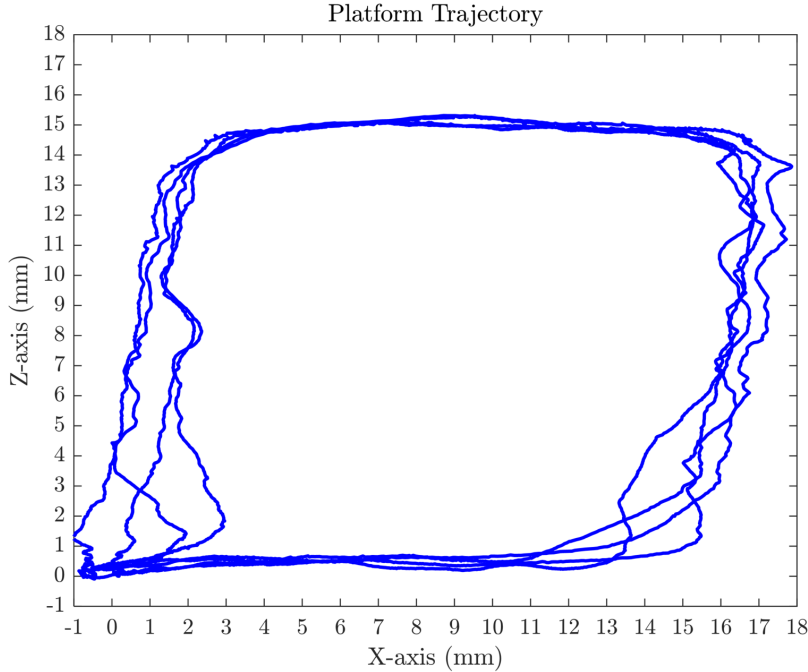


Figure 6.6: Patient trajectory simulated by Stewart platform

In Figure 6.7, 6.8, and 6.9, there are total six subplots in each figure. The left three subgraphs show position information in X-axis, Y-axis and Z-axis, and the right three subgraphs show the relative distance in X-axis, Y-axis, and Z-axis. The handpiece position is the solid blue line, and the root position the dotted blue lines, and the relative distance between the handpiece and the root position is the solid red line. Note that there is an original offset of around 55mm in the vertical direction between the root and handpiece. Therefore, the scale for the relative distance on Z-axis is different from X-axis and Y-axis.

First, we could find that there is a phase difference between the root position and the handpiece position on X-axis . The main reason is that the file property is

superelastic and delays the response time when the file bears a contact force.

Compared all X-axes and Y-axes from Config. A to C, the maximum relative distance are all around 3 mm. This relative distance is acceptable because it came from many errors caused by the motion capture system, the 3-D print support, and the flexible property of the endodontic file. On Z-axis, the maximum relative distance in Config.A approximately retains at 55 mm; as for Z-axis, in Config.B there is a ripple at 87th second. It is due to the file leaving out of the root when the platform was moving down along with Z-axis. The file chased the root because  $f_z$  made DentiBot insert and the relative distance went back to the original offset after a few seconds. Why the file is easy to leave out of the root in Config. B and not in Config. A is the file rotation. As for Z-axis of Config. C, ripples were expected because the maximum  $f_z$  was half of the previous. With the velocity is increasing, ripples are getting bigger. At 6 mm/s velocity, the maximum relative distance is around 5 mm. After around 5 seconds, it could go back to the original offset.

In conclusion, from Config. A to C, the maximum relative distances were all retained in an acceptable error. Despite that Config. C had a significant detachment between the endodontic file and the root, the file could track and go back to the original offset. It is worth noting that there is a distortion when the Stewart platform moves along with Z-axis, which means the force-guided alignment could track and compensate the surgical path in real-time with high performance in uncertainty.

The second metric type of figure is comparing the detected force with the command velocity and the real velocity. Config. A , B, and C were plotted in

## 6. Experimental Results

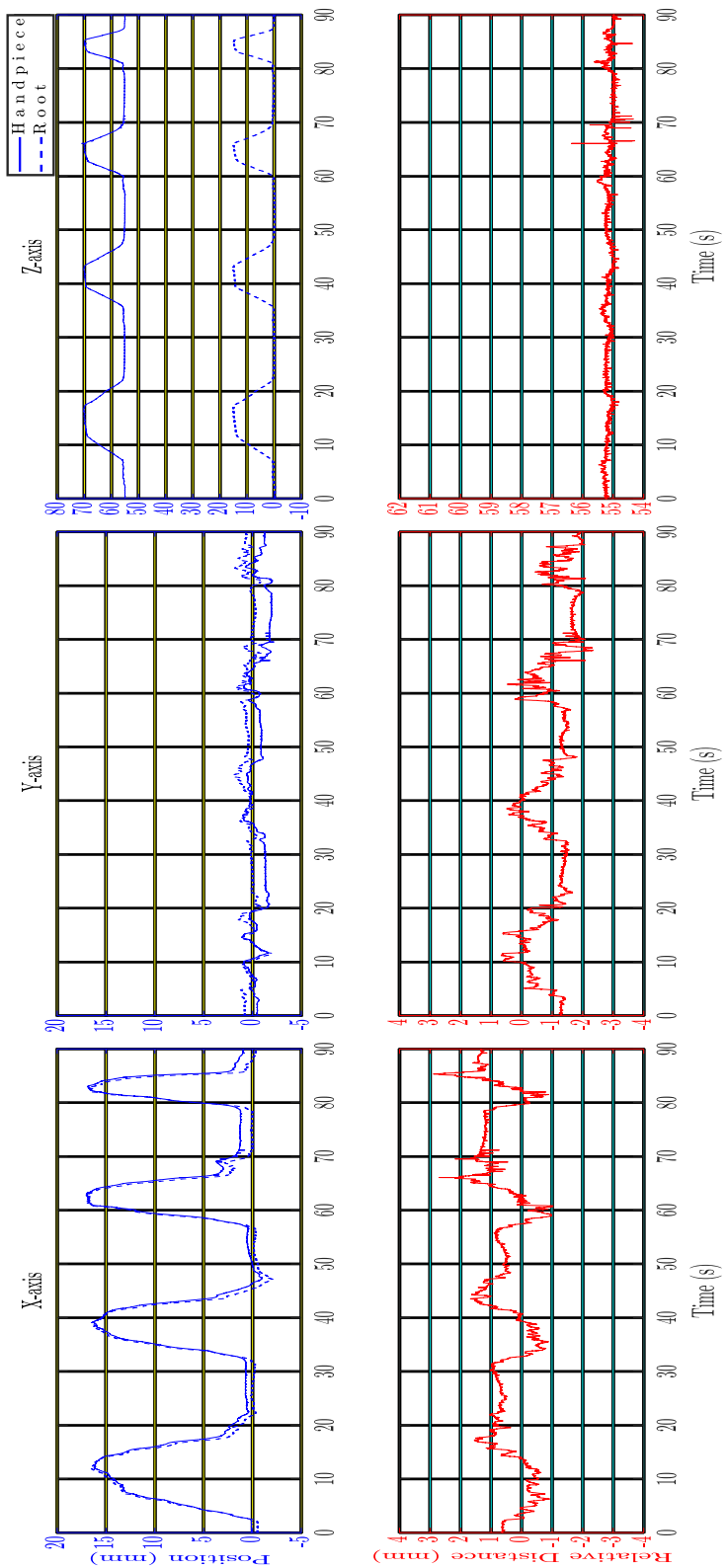


Figure 6.7: Config. A: Handpiece position vs root position root and their relative distance

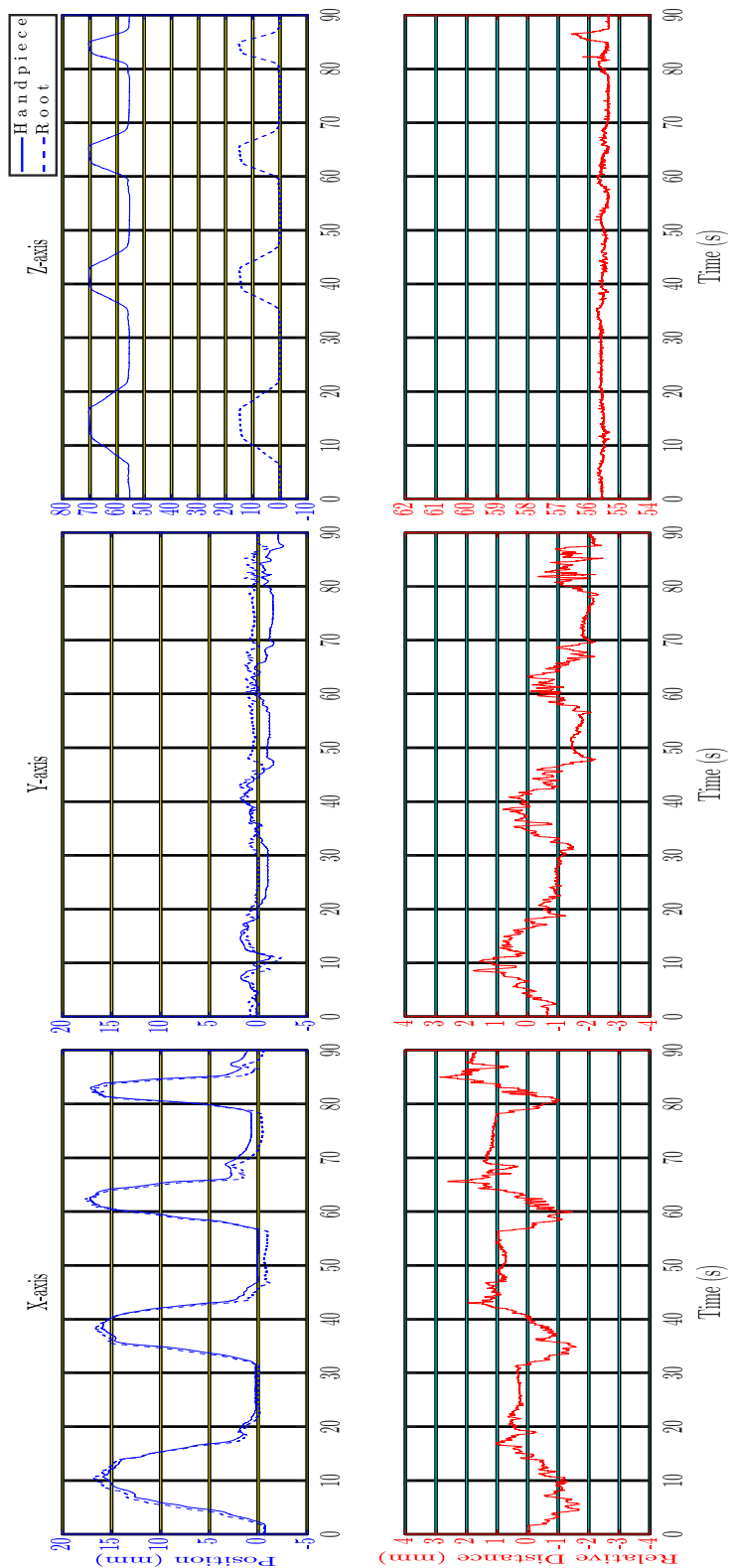


Figure 6.8: Config. B: Handpiece position vs root position root and their relative distance

## 6. Experimental Results

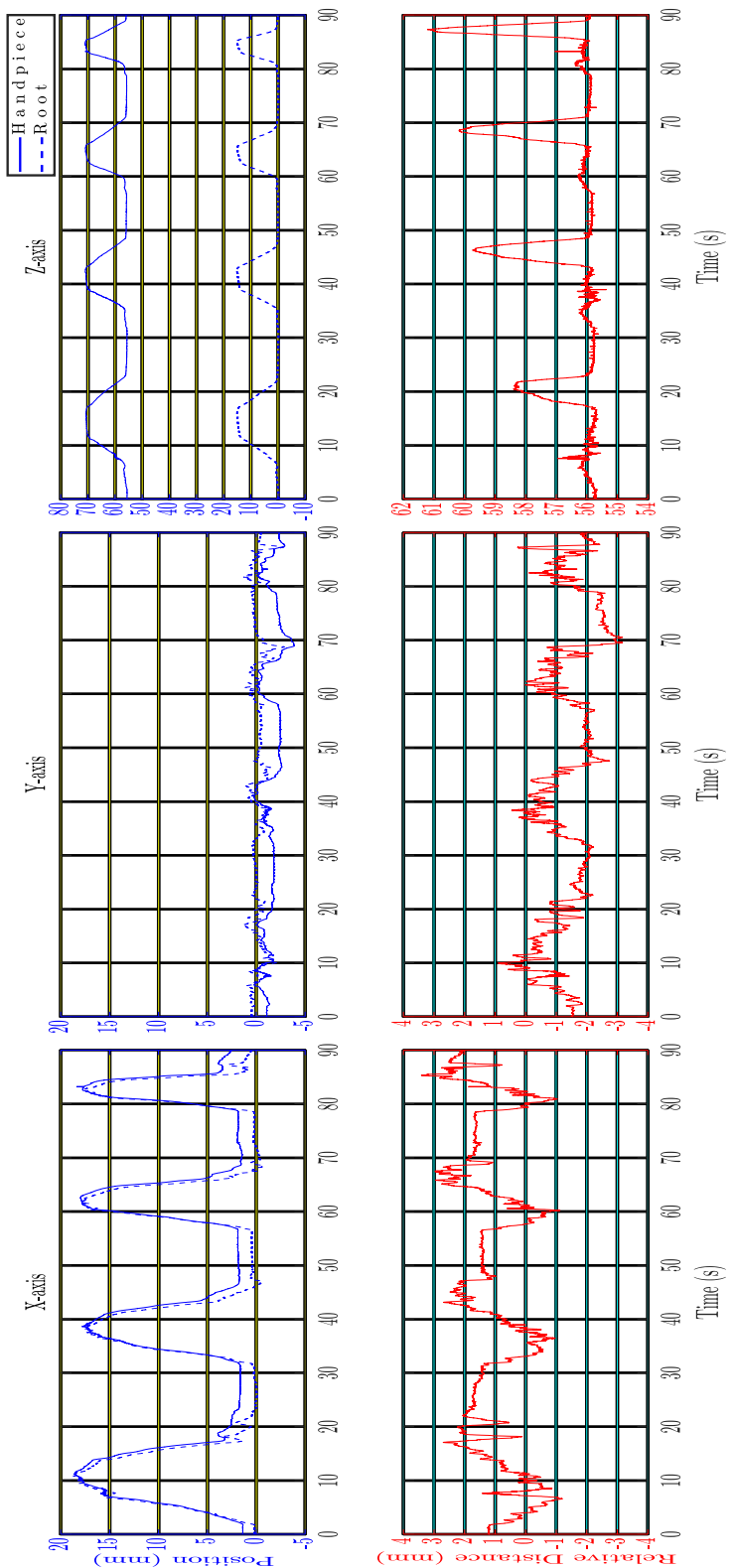


Figure 6.9: Config. C: Handpiece position vs root position root and their relative distance

Figure 6.11, Figure 6.12, and Figure 6.13 and were discussed together here. In theory, the force should match the command velocity and have a highly positive correlation to the real velocity. From Config. A to Config. C, three plots are similar, overall the results compared to the theory are all correct. However, two phenomena occurred on Z-axis. The first phenomenon is that there is oscillation due to excessive velocity caused by a large value of  $f_z$ . Too fast velocity would produce excessive force than the desired force when the file contacts the root bottom and lead to an opposite move. The other phenomenon is zoomed in and shown in Figure 6.10. The difference between the command and real velocity is caused by the detachment between root and file.

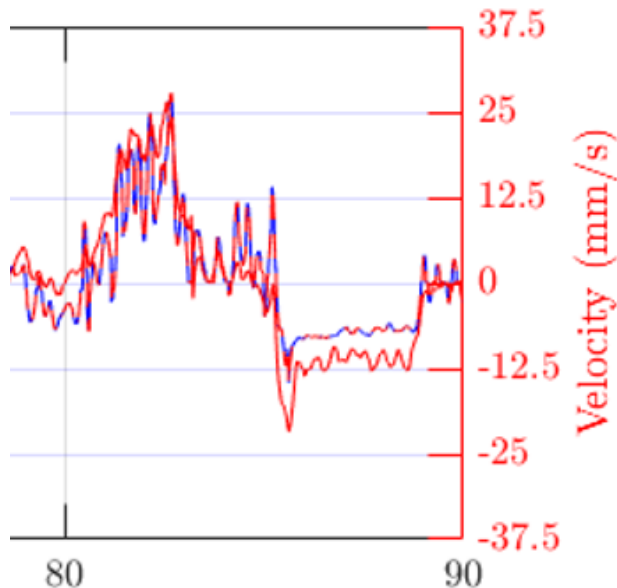


Figure 6.10: Zoom-in plot of Force vs Velocity on Z-axis from 80th to 90th second

The third metric type of figure is comparing the detected force with the hand-

## 6. Experimental Results

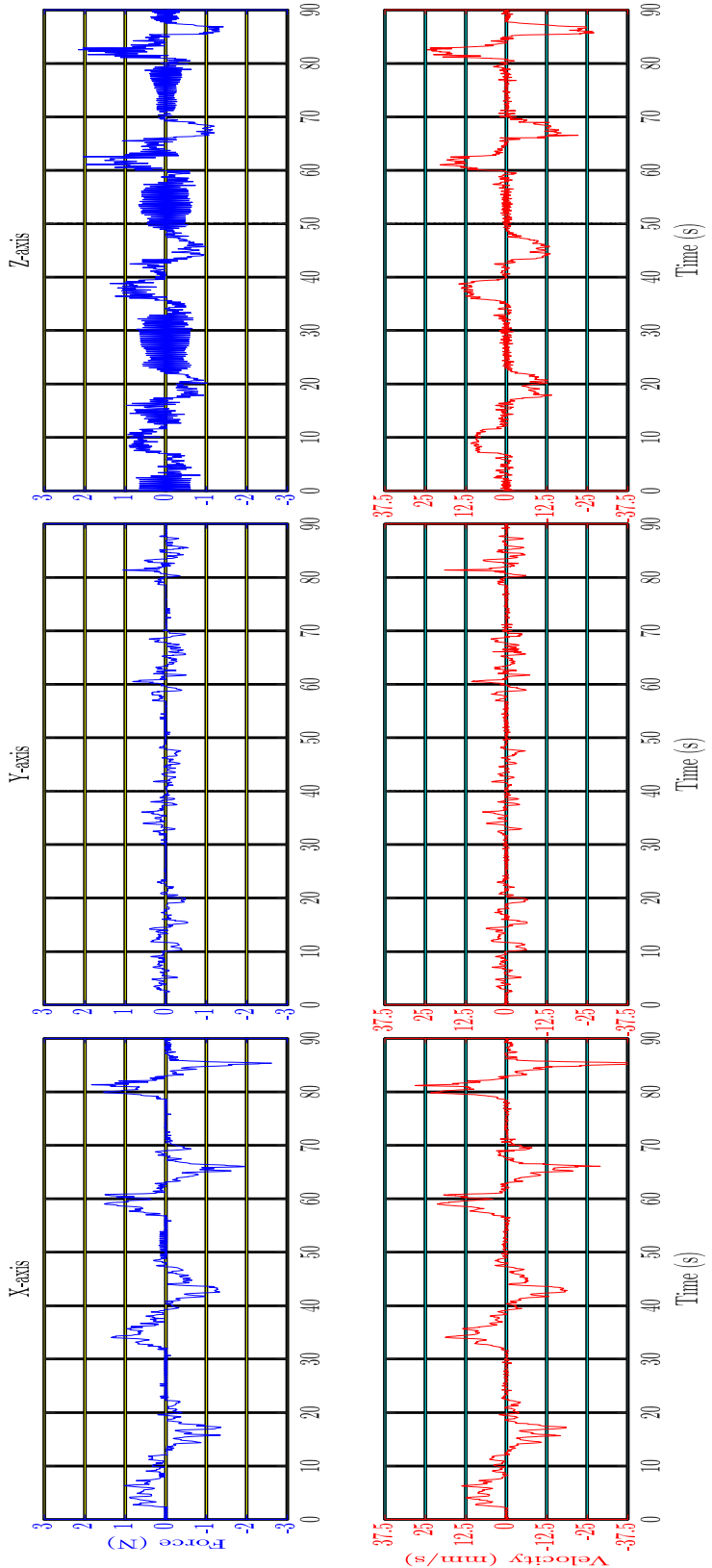


Figure 6.11: Config. A: Force vs Velocity and Velocity command

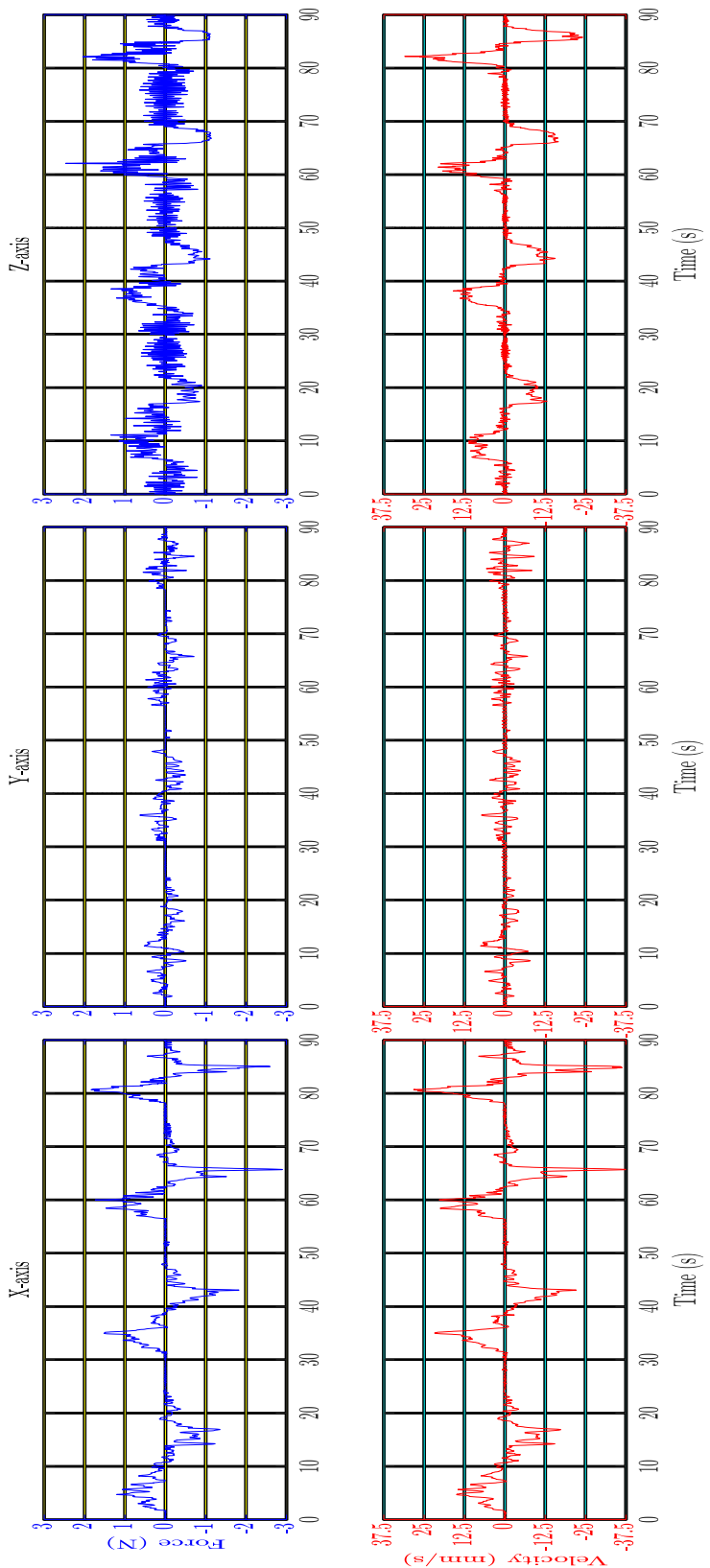


Figure 6.12: Config. B: Force vs Velocity and Velocity command

## 6. Experimental Results

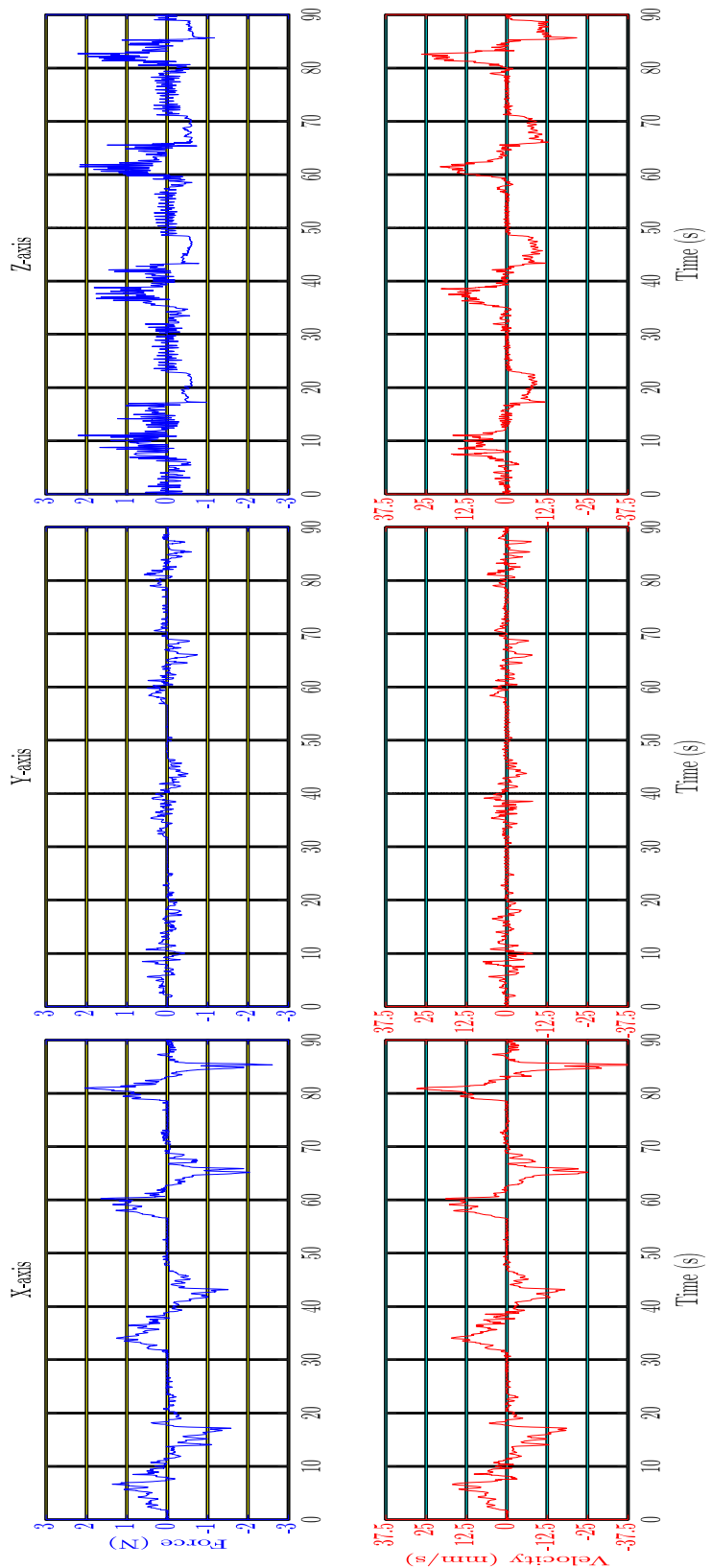


Figure 6.13: Config. C: Force vs Velocity and Velocity command

piece position. Config. A , B, and C were plotted in Figure 6.14, Figure 6.15, and Figure 6.16 and were discussed together here. An oscillation occurred on Z-axis is due to excessive velocity caused by a large value of  $f_z$ . A large value of  $f_z$  means a faster inserting velocity. Once the file contacts the bottom of root, the opposite force is produced and detected by the F/T sensor. The contact velocity is faster, then the opposite force is larger. Therefore, if the opposite force is larger than the desired force, DentiBot will move to the opposite direction. However, the opposite move will decrease the detected force and then make DentiBot move forward again. That is why the oscillation occurs.

### Conclusion of Force-Guided Alignment Experiment

To conclude the experiment 1, the maximum relative distances on X-axis and Y-axis were all retained within 3 mm. 3 mm was an acceptable error because it could be the result of the inaccurate 3-D print support, the flexible property of endodontic files, and the motion capture system error. Despite that Config. C had a significant detachment between the endodontic file and the root, the file could track and go back to the original offset. Patient moving within 15 mm is proved to be allowed because the force-guided alignment could track and compensate the surgical path in real-time with low error. Therefore, the experiment result has proved the feasibility of combining force-guided alignment, file feedrate control and patient tracking.

## 6. Experimental Results

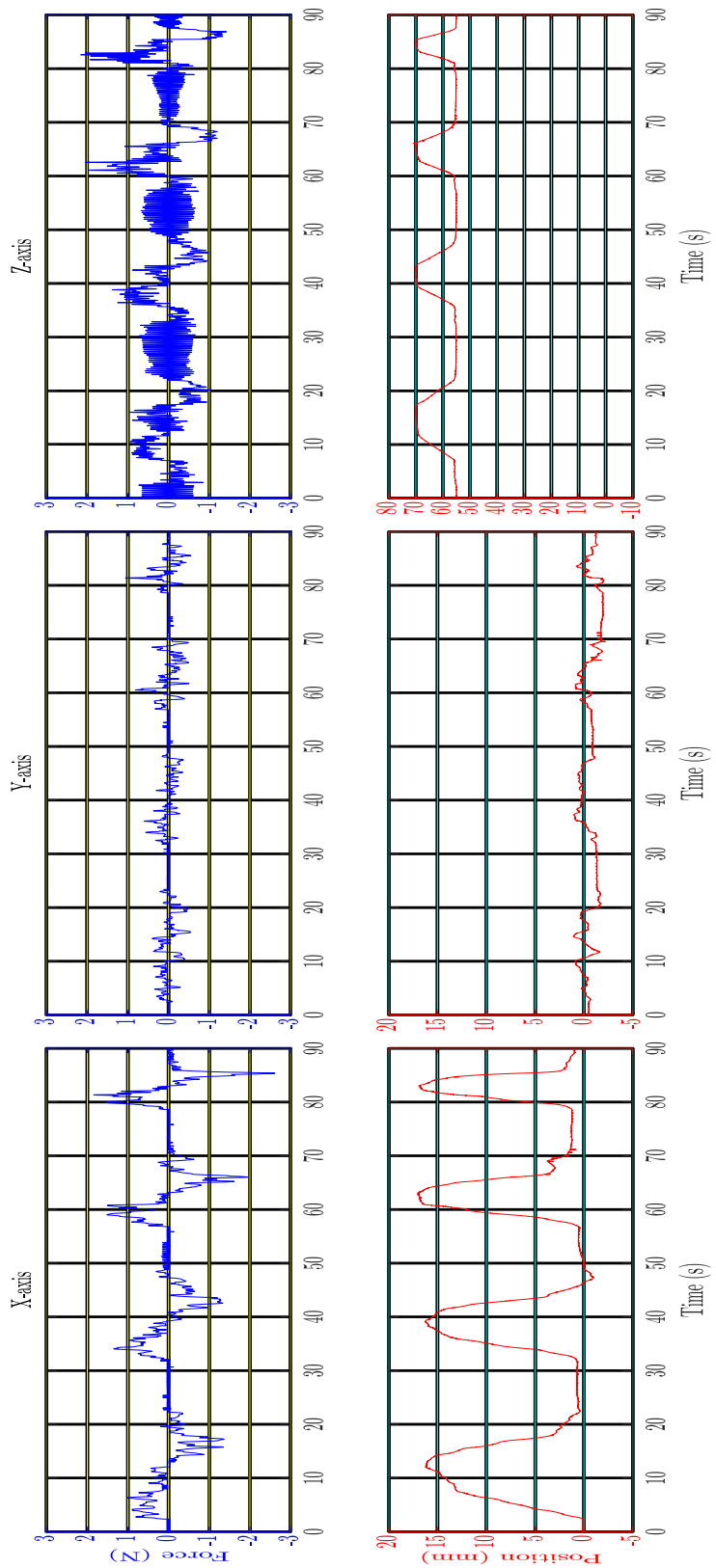


Figure 6.14: Config. A: Force vs Handpiece position

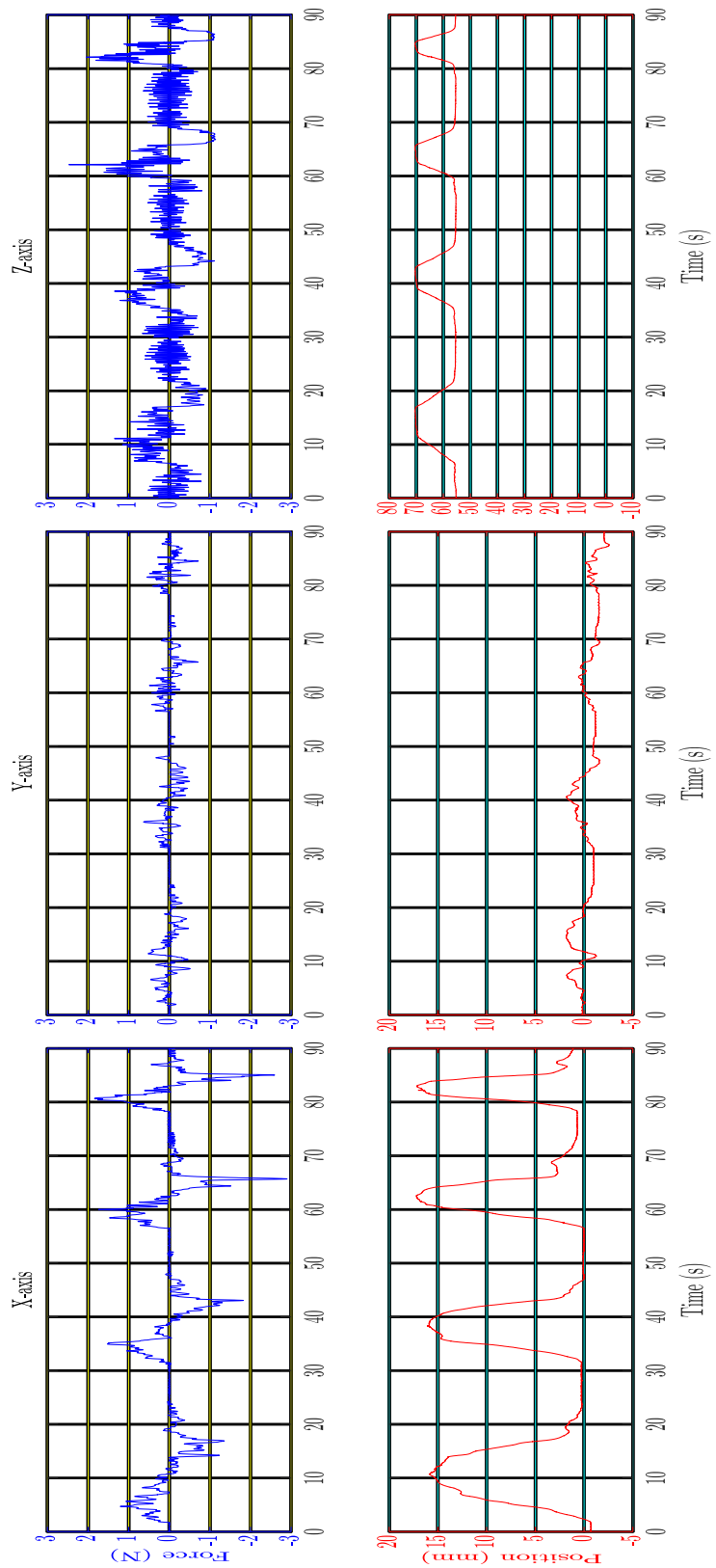


Figure 6.15: Config. B: Force vs Handpiece position

## 6. Experimental Results

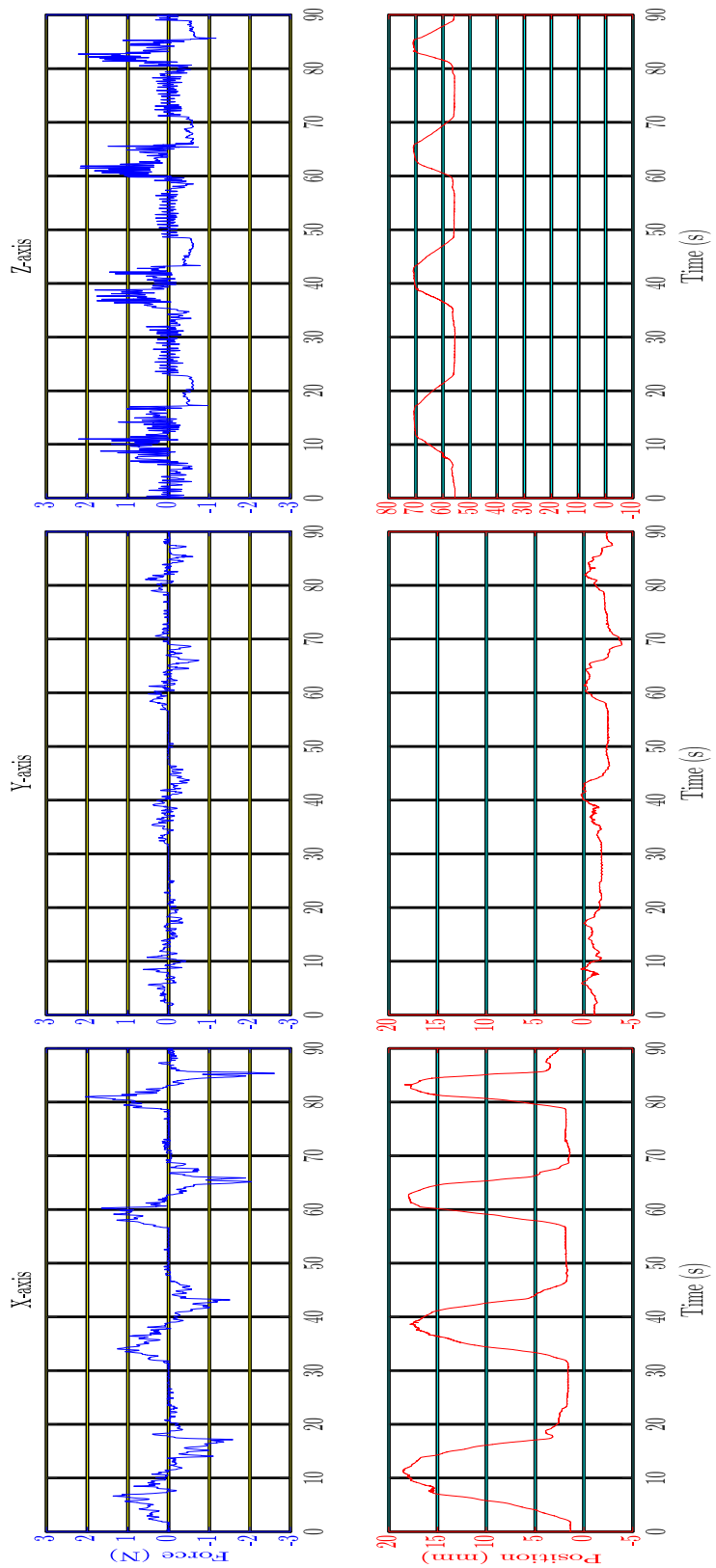


Figure 6.16: Config. C: Force vs Handpiece position

## 6.3 Pre-Clinical Evaluation

We have verified the feasibility of combining force-guided alignment, file feedrate control. In what follows, an algorithm that combines all functions including force-guided alignment, patient tracking, inverse rotation control, and feed control were implemented in the pre-clinical trial as shown in Figure 6.17.

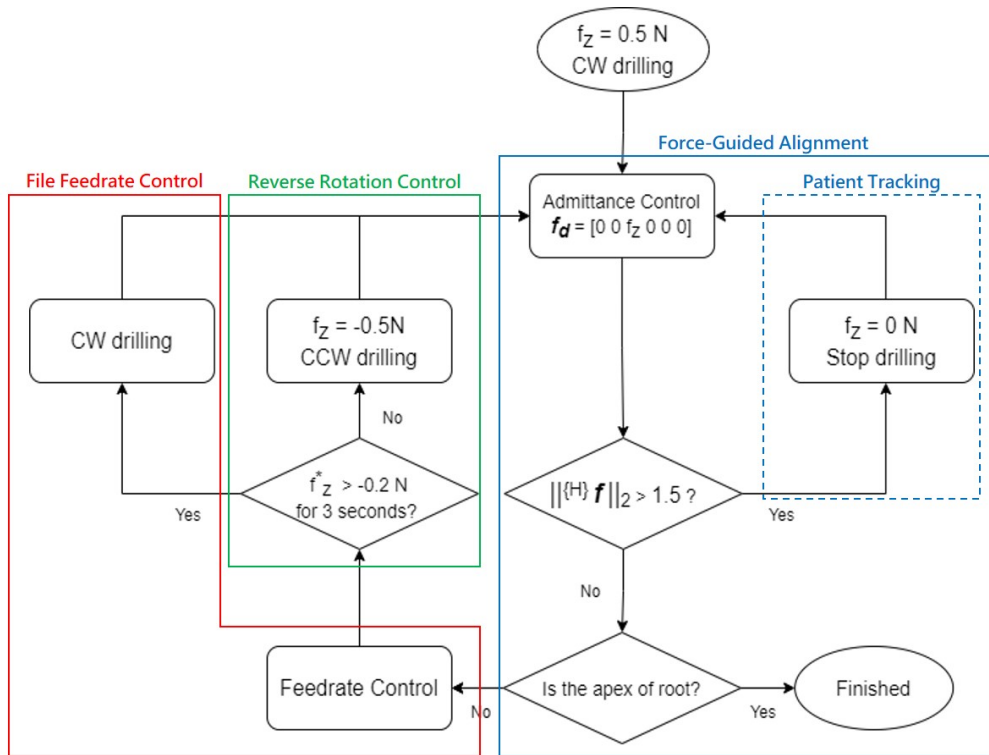


Figure 6.17: Flowchart of the algorithm for autonomous endodontic treatment

The metrics of the pre-clinical trial were completeness of root preparation and whether instrument fracture happened. To compare the completeness before and after the surgery, acrylic root phantoms were involved. The acrylic root phantoms were widely used in the operative technique classroom to simulate the clinical

situations. Intern dentists practised the endodontic techniques with acrylic root phantoms. To simulate and visualize the pulp in roots, red pigment was filled with roots shown in Figure 6.18. The top of the model is a cone shape and is not included to calculate the completeness because the cone area is not the drilling area. Therefore, the red line depicted in the figure is the calculated length.

Hence, completeness is defined as

$$\text{Completeness} = \frac{R_b - R_a}{R_b} \times 100\% \quad (6.1)$$

where  $R_b$  denotes the red area before the treatment.  $R_a$  denotes the remained red area after the treatment.

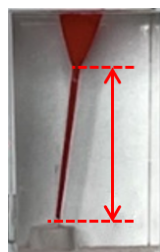


Figure 6.18: Acrylic root phantom used in operative technique practice

Note that the acrylic root phantoms were all different due to manufacture process. Conditions of the acrylic root phantoms might be straight, titled, or even curve.

Six root models, A to F, were divided into two groups. The desired torque  $\tau_d$  in file feedrate control was set 40 and implemented in A, B, and C. On the other hand,  $\tau_d$  was set 50 in D, E, and F. Each model was treated for two times. The first round took 300 seconds and the second round took 200 seconds.

## Result

In Figure 6.19, six root models before and after treatment are compared. There is few remained red pigment within roots. Besides, the roots were all shaped to cone shapes without ledging. Ledging is an irregular platform caused by an inappropriate operation such as too much force while drilling. Once ledging happens, it would impede the endodontic files to the apex. The results without ledging proved that force-guided alignment was effective to adjust the surgical path in real-time.

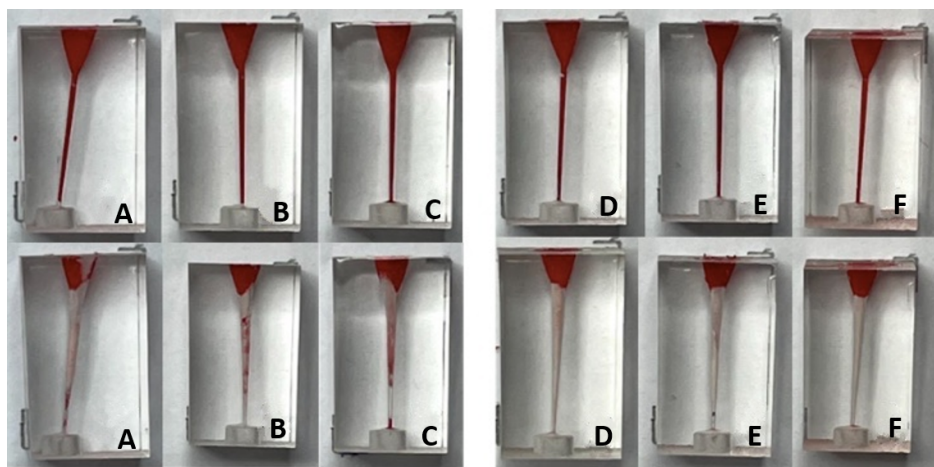


Figure 6.19: Experiment 2: A comparison of completeness before and after two times drilling.  $\tau_d$  were set 40 in A,B,C and 50 in D,E,F

To dissect the completeness, the root images were evaluated by image processing and shown in Table 6.5. The average completeness of A, B, C is 88.41% and the average completeness of D, E, F is 99.2%. It means that  $\tau_d$  50 below the maximum file bearing torque 62 had higher completeness than  $\tau_d$  40. However, no

matter  $\tau_d$  was 40 or 50, it could both achieve high performance in root preparation and prevent instrument fracture.

Table 6.5: Results of pre-clinical evaluation

Number	Preoperative	Postoperative	Completeness	Instrument
	Red Area (pixel)	Red Area (pixel)		Fracture
A	15652	795	94.92%	No
B	17316	2418	86.04%	No
C	17403	2738	84.27%	No
D	16114	53	99.67%	No
E	17047	185	98.91%	No
F	18482	180	99.03%	No

### Conclusion of pre-clinical evaluation

In this experiment, the performance of root preparation using our robot was demonstrated. No ledging in all postoperative acrylic root phantoms proved that force-guided alignment could adjust the surgical path in real-time. Preoperative and Postoperative root models were evaluated their completeness and compared. The results verified the feasibility of robot-assisted endodontic treatment.

# **Chapter 7**

## **Conclusions and Future work**

An endodontic treatment is a challenging surgery for dentists due to complex conditions of teeth. Therefore, building a robot-assisted system for the endodontic robot requires comprehensive consideration on whole surgery procedures. Review the section 1.4, we advocated the four parts of the project prospect. We highlight two main parts of the prospect and have proved the feasibility of our proposed approaches. The whole work of the thesis is concluded in this chapter.

### **7.1 Conclusions**

Nowadays, despite that there are more and more dental robots springing up, there are still few teams specific to endodontic treatment. In view of this, our team has built the robot-assisted system – DentiBot – composed of a 6-DoF robot arm, a 1-DoF modified handpiece, and a 6-DoF F/T sensor. System integration solutions between the above devices are reviewed. DentiBot can assist dentists in performing endodontic treatment as a consequence of the following functions.

Admittance control based on F/T sensor is implemented to enable dentists to move DentiBot above an infected tooth. Also, a framework based on admittance control for real-time force-guided alignment is presented to adjust surgical path

and compensate patient moving. "Dragging Mode" and "Self-Alignment Mode" are separately implemented for the above functions.

Moreover, instrument fracture is a severe iatrogenic error for dentists and might lead to a medical dispute. With the torque monitoring system, inverse rotation control and file feedrate control were applied to reduce the possibility of instrument fracture.

Experiments proved the feasibility in technical and clinical perspectives. Experiment 1 demonstrated the performance of force-guided alignment and file feedrate control. Experiment 2 is a pre-clinical evaluation and verify the feasibility of robot-assisted endodontic treatment. Undoubtedly, DentiBot can help dentists perform better clinical results.

## 7.2 Discussion and Future Work

The thesis is the pioneer of the endodontic project. Despite that the thesis develops DentiBot and presents the above functions, there are some remained works and rooms for improvement on the modified hardware and functions. The modified handpiece made by 3-D prints is not durable for a time-consuming endodontic treatment. It is necessary to do machining for more stable results.

In the thesis, we hypothesize that a dentist moves DentiBot above the root, then DentiBot does the "Cleaning" procedure. However, sometimes there is not only one root in the tooth. For instance, there are three to four roots in a molar. Therefore, DentiBot should have the ability to search all root canals after moved

above the infected tooth.

On top of that, we proposed the alignment method while DentiBot does drilling. It not only aligns with the root path but also with patient moving. However, this patient tracking belongs to a minor range movement. Therefore, DentiBot is expected to be applied to patient tracking with large movement via string potentiometers in the future.

# **Appendices**

## Appendix A    Forward Kinematics

$${}^0_6 \mathbf{T} = {}^0_1 \mathbf{T} \cdot {}^1_2 \mathbf{T} \cdot {}^2_3 \mathbf{T} \cdot {}^3_4 \mathbf{T} \cdot {}^4_5 \mathbf{T} \cdot {}^5_6 \mathbf{T} = \begin{bmatrix} {}^0_6 \mathbf{R}_{3 \times 3} & {}^0_6 \mathbf{p}_{6_{\text{org}}} \\ 0_{1 \times 3} & 1 \end{bmatrix} = \begin{bmatrix} t_{11} & t_{12} & t_{13} & t_{14} \\ t_{21} & t_{22} & t_{23} & t_{24} \\ t_{31} & t_{32} & t_{33} & t_{34} \\ 0 & 0 & 0 & 1 \end{bmatrix}$$

$$t_{11} = -S_6(C_4S_1 + S_4(C_1S_3 - C_2 - C_1C_3S_2)) - C_6(C_5(S_1S_4 - C_4(C_1S_3 - C_2 - C_1C_3S_2)))$$

$$- C_2 - C_1C_3S_2) - S_5(C_1C_3 - C_2 + C_1S_2S_3))$$

$$t_{12} = S_6(C_5(S_1S_4 - C_4(C_1S_3 - C_2 - C_1C_3S_2)) - S_5(C_1C_3 - C_2 + C_1S_2S_3))$$

$$- C_6(C_4S_1 + S_4(C_1S_3 - C_2 - C_1C_3S_2))$$

$$t_{13} = -S_5(S_1S_4 - C_4(C_1S_3 - C_2 - C_1C_3S_2)) - C_5(C_1C_3 - C_2 + C_1S_2S_3)$$

$$t_{14} = 135C_1S_2 - 70S_5(S_1S_4 - C_4(C_1S_3 - C_2 - C_1C_3S_2)) - 70C_5(C_1C_3 - C_2$$

$$+ C_1S_2S_3) - 120C_1C_3 - C_2 - 120C_1S_2S_3 - 38C_1S_3 - C_2 + 38C_1C_3S_2$$

$$t_{21} = S_6(C_1C_4 + S_4(C_3S_2S_1 - S_1S_3 - C_2)) + C_6(C_5(C_1S_4 - C_4(C_3S_2S_1$$

$$- S_1S_3 - C_2)) + S_5(C_3S_1 - C_2 + S_2S_1S_3))$$

$$t_{22} = C_6(C_1C_4 + S_4(C_3S_2S_1 - S_1S_3 - C_2)) - S_6(C_5(C_1S_4 - C_4(C_3S_2S_1$$

$$- S_1S_3 - C_2)) + S_5(C_3S_1 - C_2 + S_2S_1S_3))$$

$$t_{23} = S_5(C_1S_4 - C_4(C_3S_2S_1 - S_1S_3 - C_2)) - C_5(C_3S_1 - C_2 + S_2S_1S_3)$$

$$t_{24} = 135S_2S_1 + 70S_5(C_1S_4 - C_4(C_3S_2S_1 - S_1S_3 - C_2)) - 70C_5(C_3S_1 - C_2$$

$$+ S_2S_1S_3) + 38C_3S_2S_1 - 120C_3S_1 - C_2 - 120S_2S_1S_3 - 38S_1S_3 - C_2$$

$$t_{31} = C_6(S_5(C_3S_2 - S_3 - C_2) + C_4C_5(C_3 - C_2 + S_2S_3)) - S_4S_6(C_3 - C_2$$

$$+ S_2S_3)$$

$$t_{32} = -S_6(S_5(C_3S_2 - S_3 - C_2) + C_4C_5(C_3 - C_2 + S_2S_3)) - C_6S_4(C_3 - C_2 + S_2S_3)$$

$$t_{33} = C_4S_5(C_3 - C_2 + S_2S_3) - C_5(C_3S_2 - S_3 - C_2)$$

$$t_{34} = 120S_3 - C_2 - 120C_3S_2 - 38C_3 - C_2 - 38S_2S_3 - 135 - C_2$$

$$- 70C_5(C_3S_2 - S_3 - C_2) + 70C_4S_5(C_3 - C_2 + S_2S_3) + 135$$

## Appendix B Jacobian Matrix

**Jg0**

$$j_{g0,21} = 135C_1S_2 - 120C_1S_2S_3 - 70S_1S_4S_5 + 120C_1C_2C_3 + 38C_1C_2S_3$$

$$+ 38C_1C_3S_2 + 70C_1C_2C_3C_5 - 70C_1C_5S_2S_3 - 70C_1C_2C_4S_3S_5$$

$$- 70C_1C_3C_4S_2S_5$$

$$j_{g0,22} = -S_1(120C_2S_3 - 38C_2C_3 - 135C_2 + 120C_3S_2 + 38S_2S_3 + 70C_2C_5S_3$$

$$+ 70C_3C_5S_2 + 70C_2C_3C_4S_5 - 70C_4S_2S_3S_5)$$

$$j_{g0,23} = -2S_1(60C_2S_3 - 19C_2C_3 + 60C_3S_2 + 19S_2S_3 + 35C_2C_5S_3$$

$$+ 35C_3C_5S_2 + 35C_2C_3C_4S_5 - 35C_4S_2S_3S_5)$$

$$j_{g0,24} = 70S_5(C_1C_4 + C_2S_1S_3S_4 + C_3S_1S_2S_4)$$

$$j_{g0,25} = -70C_5(C_2C_4S_1S_3 - C_1S_4 + C_3C_4S_1S_2) - 70C_{34}S_1S_5$$

$$j_{g0,26} = 0$$

$$j_{g0,31} = 0$$

$$j_{g0,32} = 120S_2S_3 - 120C_2C_3 - 38C_2S_3 - 38C_3S_2 - 135S_2 + 70C_5S_2S_3$$

$$- 70C_2C_3C_5 + 70C_2C_4S_3S_5 + 70C_3C_4S_2S_5$$

$$\begin{aligned}
j_{g0,33} = & \ 120S_2S_3 - 38C_2S_3 - 38C_3S_2 - 120C_2C_3 + 70C_5S_2S_3 - 70C_2C_3C_5 \\
& + 70C_2C_4S_3S_5 + 70C_3C_4S_2S_5 \\
j_{g0,34} = & \ 70C_{34}S_4S_5 \\
j_{g0,35} = & \ 70S_{34}S_5 - 70C_{34}C_4C_5 \\
j_{g0,36} = & \ 0 \\
j_{g0,41} = & \ \theta_4S_1S_2S_3 - \theta_3C_1 - \theta_5C_1C_4 - \theta_4C_2C_3S_1 - \theta_6C_1S_4S_5 - \theta_2C_1 \\
& - \theta_6C_2C_3C_5S_1 - \theta_5C_2S_1S_3S_4 - \theta_5C_3S_1S_2S_4 + \theta_6C_5S_1S_2S_3 \\
& \theta_6C_2C_4S_1S_3S_5 + \theta_6C_3C_4S_1S_2S_5 \\
j_{g0,42} = & \ \theta_5C_1C_2C_3S_4 - \theta_4C_1C_2S_3 - \theta_4C_1C_3S_2 - S_1 - \theta_6C_1C_2C_5S_3 \\
& - \theta_6C_1C_3C_5S_2 - \theta_5C_1S_2S_3S_4 - \theta_6C_1C_2C_3C_4S_5 + \theta_6C_1C_4S_2S_3S_5 \\
j_{g0,43} = & \ \theta_5C_1C_2C_3S_4 - \theta_4C_1C_2S_3 - \theta_4C_1C_3S_2 - S_1 - \theta_6C_1C_2C_5S_3 \\
& - \theta_6C_1C_3C_5S_2 - \theta_5C_1S_2S_3S_4 - \theta_6C_1C_2C_3C_4S_5 + \theta_6C_1C_4S_2S_3S_5 \\
j_{g0,44} = & \ \theta_5(S_1S_4 + C_1C_2C_4S_3 + C_1C_3C_4S_2) - C_1S_2S_3 + C_1C_2C_3 \\
& + \theta_6S_5(C_1C_2S_3S_4 - C_4S_1 + C_1C_3S_2S_4) \\
j_{g0,45} = & \ -C_4S_1 - \theta_6(C_5(S_1S_4 - C_4(C_1S_3 - C_2 - C_1C_3S_2)) - S_5(C_1C_3 \\
& - C_2 + C_1S_2S_3)) - S_4(C_1S_3 - C_2 - C_1C_3S_2) \\
j_{g0,46} = & \ C_{34}C_1C_5 - S_5(S_1S_4 + C_1C_2C_4S_3 + C_1C_3C_4S_2) \\
j_{g0,51} = & \ \theta_4C_1C_2C_3 - \theta_3S_1 - \theta_5C_4S_1 - \text{theta2}S_1 - \theta_4C_1S_2S_3 - \theta_6S_1S_4S_5 \\
& + \theta_6C_1C_2C_3C_5 + \theta_5C_1C_2S_3S_4 + \theta_5C_1C_3S_2S_4 - \theta_6C_1C_5S_2S_3 \\
& - \theta_6C_1C_2C_4S_3S_5 - \theta_6C_1C_3C_4S_2S_5 \\
j_{g0,52} = & \ C_1 - \theta_4C_2S_1S_3 - \theta_4C_3S_1S_2 + \theta_5C_2C_3S_1S_4 - \theta_6C_2C_5S_1S_3 \\
& - \theta_6C_3C_5S_1S_2 - \theta_5S_1S_2S_3S_4 - \theta_6C_2C_3C_4S_1S_5 + \theta_6C_4S_1S_2S_3S_5
\end{aligned}$$

$$\begin{aligned}
j_{g0,53} = & C_1 - \theta_4 C_2 S_1 S_3 - \theta_4 C_3 S_1 S_2 + \theta_5 C_2 C_3 S_1 S_4 - \theta_6 C_2 C_5 S_1 S_3 \\
& - \theta_6 C_3 C_5 S_1 S_2 - \theta_5 S_1 S_2 S_3 S_4 - \theta_6 C_2 C_3 C_4 S_1 S_5 + \theta_6 C_4 S_1 S_2 S_3 S_5 \\
j_{g0,54} = & \theta_5 (C_2 C_4 S_1 S_3 - C_1 S_4 + C_3 C_4 S_1 S_2) + \theta_6 S_5 (C_1 C_4 + C_2 S_1 S_3 S_4 \\
& + C_3 S_1 S_2 S_4) - S_1 S_2 S_3 + C_2 C_3 S_1 \\
j_{g0,55} = & C_1 C_4 + S_{34} S_1 S_4 - \theta_6 C_{34} S_1 S_5 + \theta_6 C_1 C_5 S_4 - \theta_6 C_2 C_4 C_5 S_1 S_3 \\
& - \theta_6 C_3 C_4 C_5 S_1 S_2 \\
j_{g0,56} = & C_{34} C_5 S_1 - S_5 (C_2 C_4 S_1 S_3 - C_1 S_4 + C_3 C_4 S_1 S_2) \\
j_{g0,61} = & 1 \\
j_{g0,62} = & \theta_6 S_{34} C_4 S_5 - \theta_6 C_{34} C_5 - \theta_5 S_{34} S_4 - \theta_4 C_{34} \\
j_{g0,63} = & \theta_6 S_{34} C_4 S_5 - \theta_6 C_{34} C_5 - \theta_5 S_{34} S_4 - \theta_4 C_{34} \\
j_{g0,64} = & \theta_5 C_2 C_3 C_4 - C_3 S_2 - C_2 S_3 - \theta_5 C_4 S_2 S_3 + \theta_6 C_2 C_3 S_4 S_5 - \theta_6 S_2 S_3 S_4 S_5 \\
j_{g0,65} = & \theta_6 (S_{34} S_5 - C_{34} C_4 C_5) + C_{34} S_4 \\
j_{g0,66} = & -S_{34} C_5 - C_{34} C_4 S_5
\end{aligned}$$

## **Jg6**

$$\begin{aligned}
j_{g6,11} = & 135 C_4 S_2 S_6 + 120 C_2 C_3 C_4 S_6 + 70 C_2 C_3 C_6 S_4 + 38 C_2 C_4 S_3 S_6 \\
& + 38 C_3 C_4 S_2 S_6 + 135 C_5 C_6 S_2 S_4 - 120 C_4 S_2 S_3 S_6 - 70 C_6 S_2 S_3 S_4 \\
& - 70 C_2 S_3 S_5 S_6 - 70 C_3 S_2 S_5 S_6 + 70 C_2 C_3 C_4 C_5 S_6 + 120 C_2 C_3 C_5 C_6 S_4 \\
& + 38 C_2 C_5 C_6 S_3 S_4 + 38 C_3 C_5 C_6 S_2 S_4 - 70 C_4 C_5 S_2 S_3 S_6 \\
& - 120 C_5 C_6 S_2 S_3 S_4 \\
j_{g6,12} = & 70 C_4 C_6 - 38 C_6 S_5 - 120 S_4 S_6 - 70 C_5 S_4 S_6 + 135 S_3 S_4 S_6 + 120 C_4 C_5 C_6
\end{aligned}$$

$$- 135C_3C_6S_5 - 135C_4C_5C_6S_3$$

$$j_{g6,13} = 70C_4C_6 - 38C_6S_5 - 120S_4S_6 - 70C_5S_4S_6 + 120C_4C_5C_6$$

$$j_{g6,14} = 70S_5S_6$$

$$j_{g6,15} = 70C_6$$

$$j_{g6,16} = 0$$

$$j_{g6,21} = 135C_4C_6S_2 + 120C_2C_3C_4C_6 + 38C_2C_4C_6S_3 + 38C_3C_4C_6S_2$$

$$- 70C_2C_3S_4S_6 - 120C_4C_6S_2S_3 - 70C_2C_6S_3S_5 - 70C_3C_6S_2S_5$$

$$- 135C_5S_2S_4S_6 + 70S_2S_3S_4S_6 + 70C_2C_3C_4C_5C_6 - 120C_2C_3C_5S_4S_6$$

$$- 70C_4C_5C_6S_2S_3 - 38C_2C_5S_3S_4S_6 - 38C_3C_5S_2S_4S_6$$

$$+ 120C_5S_2S_3S_4S_6$$

$$j_{g6,22} = 38S_5S_6 - 120C_6S_4 - 70C_4S_6 + 135C_6S_3S_4 + 135C_3S_5S_6$$

$$- 120C_4C_5S_6 - 70C_5C_6S_4 + 135C_4C_5S_3S_6$$

$$j_{g6,23} = 38S_5S_6 - 120C_6S_4 - 70C_4S_6 - 120C_4C_5S_6 - 70C_5C_6S_4$$

$$j_{g6,24} = 70C_6S_5$$

$$j_{g6,25} = -70S_6$$

$$j_{g6,26} = 0$$

$$j_{g6,31} = S_4S_5(135S_2 + 23961(0.5)\cos(\theta_2 + \theta_3 - \tan^{-1}(19/60)))$$

$$j_{g6,32} = 38C_5 + 135C_3C_5 + 120C_4S_5 - 135C_4S_3S_5$$

$$j_{g6,33} = 38C_5 + 120C_4S_5$$

$$j_{g6,34} = 0$$

$$j_{g6,35} = 0$$

$$j_{g6,36} = 0$$

$$\begin{aligned}
j_{g6,41} = & C_2C_3S_4S_6 + C_2C_6S_3S_5 + C_3C_6S_2S_5 - S_2S_3S_4S_6 + \theta_2C_2C_3C_6S_5 + \\
& \theta_3C_2C_3C_6S_5 + \theta_4C_2C_3C_4S_6 + \theta_5C_2C_5C_6S_3 + \theta_5C_3C_5C_6S_2 + \theta_6C_2C_3C_6S_4 - \\
& \theta_2C_2S_3S_4S_6 - \theta_2C_3S_2S_4S_6 - \theta_2C_6S_2S_3S_5 - \theta_3C_2S_3S_4S_6 - \theta_3C_3S_2S_4S_6 - \theta_3C_6S_2S_3S_5 - \\
& \theta_4C_4S_2S_3S_6 - \theta_6C_6S_2S_3S_4 - \theta_6C_2S_3S_5S_6 - \theta_6C_3S_2S_5S_6 - C_2C_3C_4C_5C_6 + C_4C_5C_6S_2S_3 + \\
& \theta_2C_2C_4C_5C_6S_3 + \theta_2C_3C_4C_5C_6S_2 + \theta_3C_2C_4C_5C_6S_3 + \theta_3C_3C_4C_5C_6S_2 + \theta_4C_2C_3C_5C_6S_4 + \\
& \theta_5C_2C_3C_4C_6S_5 + \theta_6C_2C_3C_4C_5S_6 - \theta_4C_5C_6S_2S_3S_4 - \theta_5C_4C_6S_2S_3S_5 - \theta_6C_4C_5S_2S_3S_6 \\
j_{g6,42} = & C_4S_6 + \theta_6C_4C_6 - \theta_4S_4S_6 + C_5C_6S_4 + \theta_4C_4C_5C_6 - \theta_5C_6S_4S_5 - \theta_6C_5S_4S_6 \\
j_{g6,43} = & C_4S_6 + \theta_6C_4C_6 - \theta_4S_4S_6 + C_5C_6S_4 + \theta_4C_4C_5C_6 - \theta_5C_6S_4S_5 - \theta_6C_5S_4S_6 \\
j_{g6,44} = & \theta_6S_5S_6 - \theta_5C_5C_6 - C_6S_5 \\
j_{g6,45} = & S_6 + \theta_6C_6 \\
j_{g6,46} = & 0 \\
j_{g6,51} = & C_2C_3C_6S_4 - C_6S_2S_3S_4 - C_2S_3S_5S_6 - C_3S_2S_5S_6 + \theta_4C_2C_3C_4C_6 - \\
& \theta_2C_2C_6S_3S_4 - \theta_2C_3C_6S_2S_4 - \theta_2C_2C_3S_5S_6 - \theta_3C_2C_6S_3S_4 - \theta_3C_3C_6S_2S_4 - \theta_3C_2C_3S_5S_6 - \\
& \theta_4C_4C_6S_2S_3 - \theta_5C_2C_5S_3S_6 - \theta_5C_3C_5S_2S_6 - \theta_6C_2C_3S_4S_6 - \theta_6C_2C_6S_3S_5 - \theta_6C_3C_6S_2S_5 + \\
& \theta_2S_2S_3S_5S_6 + \theta_3S_2S_3S_5S_6 + \theta_6S_2S_3S_4S_6 + C_2C_3C_4C_5S_6 - C_4C_5S_2S_3S_6 + \theta_6C_2C_3C_4C_5C_6 - \\
& \theta_2C_2C_4C_5S_3S_6 - \theta_2C_3C_4C_5S_2S_6 - \theta_3C_2C_4C_5S_3S_6 - \theta_3C_3C_4C_5S_2S_6 - \theta_4C_2C_3C_5S_4S_6 - \\
& \theta_5C_2C_3C_4S_5S_6 - \theta_6C_4C_5C_6S_2S_3 + \theta_4C_5S_2S_3S_4S_6 + \theta_5C_4S_2S_3S_5S_6 \\
j_{g6,52} = & C_4C_6 - C_5S_4S_6 - \theta_4C_6S_4 - \theta_6C_4S_6 - \theta_4C_4C_5S_6 - \theta_6C_5C_6S_4 + \theta_5S_4S_5S_6 \\
j_{g6,53} = & C_4C_6 - C_5S_4S_6 - \theta_4C_6S_4 - \theta_6C_4S_6 - \theta_4C_4C_5S_6 - \theta_6C_5C_6S_4 + \theta_5S_4S_5S_6 \\
j_{g6,54} = & S_5S_6 + \theta_5C_5S_6 + \theta_6C_6S_5 \\
j_{g6,55} = & C_6 - \theta_6S_6 \\
j_{g6,56} = & 0
\end{aligned}$$

$$\begin{aligned}
j_{g6,61} = & \theta_2 C_5 S_2 S_3 - C_3 C_5 S_2 - \theta_2 C_2 C_3 C_5 - \theta_3 C_2 C_3 C_5 - C_2 C_5 S_3 + \theta_3 C_5 S_2 S_3 + \\
& \theta_5 C_2 S_3 S_5 + \theta_5 C_3 S_2 S_5 - C_2 C_3 C_4 S_5 + C_4 S_2 S_3 S_5 - \theta_5 C_2 C_3 C_4 C_5 + \theta_2 C_2 C_4 S_3 S_5 + \\
& \theta_2 C_3 C_4 S_2 S_5 + \theta_3 C_2 C_4 S_3 S_5 + \theta_3 C_3 C_4 S_2 S_5 + \theta_4 C_2 C_3 S_4 S_5 + \theta_5 C_4 C_5 S_2 S_3 - \theta_4 S_2 S_3 S_4 S_5
\end{aligned}$$

$$j_{g6,62} = S_4 S_5 + \theta_4 C_4 S_5 + \theta_5 C_5 S_4$$

$$j_{g6,63} = S_4 S_5 + \theta_4 C_4 S_5 + \theta_5 C_5 S_4$$

$$j_{g6,64} = C_5 - \theta_5 S_5$$

$$j_{g6,65} = 0$$

$$j_{g6,66} = 1$$

# Reference

- [1] “Number of licensed medical and paramedical personnel, statistics of general health and welfare 2018, ministry of health and welfare,” 2019, <https://www.mohw.gov.tw/dl-18078-fd3fad52-83c8-4690-a8f1-64c468ab123a.html>. 1
- [2] “Number of licensed endodontists personnel, the acadamy of endodontology,” 2019, <http://www.aeroc.org.tw/member/download/1080107-%E5%B0%88%E7%A7%91%E9%86%AB%E5%B8%AB%E5%90%8D%E5%96%AE.pdf>. 1
- [3] J. L. Gutmann and P. E. Lovdahl, “Chapter 8 - problem solving in tooth isolation, access openings, and identification of orifice locations,” in *Problem Solving in Endodontics (Fifth Edition)*, J. L. Gutmann and P. E. Lovdahl, Eds. Saint Louis: Mosby, 2011, pp. 150–176. 3
- [4] ——, “Chapter 10 - problem-solving clinical techniques in enlarging and shaping the root canal,” in *Problem Solving in Endodontics (Fifth Edition)*, J. L. Gutmann and P. E. Lovdahl, Eds. Saint Louis: Mosby, 2011, pp. 195–208. 3
- [5] ——, “Chapter 12 - problem-solving challenges in root canal obturation,” in *Problem Solving in Endodontics (Fifth Edition)*, J. L. Gutmann and P. E. Lovdahl, Eds. Saint Louis: Mosby, 2011, pp. 218–240. 3

- [6] “Root canal procedure, tower endodontics,” 2020, <https://www.towerendodontics.com/find-out-more-about-our-services/introduction/>. 3
- [7] J. L. Gutmann and P. E. Lovdahl, “Chapter 11 - problem solving in cleaning and disinfecting the root canal system,” in *Problem Solving in Endodontics (Fifth Edition)*, J. L. Gutmann and P. E. Lovdahl, Eds. Saint Louis: Mosby, 2011, pp. 209–217. 4
- [8] G. Kim, H. Seo, S. Im, D. Kang, and S. Jeong, “A study on simulator of human-robot cooperative manipulator for dental implant surgery,” *2009 IEEE International Symposium on Industrial Electronics*, pp. 2159–2164, 2009. 4, 12
- [9] J. Li, Z. Shen, W. Xu, W. Y. Lam, R. T. C. Hsung, E. H. Pow, K. Kosuge, and Z. Wang, “A compact dental robotic system using soft bracing technique,” *IEEE Robotics and Automation Letters*, vol. 4, pp. 1271–1278, 2019. 4, 10, 11
- [10] J. Dong, S. Hong, and G. Hesselgren, “Wip: a study on the development of endodontic micro robot,” in *Proceedings of the 2006 IJME-INTERTECH Conference*. Citeseer, 2006. 4, 15, 16, 17
- [11] J. L. Gutmann and P. E. Lovdahl, “Chapter 5 - problem solving in the diagnosis of treatment failure,” in *Problem Solving in Endodontics (Fifth Edition)*, J. L. Gutmann and P. E. Lovdahl, Eds. Saint Louis: Mosby, 2011, pp. 97–118. 5

- [12] B. Sattapan, G. J. Nervo, J. E. Palamara, and H. H. Messer, “Defects in rotary nickel-titanium files after clinical use,” *Journal of Endodontics*, vol. 26, no. 3, pp. 161–165, 2000. 5, 69
- [13] M. Rawtiya, K. Verma, P. Sethi, and K. Loomba, “Application of robotics in dentistry,” *Indian J Dent Adv*, vol. 6, no. 4, pp. 1700–1706, 2014. 10
- [14] P. Ahmad, M. K. Alam, A. Aldajani, A. Alahmari, A. Alanazi, M. Stoddart, and M. G. Sghaireen, “Dental robotics: A disruptive technology,” *Sensors*, vol. 21, no. 10, 2021. 10
- [15] B. D. Bhat, S. Bhandary, R. Naik, D. Shetty *et al.*, “Robotics in dentistry: Fiction or reality,” *Journal of Dental Research and Review*, vol. 4, no. 3, p. 67, 2017. 10
- [16] Z. Haidar, “Autonomous robotics: A fresh era of implant dentistry... is a reality!” *Journal of Oral Research*, vol. 6, no. 9, pp. 230–231, 2017. 10
- [17] Y. Wu, F. Wang, S. Fan, and J. K.-F. Chow, “Robotics in dental implantology,” *Oral and Maxillofacial Surgery Clinics*, vol. 31, no. 3, pp. 513–518, 2019. 10
- [18] T. Iijima, T. Matsunaga, T. Shimono, K. Ohnishi, S. Usuda, and H. Kawana, “Development of a multi dof haptic robot for dentistry and oral surgery,” in *2020 IEEE/SICE International Symposium on System Integration (SII)*, 2020, pp. 52–57. 11

- [19] S. L. Bolding and U. N. Reebye, “Accuracy of haptic robotic guidance of dental implant surgery for completely edentulous arches,” *The Journal of prosthetic dentistry*, 2021. 12
- [20] ——, “Accuracy of haptic robotic guidance of dental implant surgery for completely edentulous arches,” *The Journal of Prosthetic Dentistry*, 2021. 12
- [21] “Implant surgery with robotic guidance – digital workflows for patient care,” 2019, <https://www.oralhealthgroup.com/features/implant-surgery-with-robotic-guidance-digital-workflows-for-patient-care/>. 13, 14
- [22] H. Everett, “Feasibility study of single-axis microrobot for endodontic treatment,” Ph.D. dissertation, University of Cincinnati. College of Engineering and Applied Science, 2014. 15
- [23] J. Dong and S. Y. Hong, “Design of z axis actuator and quick tool change assembly for an endodontic micro robot,” in *ASME International Mechanical Engineering Congress and Exposition*, vol. 44472, 2010, pp. 507–511. 15, 17
- [24] S. Neha, P. Shantipriya, K. Shekhar, R. Smitha, C. Ravichandra, and G. Sindhuра, “Micro robot - a revolution in endodontics,” *Annals of International medical and Dental Research*, vol. 3, 2017. 15
- [25] B. Benyo, L. Szilagyi, T. Haidegger, L. Kovacs, and C. Nagy-Dobo, “Detection of the root canal’s centerline from dental micro-ct records,” in *2009*

- Annual International Conference of the IEEE Engineering in Medicine and Biology Society*, 2009, pp. 3517–3520. 18
- [26] S. Yeotikar, A. M. Parimi, and Y. V. Daseswar Rao, “Automation of end effector guidance of robotic arm for dental implantation using computer vision,” in *2016 IEEE Distributed Computing, VLSI, Electrical Circuits and Robotics (DISCOVER)*, 2016, pp. 84–89. 18
- [27] M.-K. Wu, D. Barkis, A. Roris, and P. Wesselink, “Does the first file to bind correspond to the diameter of the canal in the apical region?” *International Endodontic Journal*, vol. 35, no. 3, pp. 264–267, 2002. 19
- [28] J. Agrawal, P. K. Shenai, L. Chatra, P. Y. Kumar *et al.*, “Evaluation of normal range of mouth opening using three finger index: South india perspective study,” *Indian Journal of Dental Research*, vol. 26, no. 4, p. 361, 2015. 19
- [29] C. Yang, J. Wang, L. Mi, X. Liu, Y. Xia, Y. Li, S. Ma, and Q. Teng, “A four-point measurement model for evaluating the pose of industrial robot and its influence factor analysis,” *Industrial Robot: An International Journal*, 2017. 33
- [30] T. Tang, H. Lin, Yu Zhao, Wenjie Chen, and M. Tomizuka, “Autonomous alignment of peg and hole by force/torque measurement for robotic assembly,” in *2016 IEEE International Conference on Automation Science and Engineering (CASE)*, 2016, pp. 162–167. 41

- [31] L. Bodenhagen, A. Fugl, M. Willatzen, H. Petersen, and N. Krüger, “Learning peg-in-hole actions with flexible objects,” *ICAART 2012 - Proceedings of the 4th International Conference on Agents and Artificial Intelligence*, vol. 1, 01 2012. [41](#)
- [32] Y. Xu, Y. Hu, and L. Hu, “Precision peg-in-hole assembly strategy using force-guided robot,” in *Proceedings of the 2015 3rd International Conference on Machinery, Materials and Information Technology Applications*. Atlantis Press, 2015/11, pp. 1406–1412. [41](#)
- [33] K. Van Wyk, M. Culleton, J. Falco, and K. Kelly, “Comparative peg-in-hole testing of a force-based manipulation controlled robotic hand,” *IEEE Transactions on Robotics*, vol. 34, no. 2, pp. 542–549, 2018. [41](#)
- [34] P. Zou, Q. Zhu, J. Wu, and J. Jin, “An approach for peg-in-hole assembling based on force feedback control,” in *2019 Chinese Automation Congress (CAC)*, 2019, pp. 3269–3273. [42](#)
- [35] A. Q. Keemink, H. van der Kooij, and A. H. Stienen, “Admittance control for physical human–robot interaction,” *The International Journal of Robotics Research*, vol. 37, no. 11, pp. 1421–1444, 2018. [52](#)
- [36] C. Erdogan, M. Zafar, and M. Stilman, “Gravity and drift in force/torque measurements,” Tech. Rep., 2014. [58](#)

- [37] C. Boessler, F. Paque, and O. A. Peters, “The effect of electropolishing on torque and force during simulated root canal preparation with protaper shaping files,” *Journal of Endodontics*, vol. 35, no. 1, pp. 102–106, 2009. [72](#), [75](#)